Copyright

by

Kurt David Fredrickson

2015

The Dissertation Committee for Kurt David Fredrickson Certifies that this is the approved version of the following dissertation:

First-Principles Studies of Perovskite Thin Films and Heterostructures

Committee:

Alexander A. Demkov, Supervisor

James R. Chelikowsky

John G. Ekerdt

Gregory A. Fiete

Allan H. MacDonald

First-Principles Studies of Perovskite Thin Films and Heterostructures

by

Kurt David Fredrickson, B.S.

Dissertation

Presented to the Faculty of the Graduate School of

The University of Texas at Austin

in Partial Fulfillment

of the Requirements

for the Degree of

Doctor of Philosophy

The University of Texas at Austin

August 2015

Dedication

To Maty

Acknowledgements

First and foremost, I would like to thank my advisor, Alex Demkov, for the support and help he's given me in my PhD. He has been an excellent mentor, and has reinforced my work ethic and my problem solving abilities. A good adviser should turn students into colleagues, and he treats me as such, always accepting input into our work, and always there for advice and direction on my projects. Due to vigorous fundraising, he was able to fund my research on a variety of grants, which gave me more time to spend on research and more time to follow the research down the various rabbit holes that presented themselves. I also am extremely grateful for the opportunity to attend the various conferences over the years, and especially my trip to France and Switzerland to attend the European Materials Science Research Spring Meeting, and to present my research with collaborators at ETH Zürich, IBM Zürich, and the Paul Scherrer Institute.

I would like to thank my groupmates, singling out Xuhui Luo, Jaekwan Lee, Alex Slepko and Hosung Seo for all their help in answering my questions about using VASP and physics in general, especially at the beginning, when I was getting my feet wet and the world of physics research was scary and intimidating. I would like to thank Patrick Ponath, Richard Hatch, Kristy Kormondy and Agham Posadas for answering all my experimental questions, and always serving as a reminder that when experiment and theory disagree, experiment wins. I would also like to thank Chungwei Lin for the countless discussions we had, and always probing me when I thought I understood something, until we were both sure we actually understood it.

I would like to thank my parents for all the support they've given me over the years, including raising me, teaching me the importance of hard work and perseverance, and

always showing interest in my work, even when they might not have understood all the finer points. I’d like to thank my girlfriend Maty, who has been beside me for the majority of the PhD, and given me the support and encouragement to keep going. She has been there for the good times and bad, and I don’t think this dissertation would exist without her.

First-Principles Studies of Perovskite Thin Films and Heterostructures

Kurt David Fredrickson, PhD

The University of Texas at Austin, 2015

Supervisor: Alex Demkov

The growth of oxides on semiconductors is of great interest for electronics applications; however, the effects of film growth, atomic adsorption, and strain can have fundamental effects on the properties of the oxides in question. In this dissertation, we use density functional theory to calculate the properties of $SrTiO_3$ and $BaTiO_3$, and discover the effects of the environment on the electronic and atomic properties of these systems. We examine the effects of H adsorption on the $SrTiO_3$ and $BaTiO_3$(001) surfaces, and discover the coverage-dependent onset and retreat of metallic surface states. We calculate the effect of Pt film growth on $BaTiO_3$, and study the effects on the polarization of $BaTiO_3$ for different Pt/$BaTiO_3$ interfaces. We study how strain and interfacial chemistry affect the ferroelectricity of $BaTiO_3$/Ge and $BaTiO_3$/$SrTiO_3$/Ge heterostructures. We also discuss the development of two-dimensional conducting states created in $BaTiO_3$/$SrTiO_3$ heterostructures.

Table of Contents

List of Tables x

List of Figures xi

Chapter 1: Introduction 1

Chapter 2: Computational Methods 6

2.1 The Born-Oppenheimer Approximation...6

2.2 Hohenberg-Kohn Theorems and Kohn-Sham Ansatz 8

2.3 The Local Density and Generalized-Gradient Approximations 10

2.4 Pseudopotentials and Pseudo Wave Functions....................................11

2.5 Landau-Ginzburg-Devonshire Theory of Ferroelectricity.....................14

2.6 The Modern Theory of Polarization 15

Chapter 3: Effect of H adsorption on the electronic and ionic reconstruction of $SrTiO_3$ and $BaTiO_3(001)$ surfaces..19

3.1 Introduction...19

3.2. The $SrTiO_3(001)$ Surface 22

3.2 The $BaTiO_3(001)$ Surface 45

Chapter 4: Thin Pt Films on $BaTiO_3$ 59

4.1 Introduction...59

4.2 Computational Details 60

4.3 Theoretical Results...63

4.4 Experimental Results 73

4.5 Conclusion 81

Chapter 5: Atomic and electronic structure of ferroelectric $BaTiO_3$/Ge(001) and $BaTiO_3$/$SrTiO_3$/Ge(001) heterostructures..82

5.1 Introduction...83

5.2 BTO/Ge Heterostructure...86

5.3. BTO/STO/Ge Heterostructure 105

Chapter 6: Switchable conductivity at the $BaTiO_3/SrTiO_3$ interface..................115
6.1 Introduction..115
6.2 Computational Details 118
6.3 Polarization Stability..120
6.3 Two-Dimensional Electron and Hole Gases..124
6.5 Conclusion 131
References..133

List of Tables

Table 3.1. The ionic motion (Å) of hydrogenated surfaces with respect to the clean TiO_2 surface. A positive number means the ion is moving towards vacuum, and a negative number means the ion is moving towards the bulk. 40

Table 4.1. Surface energies of Pt (J/m^2). 65

Table 5.1. Structural data for the Ge-O bonded interface. TiO_2 Layer 1 is closest to the interface, Layer 4 is farthest away. A positive value means that Ti is closer to the Ge dimer than O, and a negative value means that Ti is farther away from the dimer than O. 94

Table 5.2 Structural data for the Ge-O bonded Sr interface. TiO_2 Layer 1 is closest to the interface, Layer 4 is farthest away. A positive value means that Ti is closer to the Ge dimer than O, and a negative value means that Ti is farther away from the dimer than O. 94

Table 5.3. Structural data for the rock salt interface. TiO_2 Layer 1 is closest to the interface, Layer 4 is farthest away. A positive value means that Ti is closer to the Ge dimer than O, and a negative value means that Ti is farther away from the dimer than O. 94

Table 5.4. Structural data for SrO_2 interface. TiO_2 Layer 1 is closest to the interface, Layer 2 is farthest away. A positive value means that Ti is closer to the Ge dimer than O, and a negative value means that Ti is farther away from the dimer than O. Note that there are only 2 layers of inequivalent TiO_2 due to this being a supercell calculation and having two interfaces. 94

List of Figures

Figure 1.1. a) The cubic perovskite phase. b) The tetragonal, ferroelectric phase. Note the relative shift between the B site and O atoms, which is characteristic of the ferroelectric distortion in perovskites. c) The orthorhombic phase, with characteristic alternating rotations of the TiO_6 octahedra. 2

Figure 1.2. The density of states for a) STO and b) BTO, calculated with density functional theory in the local density approximation (LDA). The band gap is underestimated compared to experiment, which is typical for LDA calculations. 3

Figure 2.1. The solid-state system described by Equation 2.1. The red balls are the ions and the blue balls are electrons. 7

Figure 2.2. The solid-state system described by Equation 2.9. The red balls are the ions and the blue balls are electrons. Notice the neglect of the ion-ion potential and the ionic motion..8

Figure 2.3. The simulation cell, split into a core sphere and valence sphere.........12

Figure 2.4. The unit cell of BTO. The rumpling of Ti and O in the c-direction creates a dipole moment **P**. 14

Figure 2.5. A hypothetical unit cell with alternating positive and negative charges; it is infinitely periodic in all directions. The box is a choice of unit cell, and the arrow is the corresponding polarization of that cell. Note that the polarization of the cell changes direction depending on the choice of the unit cell, which is unphysical. 16

Figure 3.1. a) The bulk and surface Brillouin zones for $SrTiO_3$ with labeled symmetry directions and points. b) Paths in the bulk Brillouin zone corresponding to ARPES measurements for two different photon energies, *hν*. RHEED images for the c) vacuum annealed sample and d) a sample etched in buffered HF, respectively, with the images taken just off the [110] azimuth due to geometric constraints of the sample holder.............25

Figure 3.2. a) The surface projected band structure of bulk STO along the [110] direction for a fine grid of k_z values that spans the bulk Brillouin zone as calculated using DFT. b) For ease of comparison to ARPES data, each line in (a) is broadened using a Lorentzian function with a FWHM of 0.3 eV. c) Same as b), but calculated using a tight-binding (TB) model.27

Figure 3.3. ARPES data along the [110] direction for STO samples prepared in a variety of ways for a photon energy of $h\nu = 21.22$ eV unless otherwise stated. a) Raw data for vacuum-annealed STO, with the 2nd derivative (in the Energy direction) shown in b) in order to better visualize dispersing bands. c), d) After water-leaching the STO surface quality is greatly improved and the ARPES data reveals dispersing bands after a simple background removal. Photoemission spectra (with background removal) for STO samples etched in e), f) BHF and those g), h) etched using the Arkansas method. i) The 2nd derivative of ARPES data for MBE-grown, undoped STO. 30

Figure 3.4. Normal emission XPS spectra of the Sr 3*d* core level for a STO(001) sample having undergone a) a vacuum-anneal b) as well as a sample etched in BHF. The primary STO lattice peaks (more intense) are accompanied by lower intensity peaks (green) which are attributed to the presence of strontium oxide crystallites on the surface which are removed, to some extent, after etching with BHF. 31

Figure 3.5. a) Angle-integrated photoemission data of the primarily O 2*p*-derived valence band states for a variety of STO preparations with b) a close-up of the gap region. Data for the BHF-etched STO is omitted from a) and b) since it is very nearly indistinguishable from the Arkansas-prepared STO. The photoemission data reveals at least two gap-states: an oxygen-vacancy state at a binding energy of $E-E_F \approx -1$ eV and another gap state about 800 meV above the top of the valence band located at $E-E_F \approx -2.75$ eV. 33

Figure 3.6. ARPES data for emission angles, θ, along the [110] direction for an STO sample prepared using the Arkansas method that correspond to the O 2*p*-derived valence band and the gap region. The pronounced shoulder for larger emission angles (at an energy of $E-E_F \approx -3.75$ eV) corresponds to the top of the valence band at the *R* point of the Brillouin zone. A close-up of the shaded region is shown in the inset and shows a mid-gap state about 800 meV above the top of the valence band that hardly disperses. 34

Figure 3.7. Sections of $SrTiO_3$ slabs corresponding to several of the systems studied using DFT calculations of the surface electronic structure. All slabs are (1×1). a) A TiO_2-terminated slab with one O replaced by F. b) Same as a) with the addition of a H bonded to Ti. c) A TiO_2-terminated slab with a single hydroxyl group. d) Same as c) with a H bonded to Ti. e) A fully hydrogenated slab with two hydroxyl groups, and a H bonded to Ti.36

Figure 3.8. a)-g) DFT calculations of the surface electronic structure for bare SrO-and TiO_2-terminated slabs as well as slabs shown in Figures 3.7 a)-e) respectively. DFT calculations predict a pronounced, dispersing surface state about 980 meV above the valence band states that roughly follows the dispersion of the STO bulk bands which is not present in the case of an SrO-terminated slab. Because of the dispersing nature of the surface state in b), it is unlikely the origin of the mid-gap state discussed in Figure 3.6, despite the TiO_2-termination that results from the Arkansas preparation. As seen in d) and f), a likely explanation for this mid-gap state is the termination of the Ti dangling bond with H. As discussed in the text, for this termination to occur, it must be preceded by either a substitution of a surface O with F, or the formation of a hydroxyl group. 37

Figure 3.9. Normal emission XPS survey spectrum for a STO(001) sample prepared by BHF etching. The F 1*s* core level has a binding energy of ~685 eV, and, if present, should be located in the region highlighted with a red circle. Despite etching with BHF, the concentration of F on the surface is negligible (we estimate ≤ 1% of all anions within the probe depth). Other sample preparations yield equally low concentrations of F (see inset)...38

Figure 3.10. a) The charge density of the non-dispersing band for the F-substituted slab with H on Ti. There is no charge density on the F (not shown). b) The charge density of the nondispersing band for the H on O, H on Ti slab. 40

Figure 3.11. Comparison of theoretical calculations for various STO systems with ARPES data for the BHF-prepared sample. a) The calculation for bulk STO band structure (see also Figure 3.2 a)-b), where prominent features are highlighted with white open circles. For ease of comparison, these same open circles are overlaid on the data in b)-j) which corresponds to data in Figure 3.2 c), Figures 3.8 a), b), d)-g) and Figures 3.3 e), f) respectively. It is apparent that the different STO terminations hardly affect band structure predicted by DFT bulk calculations, but can give rise to surface states both above and below the valence band as seen in d)-h)...43

Figure 3.12. The band structure of the clean TiO_2-terminated surface. The Fermi energy is indicated with a dotted line. a) The contribution of the surface Ti atom is shown in blue. b) The contribution of the surface O atoms are shown in red...46

Figure 3.13. a) The TiO_2-terminated surface, with 3 H adsorbed. b) The order of adsorption. 1) H adsorbs on one of the O sites. 2) H adsorbs on the Ti site. 3) H adsorbs on the remaining O site. 47

Figure 3.14. The band structure for the H adsorbed (1×1) surface. a) The surface Ti contribution in blue. b) The O of the OH complex contribution in red. c) The adsorbed H contribution in green. 48

Figure 3.15. The band structure for the 2H adsorbed (1×1) surface. a) The surface Ti contribution in blue. b) The O of the OH group contribution in red. c) The adsorbed H contribution in green. 49

Figure 3.16. The band structure for the 3H adsorbed (1×1) surface. a) The surface Ti contribution in blue. b) The surface O contribution in red. c) The H contribution in green. 50

Figure 3.17. The charge density difference plots for the a) 1H, b) 2H and c) 3H cases. The red indicates an increase in charge density, and the blue indicates a decrease in charge density. 51

Figure 3.18. The order of adsorption for the (√2×√2) surface. 1) The H adsorbs on an O site. 2) The H adsorbs on another O site, farthest from the original OH complex. 3) The H adsorbs on one of the Ti sites. 4) The H adsorbs on one of the other free O sites. 52

Figure 3.19. The band structure for the 3H adsorbed (√2×√2) surface. a) The surface Ti contribution in blue. b) The surface O contribution in red. c) The H contribution in green. 53

Figure 3.20. The band structure for the 3H adsorbed (√2×√2) surface. a) The surface Ti contribution in blue. b) The surface O contribution in red. c) The H contribution in green. 54

Figure 3.21. The rumpling of the TiO_2 layers for a) the clean BTO(001) surface, b) the 1H adsorbed surface, c) the 2H adsorbed surface and d) the 3H adsorbed surface. The green dotted line is the rumpling of bulk BTO. In b) and c), the red represents the rumpling between the O with adsorbed H and Ti, and the blue represents the rumpling between the O without adsorbed H and Ti. In d), although both O have adsorbed H, their rumpling is inequivalent near the surface. 56

Figure 3.22. The rumpling of the ($\sqrt{2}\times\sqrt{2}$) TiO_2 layers for a) the 1H adsorbed surface, b) the 2H adsorbed surface, c) the 3H adsorbed surface and d) the 4H adsorbed surface. The green dotted line is the rumpling of bulk BTO. The red line indicates rumpling between a pair of Ti and O where both have adsorbed H, the green line indicates rumpling between a pair of Ti and H where one of the atoms has an adsorbed H, and blue indicates rumpling between a pair of Ti and H with no adsorbed H................58

Figure 4.1. a) The simulation cell containing the BTO/(100)Pt slab. The slab shown contains ten UCs of BTO. b) Zoomed-in portion that shows polarization of BTO. 62

Figure 4.2. The rumpling for each TiO_2 plane for the BTO/Pt structures with a) 5.5 UC b) 10.5 UC c) 15.5 UC and d) 20.5 UC of BTO. The green line is rumpling for bulk BTO. 64

Figure 4.3. Polarized slabs of a) TiO_2 terminated and b) BaO terminated BTO. ..67

Figure 4.4. Surface energy of BaO and TiO_2-terminated BTO slabs. 68

Figure 4.5. Surface energies of out-of-plane polarized BaO- and TiO_2-terminated BTO slabs. Below the red line, the surface energy of the TiO_2-terminated slab is the lowest, but as this this never occurs within the restrictions, the surface energy of the BaO-terminated slab is always the lowest. 69

Figure 4.6. Surface energy of Pt and energy of the Pt/BTO interface as a function of the chemical potential for the a) (100) and b) (110) interface. The shaded area in a) indicates the variation of the interface energy with the thickness of the BTO slab. 70

Figure 4.7. a) The TEM image of the Pt/BTO interface. The zig-zag chains of Pt are identified in red. b) The model used to calculate properties of this interface, with the zig-zag Pt identified in red. The model is rotated 90º with respect to the TEM image. 71

Figure 4.8. The BTO/(110)Pt interface, showing the three directions of rumpling.72

Figure 4.9. Rumpling of the (110)Pt/BTO/(110)Pt structure in the a) a, b) b and c) c directions. 73

Figure 4.10. Low-magnification cross-section TEM image of the Pt/BTO/STO/Si structure. 75

Figure 4.11. Higher magnification TEM image. 75

Figure 4.12. a) A cubic island. b) A diamond island. c) An irregular island. 76

4.13. Elemental maps showing Sr, Si, Ti, Ba, Pt, and O distributions, extracted from area under ionization edge after fitting power law background. Top left image represents the high-angle annular dark-field image acquired during the acquisition of the spectrum-image and the top right image represent a color overlay of the Si (blue), Sr (green), Pt (red), and Ba (magenta) elements. Pixel separation 2.6 Å, map size 195 by 143 pixels. Probe size less than 2Å. 77

Figure 4.14. Atomic resolution elemental overlay of the Pt (blue), Ba (red), and Ti (green) showing the interface layers. Pixel separation 0.4 Å, map size 64 by 60 pixels. 78

Figure 4.15. Lines of Pt, Ba, and Ti are extracted by summing the signal from a 0.4 nm wide box parallel to the interface along a trajectory perpendicular to the Pt/BTO interface. 79

Figure 5.1 The GOB cubic unit cell...88

Figure 5.2. a) The Ge-O interface. b) The Ge-O Sr interface. c) The rock salt interface. d) The SrO_2 interface. 90

Figure 5.3. a) The GOB-BaO interface. b) The GOB-TiO_2 interface...................91

Figure 5.4. Band offset diagrams for the a) Ge-O bonded b) Ge-O Bonded Sr c) Rock Salt d) SrO2 e) GOB-BaO interface. Filled interfacial states are dark blue, and empty interfacial states are light blue...............................92

Figure 5.5. The possible directions of rumpling for the BTO film/Ge substrate system. 93

Figure 5.6. a) X-ray diffraction 2θ-θ scan of a 40 nm BTO film grown on Ge(001). Only substrate peaks and (*h*00) peaks of BTO are present indicating *a*-axis out-of-plane orientation. The inset shows a reflection high-energy electron diffraction pattern for a 12-nm-thick BTO on Ge, viewed along the <110> azimuth of BTO. b) High resolution 2θ-θ scan about the BTO(200) peak (dots) overlaid with a pseudo-Voigt function fit (solid line). The peak position indicates an out-of-plane lattice constant of 3.99 Å. c) Rocking curve scan of the same BTO/Ge sample about the BTO(200) peak, with a full width at half maximum of 0.7°. d) Reciprocal space map around the (103)/(301) reciprocal lattice point. The centroid of the feature corresponds to a = 3.99 Å and c = 4.01 Å. The small black circles indicate the positions corresponding to in-plane spacings of 4.03 and 3.99 Å. The in-plane structure is expected to have a mosaic domain structure but is unresolved in this scan. 97

Figure 5.7. a) High-angle annular-dark-field aberration-corrected electron micrograph showing abrupt nature of BTO/Ge interface. b) Enlarged view of BTO/Ge interface showing a region of the BTO-Ge interface with both 2x and 1x periodicities visible along the plane of the interface. c) Same image with overlaid structural model. Arrow indicates step edge in Ge corresponding to transition between 2x and 1x periodicity of the reconstructed Ge surface viewed in [110]-type projection. 100

Figure 5.8. Ge *3d* core level spectrum for a sample with 4-nm-thick BTO overlayer. There is a chemical shift of 2.1 eV that is consistent with metal-O-Ge bonding. 101

Figure 5.9. a) Calculated structure of the BTO/Ge interface after a step. Note that half of the O at the interface has relaxed to be on top of the Ge dimers. b) The BTO interface showing influences of two steps. Before the first step, the interface is the same as Figure 5.4. After the first step, the interface is that of Figure 5.5 a), rotated 90°. After the second step, the interface is the same as before either of the steps. In order to maintain the same interface, we propose a rock salt bonding between the BTO on either side of the steps. 104

Figure 5.10. The supercell used in the DFT calculations, consisting of vacuum, BTO, STO and B-doped Ge. The cell is mirrored on the other side (not shown). Note the recession of the Ti from the surface, indicating polarization away from the BTO surface, and toward the BTO/STO interface. Below, we show the macroscopic average of the plane-averaged electrostatic potential for the P_1 and P_2 states. 107

Figure 5.11. a) X-ray diffraction θ-2θ scan of 16 nm $BaTiO_3$ epitaxially grown on Ge(001) substrate, with and without a 2 nm $SrTiO_3$ buffer layer. Without the buffer, the d-spacing corresponds to the *a*-axis of BTO directed out of plane. With the STO buffer, the *c*-axis of BTO is directed out of plane. b) Reciprocal space map of the (103) Bragg reflection for BTO/STO/Ge. The centroid of the peak is consistent with a short in-plane axis and long out-of-plane axis. The inset shows a typical RHEED pattern for BTO/STO/Ge taken along the [110] azimuth showing good crystallinity and surface flatness. 108

Figure 5.12. a) High-angle annular-dark-field (ADF) image of BTO/STO/Ge(001) heterostructure recorded with 200-keV probe-corrected scanning transmission electron microscope. White spots correspond to positions of metal atoms. b) Fourier transform of ADF image confirming tetragonality of BTO layer. c) Enlargement of ADF image showing region of BTO film. d) Corresponding line profile from c) showing shifts in Ti atomic-column positions..109

Figure 5.13. a) Topography, b) BE-PFM amplitude and c) associated phase image after a box-in-box switching experiment on the BTO heterostructure, showing clear ferroelectric switching. A 5 x 5 μm^2 box was poled with the tip held at -6 V, and then a smaller box 2.5 x 2.5 μm^2 was subsequently scanned with the tip held at +4 V before the BE-PFM images were captured. 100 hysteresis loops were then captured on the same film using BE spectroscopy. The average response is shown in the spectrograms in d) for amplitude (above) and phase (below), with the applied DC waveform shown in blue. Selected e) amplitude and f) phase loops are shown, with the average loop shown as a solid line in olive.111

Figure 5.14. a) Schematic diagram illustrating the measurement setup and configuration of samples. A negative-biased conductive scanning probe makes downward to upward switching in ferroelectric polarization of BTO layer, which modulates hole density at the BTO/p-Ge interface. b) PFM, AFM (bottom right corner in b), c) MIM real part and MIM imaginary part (bottom right corner in c) images acquired after writing a 20 × 20 mm^2 square by applying -4 V DC bias on the tip (Scale bars: 10 mm). d) Simulated MIM-Re (blue line) and MIM-Im (red line) signals as a function of conductivity at the BTO/Ge interface. Left and right insets, respectively, show band diagrams of Ge in regions A and B in panel c). 113
Figure 6.1. The simulation cell, showing the Vacuum/BTO/STO/BTO/Vacuum slab. 120
Figure 6.2. The a) rumpling and b) polarization for the paraelectric P_0 structure, and the c) rumpling and d) polarization for the polarized P_+ structure..122
Figure 6.3. The comparison of plane-averaged electron electrostatic potential between P_0 and P_+. The difference in potential due to the polarization in the P_+ case can be clearly seen. 124
Figure 6.4. The layer-decomposed DOS for a) P0 and b) P+. The slab is mirrored on the other side, so only a half of the DOS is shown. 125
Figure 6.5. The DOS of the system projected on TiO_2 planes in the energy vs distance plane for the a) polarized and b) paraelectric BTO/STO heterostructure. In the polarized case, the 2DEG and the 2DHG can be clearly seen.126

Figure 6.6. Projected DOS for selected TiO2 planes for the polarized BTO/STO heterostructure. a) p-states and b) d-states of the BTO surface, c) p-states and d) d-states of the BTO/STO interface, and e) p-states and f) d-states of the center of the STO bulk. The 2DEG can be seen to be of almost all d-character, and the 2DHG can be seen to be almost entirely p-character. 127

Figure 6.7. The charge density at the Fermi level. The pictured isosurface is for a charge density of 0.1203 e/Å^3. a) The hole gas at the surface of BTO. Note the p-character of the charge density. b) The electron gas at the STO/BTO interface. Note the d-character of the charge distribution.128

Figure 6.8. a) The electric field caused by the polarization of BTO. b) The electric field caused by the 2DEG and 2DHG. Note that the gases cause a field that opposes the field caused by the polarization of the sample. 130

Chapter 1: Introduction

An important subclass of oxides are the perovskites, with the ABO_3 formula.[1] These materials are remarkably versatile, due to the ability to accommodate almost every atom in the periodic table in the A or B position;[2] various perovskites are high-*k* dielectrics ($SrTiO_3$),[3] ferroelectrics ($BaTiO_3$),[4] muliferroics ($BiFeO_3$),[5] exhibit colossal magnetoresistance ($La_{1-x}Ca_xMnO_3$),[6] and have a metal-insulator transition ($LaAlO_3$).[7] Perovskites consist of an A-site “cage” with a B-O_6 octahedron inside (Figure 1.1 a)); in the simple cubic case, the perovskite has space group $Pm\bar{3}m$.[8] The octahedra often undergo energetically favorable distortions.[9] Some of them are driven by B-site bonding, which allows them to stabilize a ferroelectric distortion; the O and B-site anion are no longer in the same plane (Figure 1.1 b)), and the cell becomes tetragonal, with space group P4mm.[8,10] However, the majority of them do this by rotating the octahedra (Figure 1.1 c)); this optimizes the A-site cation coordination, and causes the cell to become orthorhombic, with space group Amm2.[8,11,12]

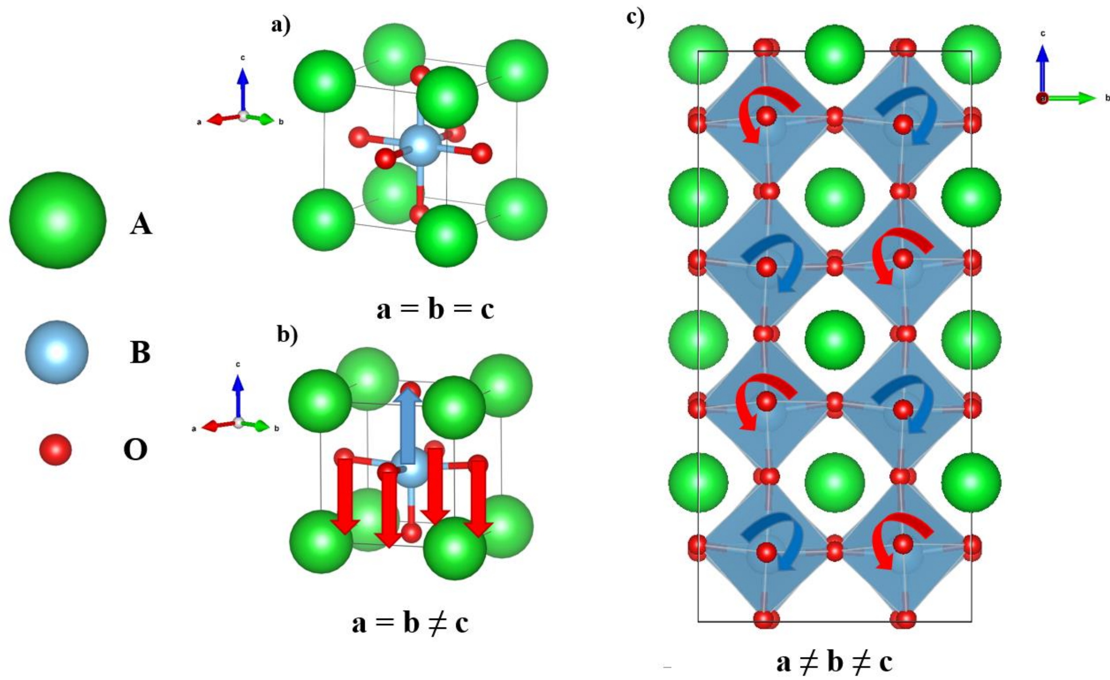

Figure 1.1. a) The cubic perovskite phase. b) The tetragonal, ferroelectric phase. Note the relative shift between the B site and O atoms, which is characteristic of the ferroelectric distortion in perovskites. c) The orthorhombic phase, with characteristic alternating rotations of the TiO_6 octahedra.

In this dissertation, we will be primarily concerned with two transition metal perovskites, $SrTiO_3$ (STO) and $BaTiO_3$ (BTO). At room temperature, STO is cubic, and BTO is tetragonal and ferroelectric. Both of their electronic structure is very similar, with the valence and conduction bands formed by hybridization of the O p states and the Ti d states; the valence band is primarily of p character and the conduction band is primarily of d states. The band gap is indirect (3.2 eV for BTO[13] and 3.25 eV for STO[14]) and is constituted by the energy gap between O p and Ti d hybrid states (Figure 1.2). Due to crystal symmetry, the Ti d states are split into triply degenerate t_{2g} and doubly degenerate e_g states; the bottom of the conduction band is composed of t_{2g}, with the e_g states located ~ 2 eV higher in energy. The Ba and Sr states are far from the Fermi level and their

contribution is mainly to donate charge to the system; formally, they donate 2 electrons per cell, but theory shows that they tend to donate closer to 1.

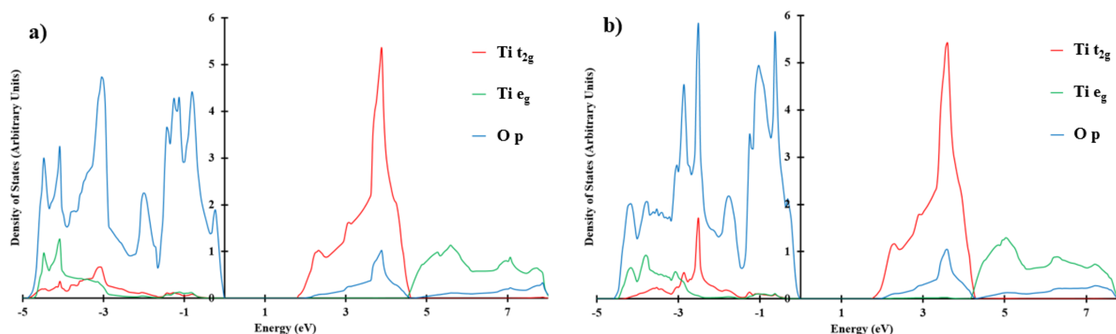

Figure 1.2. The density of states for a) STO and b) BTO, calculated with density functional theory in the local density approximation (LDA). The band gap is underestimated compared to experiment, which is typical for LDA calculations.

Although the bulk properties of STO and BTO are interesting in and of themselves, there is great excitement in the integration of oxides on semiconductors. Due to ferroelectricity in BTO, there is work on the integration of BTO with polarization parallel to the semiconductor/BTO interface for microwave applications[15] and non-linear optic devices;[16] the growth of BTO with the polarization normal to the interface is an important criteria for the development of a ferroelectric field-effect transistor.[17,18] The interface is critical for integration of BTO with semiconductors,[19] having been studied extensively both theoretically[20–25] and experimentally.[25–29]

Our main concern will be: how does the interaction of BTO or STO with semiconductors, insulators, metals or atoms, change their material properties (for example, ferroelectric behavior and electronic structure) or the electronic structure of the entire superstructure (for example, band offsets and charge transfer)? Previous studies have shown that strain can increase the polarization of BTO by 250% compared to bulk.[30,31] Very thin films of STO have been found to be ferroelectric,[32–34] and under strain even thick

films of STO can be made ferroelectric,[35] in contrast to bulk STO, which is paraelectric and does not become ferroelectric under any temperature. In general, metal/BTO interfaces reduce the polarization of BTO, due to incomplete screening by the metallic contacts;[36,37] however, this depends on the specific metal-oxide bond, and for BTO/Pt the polarization in BTO can actually be enhanced.[38] BTO/Co and BTO/Fe heterostructures have been shown to have a multiferroic interface; the induced magnetization at the interface can be controlled by the polarization of BTO.[39,40] BTO/STO heterostructures also show enhanced polarization in BTO and induced polarization in STO,[41] along with enhanced dielectric response.[42] $CaTiO_3$/STO/BTO heterostructures have been shown to have greatly enhanced polarization[43,44] and dielectric constants,[45] despite the fact that neither $CaTiO_3$ nor STO is expected to be ferroelectric. Interfaces between transition metal oxides can lead to novel emergent interface states,[46] such as the creation of two-dimensional gases,[46–52] which has some promise for new devices; field-effect transistors incorporating 2DEGs are expected to have very high mobilities even at room temperature.[53]

The adsorption of atoms and molecules on BTO and STO surfaces is another important topic. Perovskites have been shown to be effective catalysts for removing CO and CH_4;[54] BTO is an effective catalyst for the combustion of CH_4 in particular.[55] Prior research shows that the adsorption of H_2O on the TiO_2-terminated (001)BTO surface leads to disassociation into H^+ and OH^- groups, and ~20% of Ti surface atoms have these OH^- groups; the OH^- adsorbed on Ti is enough to reverse the polarization of the surface TiO_2 layer;[56] adsorption of H_2O on the BaO-terminated surface leads to surface O vacancies, $Ba(OH)_2$ groups, and reversal of the surface polarization.[57] Likewise, the coverage of H on the TiO_2-terminated (001)STO surface changes the electronic structure dramatically; depending on the amount of coverage, the surface changes from insulating to metallic and back again.[58,59]

In Chapter 2, we discuss the theoretical methods that will form the backbone of the remainder of the dissertation. In Chapter 3, we discuss the adsorption of H on the STO and BTO(001) surfaces, and its effect on their electronic structure. In Chapter 4, we discuss the wetting of BTO by Pt, including its formation of islands and on the ferroelectricity of the BTO substrate. In Chapter 5, we discuss the models of the BTO/Ge interface and their effects on the band offsets of the system; we also discuss the BTO/STO/Ge heterostructure, and its effects on the polarization of BTO. Finally, in Chapter 6 we discuss the polarization stability of the BTO/STO heterostructure and the effect of the polarization on the creation of two-dimensional gases.

Chapter 2: Computational Methods

2.1 The Born-Oppenheimer Approximation

The Hamiltonian H for a solid-state system is known, in principle, exactly:

$$H = T_e + T_I + V_{e-e} + V_{I-e} + V_{I-I} \tag{2.1}$$

T_e is the kinetic energy of the electrons:

$$T_e = \sum_i \frac{p_i^2}{2m} \tag{2.2}$$

where p_i is the momentum of electron i, and m is the mass of the electron. T_I is the kinetic energy of the ions:

$$T_I = \sum_j \frac{P_j^2}{2M_j} \tag{2.3}$$

where P_j is the momentum of ion j, and M_j is the mass of ion j. V_{e-e} is the electron-electron interaction term:

$$V_{e-e} = \frac{1}{2}\sum_{i,j} V(r_i, r_j) \tag{2.4}$$

where r_i is the position of electron i, and r_j is the position of electron j. V_{I-e} is the electron-ion interaction term:

$$V_{I-e} = \frac{1}{2}\sum_{I,j} V(R_I, r_j) \tag{2.5}$$

where R_I is the position of ion I, and r_j is the position of electron j. Finally, V_{I-I} is the ion-ion interaction term:

$$V_{I-I} = \frac{1}{2}\sum_{I,J} V(R_I, R_J) \tag{2.6}$$

where R_I and R_J are the positions of ion I and ion J, respectively. In all cases, V is the Coulomb interaction that is attractive for the ion-electron interaction and repulsive for the electron-electron and ion-ion interaction. We want to solve the Schrödinger equation:

$$H\Psi_0(\{r_i\},\{R_J\}) = E_0\Psi_0(\{r_i\},\{R_J\}) \tag{2.7}$$

where Ψ_0 is the ground state many-body wave function, that is a function of the set of electron positions $\{r_i\}$ and ion positions $\{R_J\}$, and E_0 is the ground state energy.

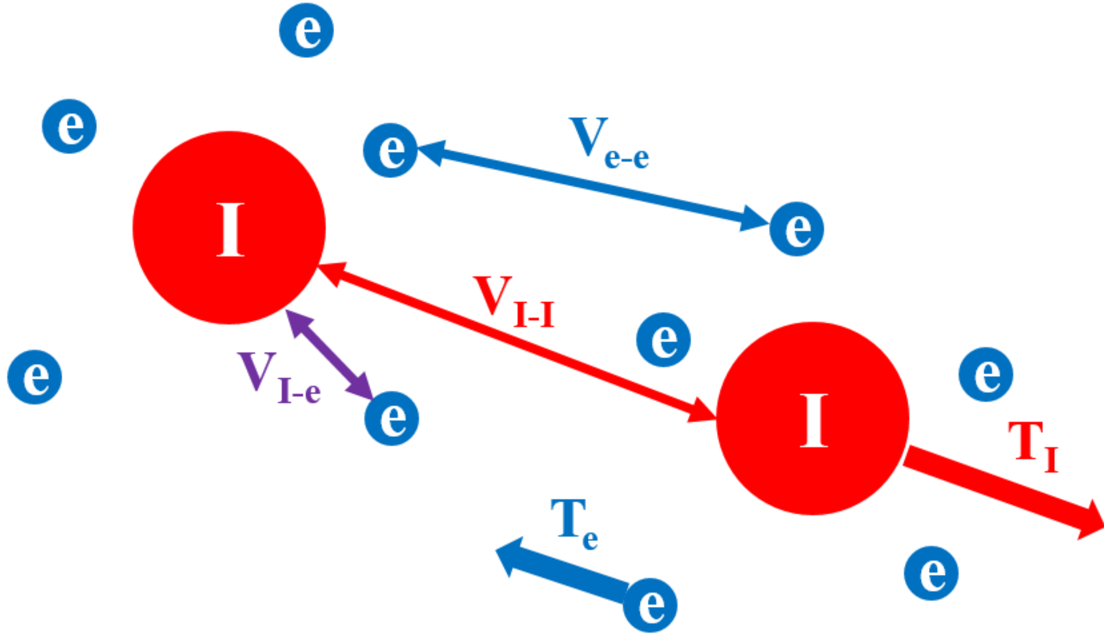

Figure 2.1. The solid-state system described by Equation 2.1. The red balls are the ions and the blue balls are electrons.

Although we have the exact Hamiltonian for any solid-state system we wish to study, in practice the equation is far too complicated to solve even on powerful computers, and approximations must be made. The first such approximation typically is the *Born-Oppenheimer approximation*, in which we treat the ionic and electron wave functions as separable:

$$\Psi_0(\{r_i\},\{R_J\}) = \psi(\{r_i\},\{R_J\})\phi(\{R_J\}) \tag{2.8}$$

where ψ is electronic wave function and φ is the ionic wave function. The typical justification for this is that the ions are much more massive than the electrons, and thus we expect their velocities to be much lower. We treat the electrons as adiabatically responding to the change in the positions of the ions, and therefore their wave functions can be solved

separately. If we are interested in the electronic wave functions, the Born-Oppenheimer approximation allows us to treat the ions as a static background potential, and thus we ignore their kinetic energies. The ion-ion interaction also is greatly simplified, as it is now a constant energy that for many purposes can be neglected.

Our electronic Hamiltonian under the Born-Oppenheimer approximation is now:

$$H_{BO} = T_e + V_{e-e} + V_{I-e} + E_{I-I} \tag{2.9}$$

where E_{I-I} is a constant.

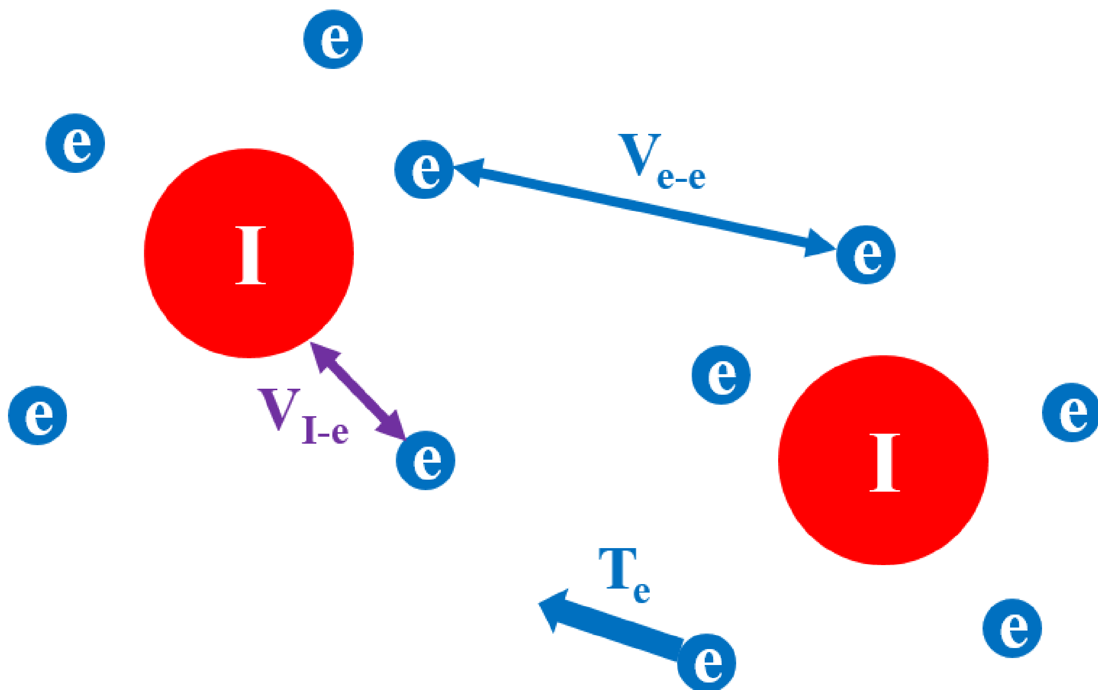

Figure 2.2. The solid-state system described by Equation 2.9. The red balls are the ions and the blue balls are electrons. Notice the neglect of the ion-ion potential and the ionic motion.

2.2 Hohenberg-Kohn Theorems and Kohn-Sham Ansatz

Next, we take advantage of two extremely powerful theorems formulated by Hohenberg and Kohn:[60]

I: For an electron gas with density $n_0(r)$, the background potential $V_{ext}(r)$ is determined uniquely by the ground state density $n_0(r)$, up to an arbitrary added constant. This means that all ground-state properties are determined uniquely by the ground state density.

II: There is an universal energy functional $E[n(r)]$ for any background potential $V_{ext}(r)$; the global minimum of this functional corresponds to the ground state density. This means that we only need to determine this functional once, and it will be valid for all systems.

The Hohenberg-Kohn theorems are useful because, generally, the density is less complicated than the full many-body wave function. However, they can also be augmented with the Kohn-Sham Ansatz:[61]

For a given many-body system, there is an auxiliary system consisting of noninteracting electrons, that can completely describe the original system with an additional background potential that must be determined self-consistently; the electron density of the auxiliary system is the same as that of the real many-body problem.

This ansatz is extremely powerful; it allows us to replace the many-body wave function Ψ with a set of single-particle wave functions φ:

$$\Psi(r_1, r_2, \ldots r_N) \Rightarrow \sum_{i=1}^{N} \varphi(r_i) \tag{2.10}$$

and ground-state density given by

$$\sum_{i=1}^{N} \left|\varphi_i(r_i)\right|^2 = n_0(r) \tag{2.11}$$

The Kohn-Sham equations are given by:

$$(-\frac{1}{2}\nabla_i^2 + V_{ext}(r_i) + V_{Hartree}(r_i) + V_{XC}(r_i))\varphi_i(r_i) = E_i\varphi_i(r_i) \tag{2.12}$$

where $V_{ext}(r)$ is the Coulomb potential due to the ions, $V_{Hartree}(r)$ is the classical Coulomb potential due to the electron gas interacting with itself, and

$$V_{XC}(r_i) = \frac{\delta E_{XC}}{\delta n(r_i)} \tag{2.13}$$

is the exchange-correlation potential. Thus, all the information that separates the single-particle system from the true many-body system is the exchange-correlation potential. The problem is that we do not know $E_{XC}[n(r)]$; if we did, we could solve the original many-body problem exactly (in the Born-Oppenheimer approximation).

2.3 The Local Density and Generalized-Gradient Approximations

A common approximation for the exchange-correlation energy functional is the *local density approximation (LDA)*, given by:

$$E_{XC}^{LDA}[n(\mathbf{r})] = \int n(\mathbf{r}) \varepsilon_{XC}(n(\mathbf{r})) d^3\mathbf{r} \tag{2.14}$$

where $\varepsilon_{XC}(r)$ is the exchange-correlation energy density. The exchange-correlation energy is assumed to be the same as the homogeneous electron gas with that same density. This automatically makes the approximation local (the solution depends only on the density of the gas at position $\boldsymbol{r}$). Despite the simplicity of this model, the results are often quite good among a variety of materials.

The *generalized-gradient approximation (GGA)* also includes the gradient of the electron density:

$$E_{XC}^{GGA}[n(\mathbf{r})] = \int n(\mathbf{r}) \varepsilon_{XC}(n(\mathbf{r}), |\nabla n(\mathbf{r})|) d^3\mathbf{r} \tag{2.15}$$

This approximation is nonlocal, due to the inclusion of the gradient term (the nearby electron densities in proximity of $\boldsymbol{r}$ also are important).

2.4 Pseudopotentials and Pseudo Wave Functions

Real atomic potentials and wave functions in practical calculations are undesirable to work with for several reasons. The electrostatic potential of an atom diverges negatively upon approaching the center of the atom, which can cause numerical difficulties in the calculation of wave functions. The core electrons are assumed to be chemically inert (they do not participate in bonding), so that much of the computational time spend on calculating the core electron wave functions are wasted. Also, the valence electron wave functions must be orthogonal to all other wave functions in the system; this means that they oscillate rapidly near the core, in order to be orthogonal to the tightly-bound core electron wave functions. This rapid oscillation causes additional computational cost with very little gain, as there is little interest of the value of the valence wave function near the core.

The solution to these problems is two-fold: first, we assume that the core electrons do not participate in bonding, and so we do not let them change as a function of their chemical environment; this is commonly called the frozen core approximation. Secondly, we do not use the true atomic potential or the valence electron wave functions; these are replaced with pseudopotentials and pseudo wave functions.[62–64] We can divide our atomic system into two distinct areas; the core sphere, and the valence sphere (Figure 2.3), where the core sphere corresponds to the volume contained by the sphere less than the critical radius r_C, and the valence sphere corresponds to the volume in a sphere greater than r_C; the upper maximum for the radius size of the valence sphere depends on the atom and pseudopotential in question. In the valence sphere, the pseudo wave functions match the atomic wave functions and the pseudopotential potential matches the atomic potential exactly; in the core sphere, the pseudo wave functions and pseudopotentials do not match the real wave functions and atomic potential, and are allowed to vary in a way that makes them computationally more tractable. The smaller the value of r_C, the more accurate the

calculation, but the higher the computational cost. The energy of the pseudo state and the real state is also required to be the same. An important issue is that dividing the electrons into core or valence electrons is somewhat arbitrary, and testing should be applied to see that the division produces physically sensible results.

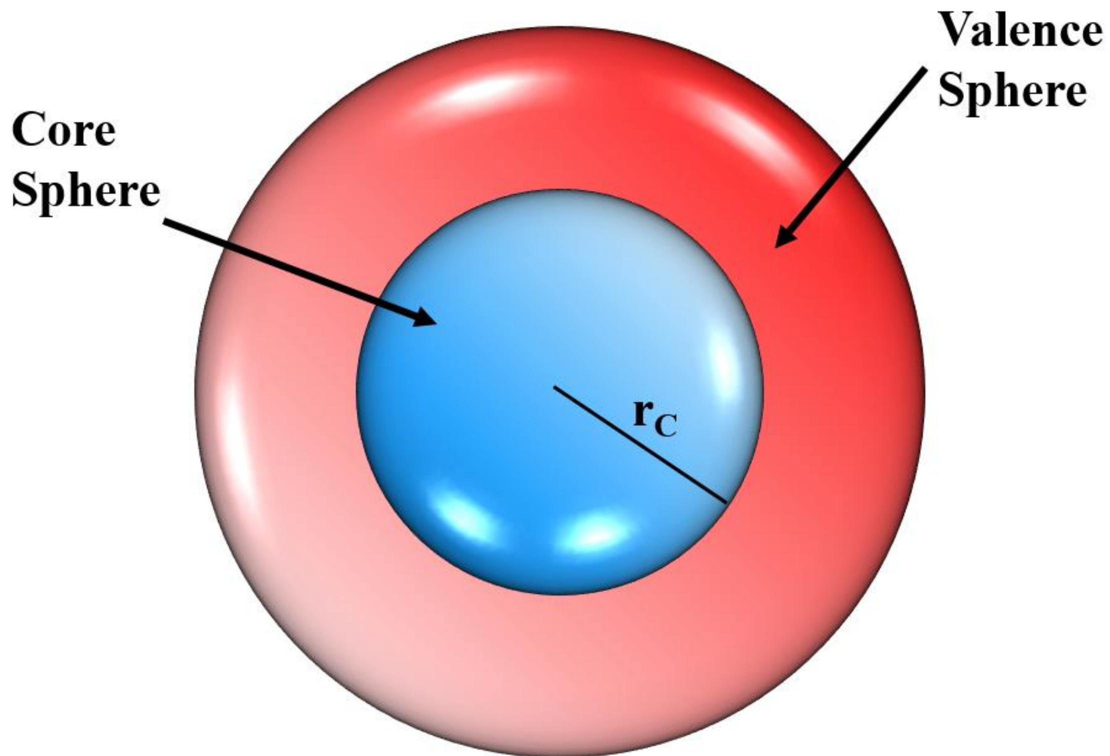

Figure 2.3. The simulation cell, split into a core sphere and valence sphere.

One commonly used pseudopotential method is the projector augmented wave (PAW) method;[65–67] all the results in this work will use the PAW method. The real all-electron wave functions ψ are related to the smoothed ψ' pseudo wave functions by

$$\psi = T\psi' \tag{2.16}$$

with $T = 1 + T_0$ inside the core sphere, and $T = 1$ inside the valence sphere; this satisfies the condition that the pseudo wave function must match the real wave function in the valence sphere, while in the core sphere they are allowed to vary. For a chosen basis $|\psi_m\rangle$,

$$\begin{aligned} |\psi\rangle &= T|\psi'\rangle = \sum_m c_m|\psi_m\rangle \\ &= |\psi'\rangle + \sum_m c_m(|\psi_m\rangle - |\psi'_m\rangle) \end{aligned} \tag{2.17}$$

For a set of projection operators p_m in each sphere,

$$c_m = \langle p_m|\psi'\rangle \tag{2.18}$$

where the set of p_m satisfies the biorthogonality condition

$$\langle p_m|\psi_{m'}'\rangle = \delta_{mm'} \tag{2.19}$$

Finally, we can describe the operator T in terms of the projectors,

$$T = 1 + \sum_m (|\psi_m\rangle - |\psi'_m\rangle)\langle p_m| \tag{2.20}$$

We can see that this easily satisfies the condition that ψ is equal to ψ' in the valence sphere.

For any arbitrary operator A in the all-electron problem, A can be transformed into an operator A' in the modified pseudo wave function problem by the following relation:

$$\begin{aligned} A' &= T^{T*}AT \\ &= A + \sum_{mm'} |p_m\rangle(\langle\psi_m|A|\psi_{m'}\rangle - \langle\psi'_m|A|\psi'_{m'}\rangle)\langle p_{m'}| \end{aligned} \tag{2.21}$$

Crucially, we can add a term

$$B - \sum_{mm'} |p_m\rangle\langle\psi'_m|B|\psi'_{m'}\rangle\langle p_{m'}| \tag{2.22}$$

for any arbitrary operator B and we will not change the expectation values. The key behind the entire technique is that we can include an operator that represents the Coulomb energy at the core (where it diverges) and remove it from the problem without changing the physics.[68] Thus, the original issue of dealing with the problematic atomic potential at the origin is removed.

2.5 Landau-Ginzburg-Devonshire Theory of Ferroelectricity

$BaTiO_3$ (BTO) is a insulating perovskite that is ferroelectric at room temperature. Below the transition temperature of 393 K, BTO becomes tetragonal, with the c lattice constant elongating. This strain causes the Ti-O bonds lengths to be longer in the c-direction than in the others, and to compensate, the Ti and O shift such that they are no longer in the same plane; this causes the bond lengths in the a-b plane to slightly elongate, but the Ti-O bonds in the c-direction to shrink and become closer to the original length. The formal charges in BTO are Ba^{2+}, Ti^{4+}, and O^{2-}, and because the Ti and O atoms are not in-plane, but are rumpled, this creates a permanent dipole moment that is the origin of ferroelectricity. The rumpling is defined as the relative shift of Ti and O (Figure 2.4).

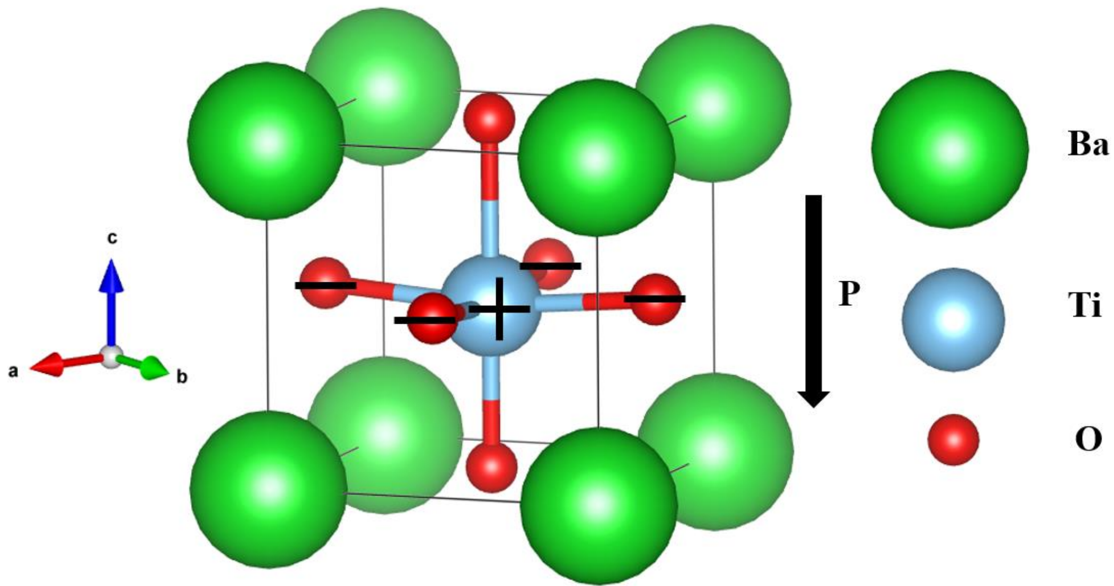

Figure 2.4. The unit cell of BTO. The rumpling of Ti and O in the c-direction creates a dipole moment **P**.

An instructive phenomenological model for ferroelectricity is the Landau-Ginzberg-Devonshire model,[69–75] which has been expanded for ferroelectrics.[76,77] For a second-order phase transition, the Gibbs free energy density G is given by:

$$F = F_0 + \frac{1}{2}\alpha P^2 + \frac{1}{4}\beta P^4 + \frac{1}{6}\gamma P^6 - EP \tag{2.23}$$

where F is the free energy density, F_0 is the free energy density in the paraelectric (non-ferroelectric) phase, P is the polarization of the sample, and E is the applied electric field. To find the equilibrium configuration of the system, we solve for the P that minimizes F:

$$\frac{\partial F}{\partial P} = 0 \tag{2.24}$$

which gives us E as a function of P

$$E = \alpha P + \beta P^3 + \gamma P^5 \tag{2.25}$$

In ferroelectrics with first-order transitions (such as BTO), the coefficients are determined as:

$$\alpha = \frac{1}{C\varepsilon_0}(T - T_0),\ \beta < 0,\ \gamma > 0 \tag{2.26}$$

In this case the polarization under no applied field is given by

$$P_s = P(E=0) = \pm\sqrt{\frac{-\beta + \sqrt{\beta^2 - 4\alpha\gamma(T-T_0)}}{2\gamma}} \tag{2.27}$$

and the electric susceptibility χ is given by[78]

$$\chi = \left(\frac{\partial E}{\partial P}\right)^{-1} = \frac{1}{\alpha(T - T_C) + 3\beta P_s^2 + 5\gamma P_s^4} \tag{2.28}$$

The coefficients must be supplied to the model; they are typically derived from experiment or *ab initio* theory.

2.6 The Modern Theory of Polarization

Although the definition of polarization in a thin-film is uncontroversial, the definition of polarization in an infinite bulk (as is used in cells with periodic boundary conditions) is more subtle. Take, for example, the charge density shown in Figure 2.4. In an infinitely periodic system, the choice of unit cell determines the direction of the

polarization, which is unphysical; the choice of unit cell should not affect the fundamental properties of the system.

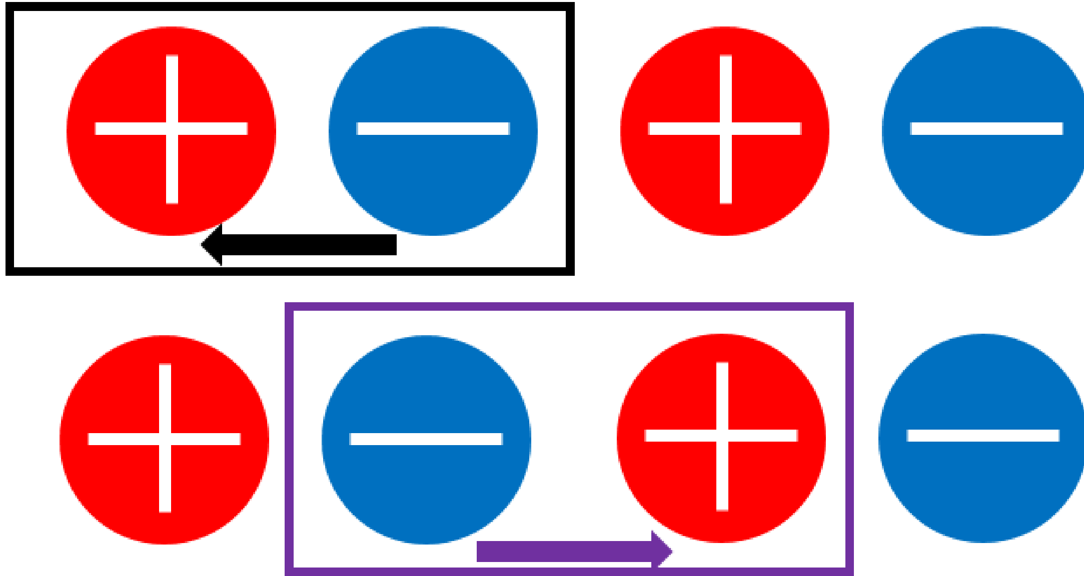

Figure 2.5. A hypothetical unit cell with alternating positive and negative charges; it is infinitely periodic in all directions. The box is a choice of unit cell, and the arrow is the corresponding polarization of that cell. Note that the polarization of the cell changes direction depending on the choice of the unit cell, which is unphysical.

The modern theory of polarization was developed to remedy this issue in calculations. The polarization of an infinite bulk ferroelectric can be seen as analogous to that of potential energy in classical mechanics; although the absolute potential energy can be shifted by an arbitrary constant, the *change* in energy is meaningful; while the absolute value of polarization is not a meaningful quality, the *change* in polarization is. We can define a change in polarization as

$$\Delta\mathbf{P} = \int_{\lambda_1}^{\lambda_2} \frac{\partial \mathbf{P}}{\partial \lambda} d\lambda \tag{2.29}$$

where λ parametrizes an adiabatic transition; in ferroelectrics, it is a displacement. So λ_1 corresponds to the paraelectric phase, and λ_2 corresponds to the ferroelectric phase. The derivative with respect to λ is given by[79]

$$\frac{\partial \mathbf{P}}{\partial \lambda} = \frac{ieh}{2\pi N\Omega m} \sum_{\mathbf{k}} \sum_{n}^{occ} \sum_{m}^{un} \frac{\langle \psi_{n\mathbf{k}}^{\lambda} | \mathbf{p} | \psi_{m\mathbf{k}}^{\lambda} \rangle \langle \psi_{m\mathbf{k}}^{\lambda} | \frac{\partial}{\partial \lambda} | \psi_{n\mathbf{k}}^{\lambda} \rangle}{(E_{n\mathbf{k}}^{\lambda} - E_{m\mathbf{k}}^{\lambda})^2} + c.c. \tag{2.30}$$

where N is the number of unit cells, Ω is the volume of the unit cell, m is the mass of the unit cell, ψ are the wave functions, $\boldsymbol{p}$ is the momentum, and the summations run over the occupied and unoccupied bands. It has also been shown that the change in λ is conservative, i.e. we only need to know the end points:

$$\Delta \mathbf{P} = \mathbf{P}^{\lambda_2} - \mathbf{P}^{\lambda_1} \tag{2.31}$$

Also, we only need the wave functions of the valence band, because the polarization is a ground state property.[80] $\boldsymbol{P}$ is given by

$$\mathbf{P}^{\lambda} = \frac{-ie}{8\pi^3} \sum_{m}^{occ} \int \langle u_{m\mathbf{k}}^{\lambda} | \nabla_{\mathbf{k}} | u_{m\mathbf{k}}^{\lambda} \rangle d^3\mathbf{k} \tag{2.32}$$

where u is the periodic part of the Bloch function. It turns out that the polarization is only defined up to $ne\boldsymbol{R}/\Omega$, where $\boldsymbol{R}$ is a lattice vector, and n is an integer. In practice, however, this term is larger than the calculated polarization, so there is no confusion.

An important property that can be computed is the Born effective charge tensor Z^*:

$$Z_{\upsilon,ij}^{*} = \Omega \frac{\partial P_i}{\partial q_{\nu,j}} \tag{2.33}$$

where q is the displacement of ion υ. There is a Born effective charge tensor for each atom in the unit cell, and it describes how the polarization changes with the motion of each atom. In crystals with high symmetry (such as BTO), the off-diagonal elements are zero. The Born effective charge tensor can be found from density functional perturbation theory (DFPT);[81,82] since the polarization is highly linear with respect to the rumpling,[83] we can calculate the polarization as

$$P_i = \frac{1}{\Omega}\sum_{\upsilon} Z^{*}_{\nu,ij} q_{\upsilon,j} \tag{2.34}$$

We can see that the difference in rumpling between the cubic paraelectric phase and the tetragonal ferroelectric phase is the main contribution to the polarization.

Since the density functional perturbation theory calculations are computationally intensive, we use the bulk Born effective charges with the actual displacements calculated for surfaces and interfaces, where DFPT is too expensive.

Chapter 3: Effect of H adsorption on the electronic and ionic reconstruction of $SrTiO_3$ and $BaTiO_3$(001) surfaces*

High-resolution angle-resolved photoemission spectroscopy was used to study the surface electronic structure of Nb-doped $SrTiO_3$ (STO) single crystals prepared using a variety of surface preparations. A non-dispersing, mid-gap state was found ~800 meV above the top of the valence band for samples which underwent etching. This mid-gap state is not present for vacuum-annealed and water-leached samples, as well as for STO thin films grown using molecular beam epitaxy. Theoretical modeling using density functional theory suggests that this mid-gap state is not related to the SrO- and TiO_2-terminated surfaces, but rather, is due to a partial hydrogenation of the STO surface that occurs during etching. We also calculated the electronic structure of H-adsorbed BTO surfaces, and found them to be either metallic or insulating depending on the H coverage, similar to that of STO. We also showed that the rumpling of BTO is increased for the metallic systems, due to the system reacting to the field caused by adsorbed bare H atoms.

3.1 INTRODUCTION

Complex oxide materials exhibit a wide range of phenomena such as magnetism, superconductivity, ionic conduction, ferroelectricity and multiferroic behavior, and have many promising applications.[37] Many of the more interesting oxides have perovskite structure, with $SrTiO_3$ (STO), a cubic perovskite, being one of the most heavily studied examples. By itself, STO possesses many notable properties such as water photolysis,[84]

---

*The work described in this chapter has been published as "Surface electronic structure for various surface preparations of Nb-doped $SrTiO_3$(001)", R.C. Hatch, K.D. Fredrickson, M. Choi, C. Lin, H. Seo, A.B. Posadas and A.A. Demkov, J. Appl. Phys. **114**, 103710 (2013). R.C.H. performed ARPES measurements and prepared the STO surface. K.D.F., C.L. and H.S. designed and performed the first-principles calculations. M.C. and A.B.P. grew the samples. A.A.D. contributed to the theoretical calculations and the overall design of the work.

photovoltaic effect,[85] blue-light emission[86] and superconductivity.[87] Furthermore, STO is favorably lattice-matched to many other complex oxides, and is a widely-used substrate for epitaxial oxide growth. The interfaces of STO with other oxides also display an array of interesting phenomena. Perhaps the most widely studied of these interfaces is that of $LaAlO_3$/STO, motivated by the discovery of a two-dimensional electron gas (2DEG) at the interface.[47,88–90] This 2DEG is quite remarkable with interesting magnetic effects,[91] superconductivity,[92] and ferromagnetism.[93,94] Several other STO heterostructures have notable properties as well such as magnetic ordering in $LaMnO_3$/STO[17] superlattices[95] and $LaCoO_3$/STO heterostructures,[96,97] electronic reconstruction,[98,99] and superconductivity at $LaTiO_3$/STO and $LaVO_3$/STO interfaces.[100–102] To understand these numerous properties, and maximize the functionality of STO-based devices, it is important to gain a greater understanding of the surface electronic structure of STO, and prepare STO substrates with high surface quality.

Since many of the unique properties of oxide heterostructures require atomically abrupt interfaces, the preparation of atomically flat, defect-free substrates is of utmost importance. The surfaces of STO(001) crystals, as provided by the manufacturer, do not typically have a unique surface termination as a result of mechanical polishing. One of the most common methods of preparing atomically-smooth, uniquely-terminated STO surfaces is based on a process used heavily in the semiconductor industry for removal of SiO_2 on Si, and consists of etching of the surface in a buffered solution of HF (BHF) followed by a high-temperature anneal in flowing O_2.[103–106] A similar process, often referred to as the "Arkansas" method, substitutes HCl/HNO_3 for HF, and reportedly minimizes surface defects resulting from the BHF etch.[107,108] Regardless of the method, the acid-based etching dissolves the SrO terraces more quickly than the TiO_2 terraces, leaving a rough surface comprised of TiO_2 islands. The subsequent anneal in O_2 results in large,

atomically flat TiO_2 terraces as a consequence of mass transport.[104,109,110] More recently, in an effort to avoid the safety issues of acidic etchants which have served as an obstacle to researchers embarking on studies of interfacial properties of oxides, it has been shown that various forms of water-leaching are able to preferentially dissolve the SrO terraces, which, after a subsequent anneal, result in atomically flat, TiO_2-terminated STO.[111–113] While the water-leaching methods result in flat, TiO_2-terminated STO, a thorough study comparing the effectiveness of acid-based etching and water-leaching is not yet available.

In order to study the electronic properties of STO, a number of researchers have utilized angle-resolved photoemission spectroscopy (ARPES). These studies have employed a number of different surface preparations including sputtering and annealing,[114] cleaving or scraping,[115–118] vacuum-anneal,[119] epitaxial thin film growth,[120] and chemical etching with vacuum anneal.[121–124] It is unlikely that sputtering and annealing provides the desired, atomically flat surfaces because of the different sputtering cross sections of the STO constituents which will likely result in non-ideal surface stoichiometry. While cleaving is a moderately effective method of surface preparation for ARPES experiments, it is expected to give rise to a large number of oxygen vacancies at the surface, and likely contributes to the formation of a 2DEG at the surface of STO.[115–118] Furthermore, cleaving in ultra-high vacuum (UHV) is not a convenient method of preparing substrates for heteroepitaxy and the creation of heterojunctions. Regardless of surface preparation, ARPES has been used to study a number of the electronic properties of STO. Using n-doped STO, such experiments have shed light on the nature of the bottom of the conduction band, or quantum-confined conduction band states and resulting 2DEGs[115–118,121–124] and have revealed the presence and origin of mid-gap states.[115–120,123,124] Finally, a number of ARPES measurements have investigated the valence band dispersions, with an older work sampling at a few *k*-points using the so-called normal emission method,[114] and, more

recently, works providing detailed measurements by utilizing a range of emission angles.[118,119,121]

The adsorption of atoms and molecules on BTO surfaces is another important topic. Perovskites have been shown to be effective catalysts for removing CO and CH_4;[54] BTO is an effective catalyst for the combustion of CH_4 in particular.[55] Prior research shows that the adsorption of H_2O on the TiO_2-terminated (001)BTO surface leads to disassociation into H^+ and OH^- groups, and ~20% of Ti surface atoms have these OH^- groups; the OH^- adsorbed on Ti is enough to reverse the polarization of the surface TiO_2 layer;[56] adsorption of H_2O on the BaO-terminated surface leads to surface O vacancies, $Ba(OH)_2$ groups, and reversal of the surface polarization.[57] However, there are currently no theoretical studies performed of pure H adsorption on the atomic and electronic structures of the BTO surface; this deserves serious consideration for its effect on the polarization of BTO; interstitial H has been shown to increase the polarization of bulk BTO.[125,126]

Because of the sensitivity of ARPES to defects in materials, this work utilizes ARPES as a tool to compare the effectiveness of a number of different preparations of STO(001). The ARPES measurements show that the surface electronic structure depends heavily on the surface preparation. Finally, a comparison of ARPES data to first-principles band structure calculations, for different STO terminations, sheds light on the origins of a number of electronic features in STO.

3.2. The $SrTiO_3$(001) Surface

3.2.1 Experimental Details

The surface electronic structure of (001)-oriented, Nb-doped STO ($SrNb_{0.01}Ti_{0.99}O_3$) single crystals (CrysTec GmbH Kristalltechnologie) was studied using

ARPES for a variety of surface preparations. The ARPES system consists of an electrostatic, hemispherical, electron-energy analyzer (Scienta R3000) with a monochromated He discharge source. He Iα radiation ($h\nu$ = 21.22 eV) was used in all experiments except for those where a photon energy of $h\nu$ = 40.81 eV (He IIα) is explicitly indicated. The combined energy resolution was ΔE < 20 meV for $h\nu$ = 21.22 eV and ΔE < 35 meV for $h\nu$ = 40.81 eV and the angular resolution was $\Delta\theta \sim 1°$. All measurements presented here were performed in the $\bar{\Gamma}\bar{M}$ direction (i.e. the [110] direction of the surface Brillouin zone) as shown in Figure 3.1 a), and the sample temperature was between 120 K and 150 K (well above the second-order phase transition from cubic to tetragonal structure which occurs at the critical temperature of $T_c \approx$ 105 K).[127,128] The approximate k-path probed in the bulk Brillouin zone, can be determined using the free electron final state model,[129,130] where the wave vector perpendicular to the sample is given by

$$k_z \approx \sqrt{\frac{2m_e}{\hbar^2}}\sqrt{V_0 + E_K \cos^2(\theta)} \tag{3.1}$$

where m_e is the electron mass, V_0 is the inner potential, E_K is the kinetic energy of the photoelectron, and θ is the emission angle. Assuming an inner potential of V_0 = 14.5 eV, which is consistent with literature values[114,115,121] and expectations based on the depth of the oxygen valence band, as well as an STO lattice constant of a = 3.905 Å, we calculate the k-paths probed for the two photon energies and plot them in Figure 3.1 b). These k-paths are broadened due to the range of kinetic energies measured, and because of the finite escape depth of the photoelectrons. As seen in Figure 3.1 b), the measurements, roughly speaking, map the band structure along the XR and ΓM directions for photon energies of $h\nu$ = 21.22 and 40.81 eV respectively.

Five different surface preparations were studied in this work. The first preparation, referred to as “vacuum anneal” consisted of ultrasonic degreasing of the sample in acetone and isopropanol (IPA) for 10 minutes each, followed by a 4 hour anneal in UHV at a

temperature of 750°C. The second preparation is based on the BHF etch.[103,104] The third preparation is based on the "Arkansas" method.[108] The fourth sample preparation is based on water leaching,[112] and consisted of the same ultrasonic degreasing as the vacuum annealed samples, followed by a 48 hour soak in deionized water (DI H_2O) at room temperature. The sample was then annealed in UHV at 775°C for 2 hours. The fifth and final preparation method was the growth of an undoped STO thin film (10 unit cells thick), using molecular beam epitaxy (MBE). For this final preparation method, all characterization of the thin STO films was done *in situ*.

All surface preparations were also studied using reflection high-energy electron diffraction (RHEED) and resulted in sharp diffraction patterns consistent with an atomically flat surface with no noticeable surface reconstructions. Representative RHEED images taken along the [110] azimuth of STO, at an electron energy of 18 keV and glancing angle of 3°, are shown in Figure 3.1 c) and d). Somewhat surprisingly, there were no obvious differences in the diffraction features for the different surface preparations, but a more rigorous RHEED study, with a comprehensive, quantitative analysis would probably reveal differences.[111]

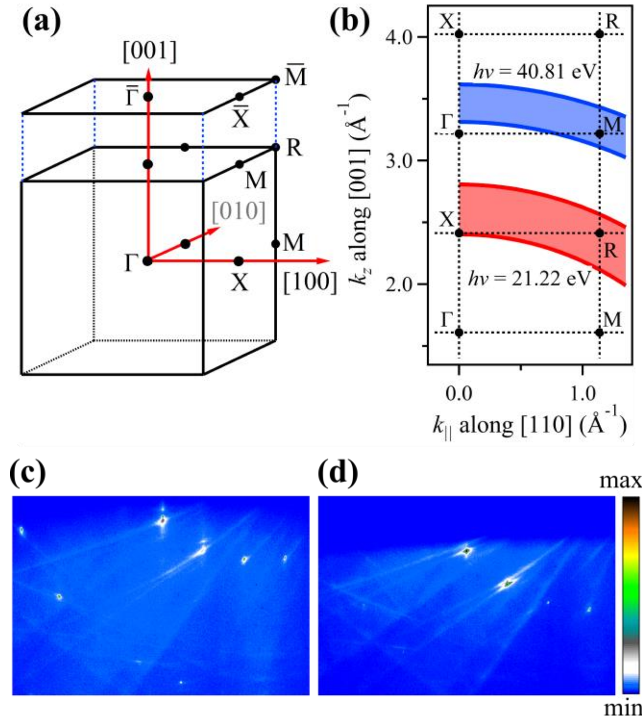

Figure 3.1. a) The bulk and surface Brillouin zones for $SrTiO_3$ with labeled symmetry directions and points. b) Paths in the bulk Brillouin zone corresponding to ARPES measurements for two different photon energies, *hv*. RHEED images for the c) vacuum annealed sample and d) a sample etched in buffered HF, respectively, with the images taken just off the [110] azimuth due to geometric constraints of the sample holder.

Density functional theory was used to model the bulk and surface of STO. All calculations were done using the local density approximation and projector augmented-wave pseudopotentials as included in the VASP code.[65,66,131–134] We used the Perdew-Zunger form of the exchange-correlation potential.[135] The valence configuration of $3p^6 4s^2 3d^2$ was used for Ti, $4s^2 4p^6 5s^2$ for Sr, $2s^2 2p^4$ for O, $1s^1$ for H and $2s^2 2p^5$ for F. A kinetic energy cutoff of E_{cutoff} = 650 eV was used. For the Brillouin zone integration, the following Monkhorst-Pack[136] *k*-point meshes were used: 6×6×6 for bulk STO, and 6×6×1 for the relaxation of surface structures, and 18×18×2 for the surface-band calculations. Bulk STO was optimized, and all structures were optimized with respect to the ionic positions until the forces on all atoms were less than 10 meV/Å; for the STO slabs,

optimization was performed until the forces were less than 50 meV/Å. The energy was converged to 10^{-3} meV per atom. The lattice constant of cubic STO was calculated to be 3.861 Å, in good agreement with an experimental value of 3.905 Å[137] and a previously reported theoretical value of 3.873 Å.[97] The small difference in lattice constant calculated in this work as opposed to that in Ref. 60 can be attributed to the 650 eV cutoff energy used here compared to 600 eV used previously. All slabs were symmetrically terminated (1×1), and were 8.5 unit cells thick, with a vacuum thickness of 15 Å.

3.1.2 Discussion

In order to better understand the differences between the surface and bulk electronic structure of STO, DFT calculations were performed for bulk STO. Figure 2.2 a) shows the results of these calculations, where the STO band structure in the [110] direction is projected onto the [001] surface. For convenience in comparison to ARPES measurements, the data in Figure 3.2 a) are broadened using a Lorentzian function with a full-width at half-maximum (FWHM) of 0.3 eV with the results shown in Figure 3.2 b). While this process neglects all photoemission matrix element effects that are present in ARPES data, the regions of maximum amplitude correspond to bands that have less k_z-dependence, and should account for features in the experimental data. The large width of 0.3 eV is chosen to account for the strong electron-(optical) phonon coupling in STO, which causes a significant 0.4 eV broadening of the quasi-particle peak.[117,121,138]

A similar analysis can be carried out using a tight-binding (TB) model for the band structure as seen in Figure 3.2 c). This tight binding model uses modified parameters from a previous work[121] which consist of the energy difference between the Ti 3*d* and O 2*p* energy levels, the crystal-field splitting of the Ti 3*d* and O 2*p* orbitals, hopping parameters between nearest neighbor Ti 3*d* and O 2*p* orbitals, and second and third neighbor hoppings

between O 2*p* orbitals. While there are subtle differences between the DFT and tight binding calculations, it will be shown that both are in reasonable agreement with ARPES data.

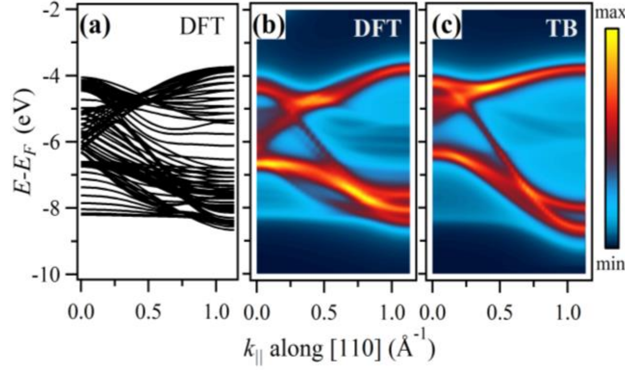

Figure 3.2. a) The surface projected band structure of bulk STO along the [110] direction for a fine grid of k_z values that spans the bulk Brillouin zone as calculated using DFT. b) For ease of comparison to ARPES data, each line in (a) is broadened using a Lorentzian function with a FWHM of 0.3 eV. c) Same as b), but calculated using a tight-binding (TB) model.

Figure 3.3 a) shows the ARPES intensity map for the vacuum-annealed sample. As shown in the literature,[112] a simple anneal results in large islands on the STO surface that are due to strontium oxide, or strontium hydroxide segregation.[104] These islands can serve as scattering centers for photoelectrons. Because photoelectrons can scatter off of these numerous islands, and lose their momentum signature, the ARPES data shows two regions of high photoemission intensity located at energies of E-$E_F \approx$ -5 and -7 eV which correspond to regions of high density of states for the primarily O 2*p*-derived valence band of STO. Captured in these measurements is some indication of the STO bandwidth, but because of the scattering, a study of the STO surface electron structure is problematic. There are, however very subtle features present in the ARPES data that correspond to photoelectrons which did not undergo scattering events. These features are only visible if one resorts to taking second derivatives of the photoemission spectra in the energy

direction, as shown in Figure 3.3 b), which shows some indication of several dispersing bands. The most notable of these bands, with an energy of E-$E_F \approx$ -3.75 and parallel wavevector of $k_{||} \sim 1$ Å^{-1}, corresponds to the top of the valence band near the bulk R point (labeled with a white arrow).

One way to remove the Sr-based islands is to dissolve them in DI water.[112,113] After water leaching, ARPES data reveals very apparent, dispersing features that correspond to the STO bulk band structure. These dispersing bands are even more obvious after removing a simple background from the ARPES data as shown in Figures 3.3 c) and d). This background removal was accomplished by integrating the photoemission data over the entire angular range. The resulting angle-integrated spectrum was then scaled, and subtracted from each constant emission angle spectrum, or energy distribution curve (EDC). After this background removal, the top of the valence band is again visible, as well as a downward dispersing band (both marked with white arrows) despite the fact that no 2nd derivatives have been taken. Another interesting feature of the ARPES data is the fact that the uppermost valence bands disperse downward as one goes away from Γ, in exactly the same fashion predicted by DFT (see Figure 3.2 b). It should be noted that this same background removal technique was not successful in the case of the vacuum-annealed sample because each EDC was very nearly identical due to the k-smearing resulting from scattering of photoelectrons off of surface defects. Finally, one consequence of this technique is that if a state is non-dispersing, it may be somewhat suppressed in the presentation of the dataset.

The surface preparations that yield the highest quality STO surfaces, and consequently give rise to the best ARPES data, are the preparations that etch the sample using either BHF, or the Arkansas preparation. The photoemission data for samples prepared using these two methods are shown in Figures 3.3 e)-h). For comparison of data

measured with a photon energy of $h\nu$ = 21.22 eV refer to Figures 3.3 c), e) and g), for the water-leached, BHF-prepared, and Arkansas-prepared samples respectively. It is immediately apparent that the samples which underwent etching (Figures 3.3 e) and g)) give rise to sharper photoemission features than the water-leached sample (Figure 3.3 c)). The presence of dispersing bands becomes much more apparent for a photon energy of $h\nu$ = 40.81 eV, which, roughly speaking, maps the band structure from Γ to M, as shown in Figure 3.1 b). Any of the subtle differences in the photoemission data for the BHF- and Arkansas-prepared samples is more likely related to data processing (primarily background subtraction) than an actual difference in surface quality.

The most likely reason for the improvement in ARPES spectra for samples that underwent surface preparations beyond the simple vacuum anneal is the removal of the strontium oxide islands on the surface. Evidence of this occurring can be seen in x-ray photoemission spectroscopy (XPS) studies shown in Figure 3.4. Figure 3.4 shows XPS spectra of the Sr 3*d* core level for the vacuum-annealed sample a) as well as for the sample etched in BHF b). At least two spin-orbit split doublets are required to fit the data with a structure-free residual. The more intense doublet corresponds to the primary STO lattice, and the less-intense doublet, with a slightly higher binding energy, has been attributed to strontium oxide crystallites, and the presence of F on the surface.[113,139,140] As seen in Figures 3.4 a) and b), there is a noticeable decrease in intensity for the higher binding energy doublet after etching with BHF—a clear indication that the concentration of strontium oxide crystallites on the surface has been reduced by the etch. Water leaching yields similar results, but the reduction in intensity of the higher binding energy doublet is not quite as pronounced as for the case of BHF etching.

Second derivatives of ARPES data for 10 unit cells of undoped STO grown on a Nb-doped STO substrate using MBE are shown in Figure 3.3 i). When compared to Figure

3.3 b), for the vacuum-annealed sample, it is obvious that the sample is of higher quality, with much more defined features. At this time, only a subset of data is available, but, as will be discussed later, there is some indication that the surfaces of MBE-grown films can be of equal quality to single crystals which underwent water leaching, or etching.

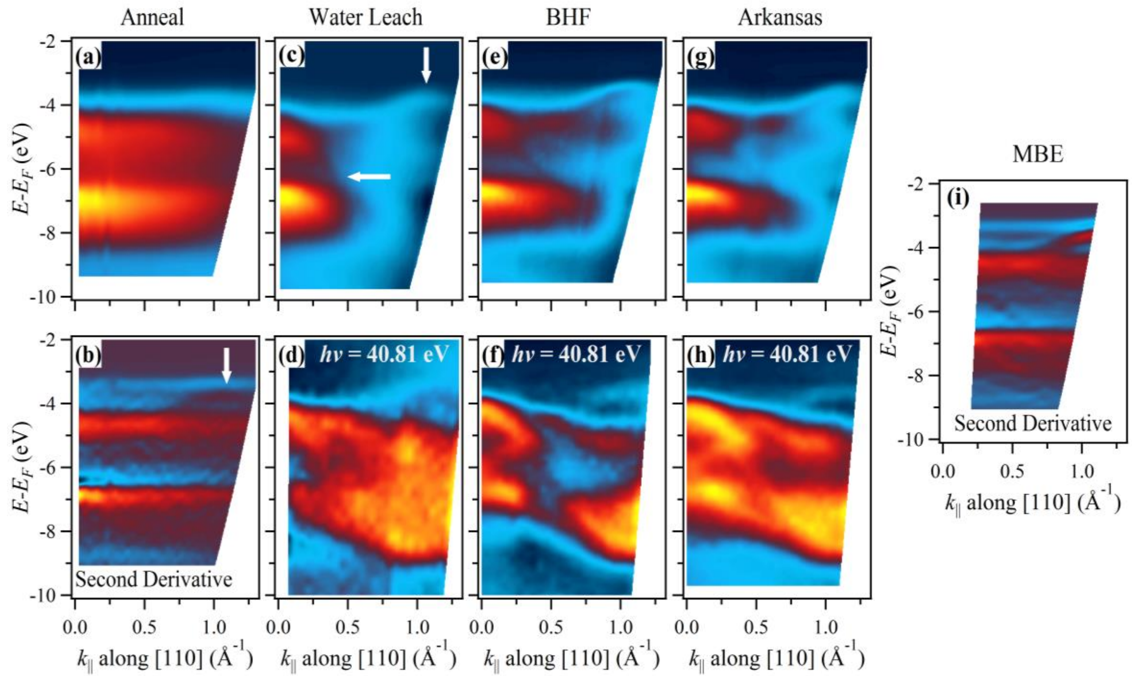

Figure 3.3. ARPES data along the [110] direction for STO samples prepared in a variety of ways for a photon energy of hv = 21.22 eV unless otherwise stated. a) Raw data for vacuum-annealed STO, with the 2nd derivative (in the Energy direction) shown in b) in order to better visualize dispersing bands. c), d) After water-leaching the STO surface quality is greatly improved and the ARPES data reveals dispersing bands after a simple background removal. Photoemission spectra (with background removal) for STO samples etched in e), f) BHF and those g), h) etched using the Arkansas method. i) The 2nd derivative of ARPES data for MBE-grown, undoped STO.

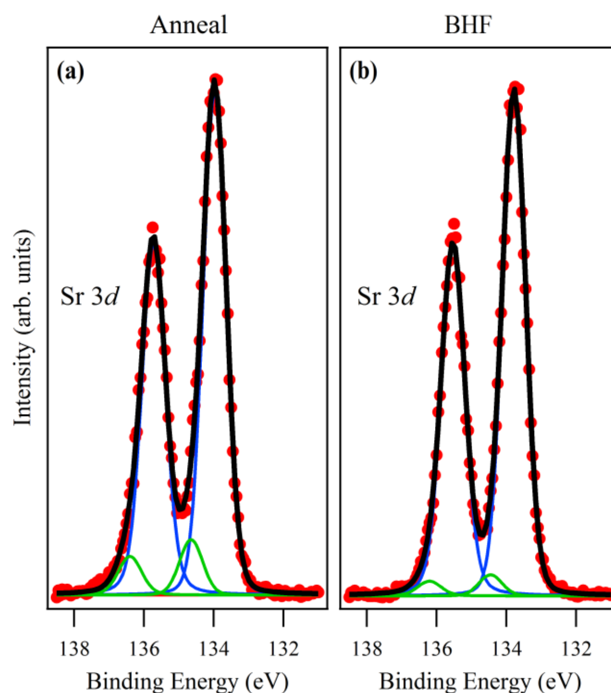

Figure 3.4. Normal emission XPS spectra of the Sr 3*d* core level for a STO(001) sample having undergone a) a vacuum-anneal b) as well as a sample etched in BHF. The primary STO lattice peaks (more intense) are accompanied by lower intensity peaks (green) which are attributed to the presence of strontium oxide crystallites on the surface which are removed, to some extent, after etching with BHF.

There are a number of photoemission features that are not apparent in Figures 3.3 a)-h) that are only apparent when looking at the energy distribution of the photoemission data. Figure 3.5 a) shows photoemission data for a variety of sample preparations that are integrated over a large emission angle of roughly 20°. The first obvious difference is the higher peak-to-valley ratio for the MBE-grown and Arkansas-prepared samples compared to the water-etched and vacuum-annealed samples. A second difference is the background level (i.e. the number of inelastically scattered photoelectrons) which is highest in the vacuum-annealed sample, then the water-leached sample, with the Arkansas-prepared and MBE-grown samples having the lowest, and very nearly identical backgrounds. These two photoemission characteristics are often associated with sample quality and indicate that surface-quality is best for etched and MBE-grown samples, followed by water-leaching

and finally vacuum-annealing. These conclusions are also in agreement with the quality of ARPES data shown in Figures 3.3 a)-i).

Different sample preparations also give rise to different gap states as shown in Figure 3.5 b). The most prominent gap state present in both the water-leached and vacuum-annealed samples is at an energy of E-$E_F \approx$ -1 eV. This state has been studied both experimentally, [86,114–118,141,142]and theoretically,[143–150] and is likely due to oxygen vacancies in the STO crystal, although it may be caused by a local screening effect, chemical disorder or donor levels (see Ref. [120] and references therein). The oxygen vacancy state for the water-leached sample has a higher spectral intensity than that of the vacuum-annealed sample and may be due to the slightly higher annealing temperature (775°C vs. 750°C) resulting in a higher concentration of defects. For etched samples (both BHF and Arkansas) there is another gap state located about 800 meV above the top of the valence band at an energy of E-$E_F \approx$ -2.75 eV. If this state is present for the water-leached sample it is not clear due to the higher spectral intensity in this energy range. As seen in Figure 3.6, this state is located in the gap region, and has basically no angular dependence. While the origins of additional gap states have been studied in the literature[120,123,124,151–155] the origins of this particular gap state have not been discussed, and must be related to the preparation of the surface using either of the two etching methods.

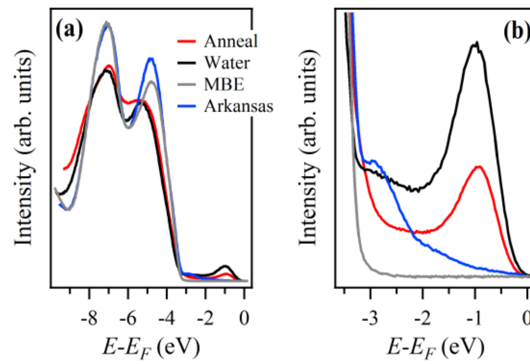

Figure 3.5. a) Angle-integrated photoemission data of the primarily O 2*p*-derived valence band states for a variety of STO preparations with b) a close-up of the gap region. Data for the BHF-etched STO is omitted from a) and b) since it is very nearly indistinguishable from the Arkansas-prepared STO. The photoemission data reveals at least two gap-states: an oxygen-vacancy state at a binding energy of $E\text{-}E_F \approx -1$ eV and another gap state about 800 meV above the top of the valence band located at $E\text{-}E_F \approx -2.75$ eV.

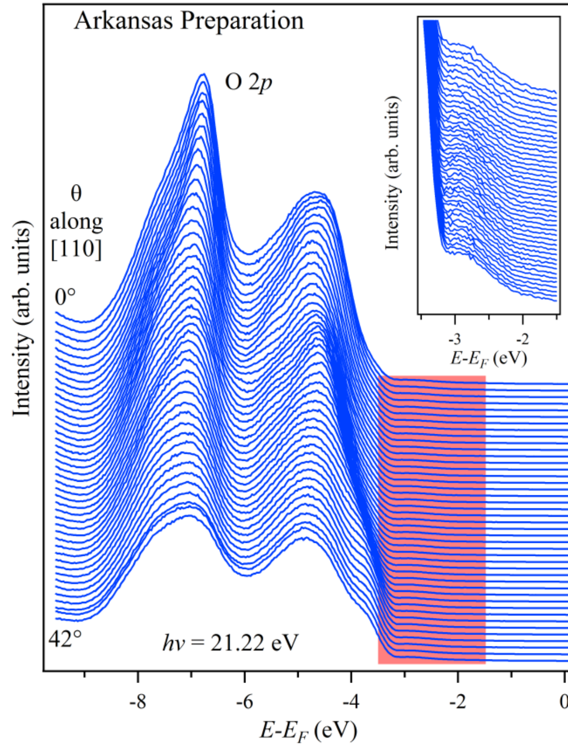

Figure 3.6. ARPES data for emission angles, θ, along the [110] direction for an STO sample prepared using the Arkansas method that correspond to the O 2*p*-derived valence band and the gap region. The pronounced shoulder for larger emission angles (at an energy of $E\text{-}E_F \approx -3.75$ eV) corresponds to the top of the valence band at the *R* point of the Brillouin zone. A close-up of the shaded region is shown in the inset and shows a mid-gap state about 800 meV above the top of the valence band that hardly disperses.

First-principles calculations of STO-based slabs can provide additional information about the electronic structure of prepared STO surfaces, and shed light on the origin of the gap state located at $E\text{-}E_F \approx -2.75$ eV. In addition to STO slabs with SrO- and TiO_2-terminations, a number of additional slabs are considered in this work, and are shown in Figures 3.7 a)-e), with their corresponding surface electronic structures shown in Figures 3.8 a)-g) respectively. The motivation of considering both F and H on the surface is the considerable experimental evidence that surprisingly high concentrations of these species can be found on the surface of STO.[113,156,157] The actual presence of F on the surface of our samples after various surface preparations was monitored using XPS. As seen in the XPS

spectra of Figure 3.9, there is possibly a trace amount of F present for all samples, but the actual concentration is noticeably less than what has been previously reported for BHF-etched samples.[113] As seen in Figure 3.8, much of the bulk-related electronic structure is not affected by different surface terminations, and surface adsorbates. The different surface configurations, however, do give rise to surface-related electronic states. One such state is the surface state seen in Figure 3.8 b) (TiO_2-terminated slab) that resides in the bulk gap, is about 980 meV above the upper-most valence bands, and whose dispersion follows that of the valence band top. The dispersion of this state of roughly 950 meV in the [110] direction precludes this as an explanation for the gap non-dispersing state located at E-E_F ≈ -2.75 eV in photoemission data. The reason this surface state is not present in the ARPES data for the TiO_2-terminated surfaces that result from various surface preparations is not immediately clear, but it is possible that, despite the care taken during surface preparation, there is simply too much surface disorder to support the development of surface states which can be notoriously sensitive to surface quality. It should also be noted that while our RHEED data does not indicate surface reconstructions, there have been numerous reports of reconstructed STO surfaces which may or may not give rise to surface states similar to the one in Figure 3.8 b).[158–163]

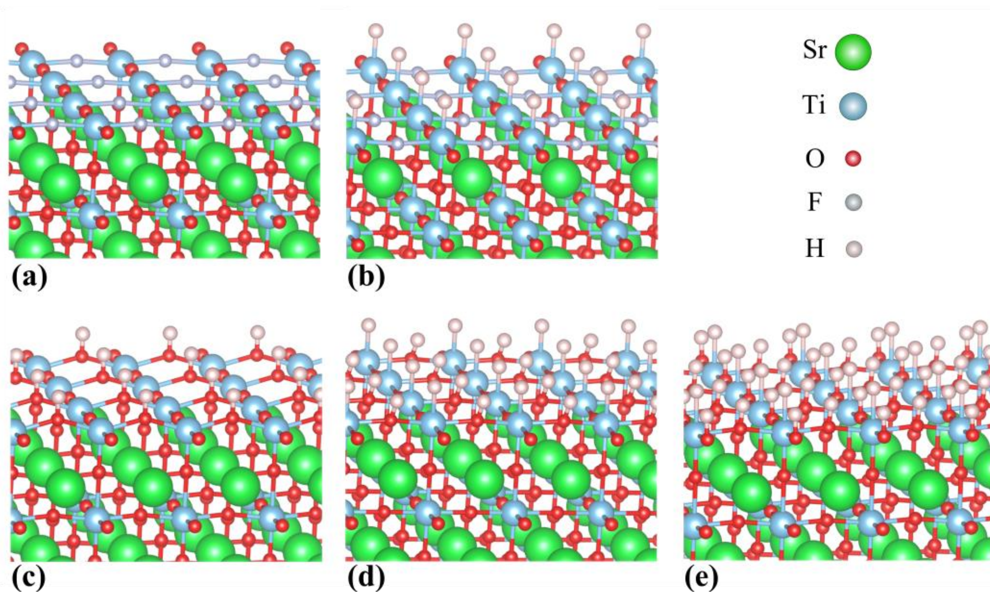

Figure 3.7. Sections of $SrTiO_3$ slabs corresponding to several of the systems studied using DFT calculations of the surface electronic structure. All slabs are (1×1). a) A TiO_2-terminated slab with one O replaced by F. b) Same as a) with the addition of a H bonded to Ti. c) A TiO_2-terminated slab with a single hydroxyl group. d) Same as c) with a H bonded to Ti. e) A fully hydrogenated slab with two hydroxyl groups, and a H bonded to Ti.

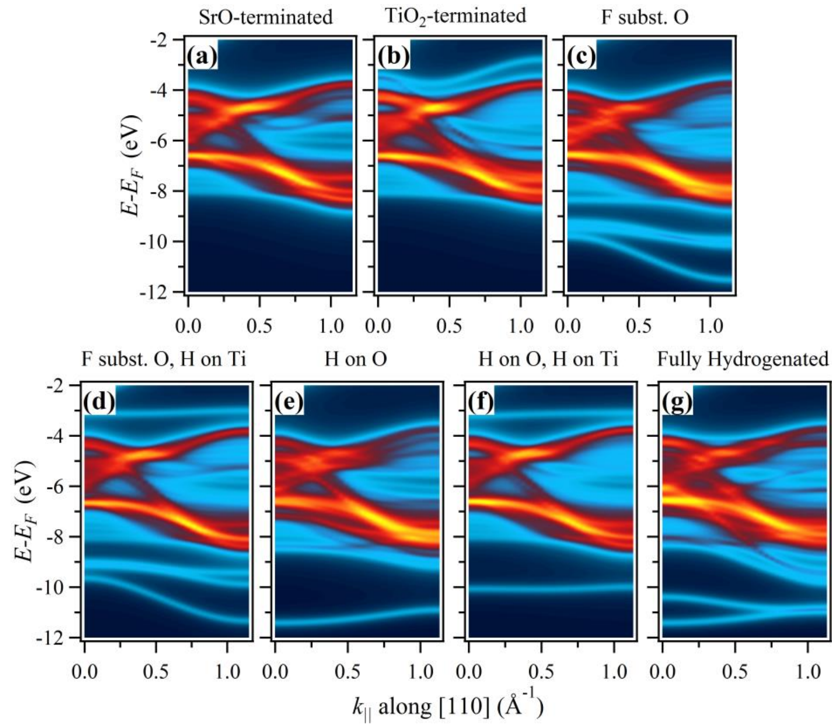

Figure 3.8. a)-g) DFT calculations of the surface electronic structure for bare SrO-and TiO_2-terminated slabs as well as slabs shown in Figures 3.7 a)-e) respectively. DFT calculations predict a pronounced, dispersing surface state about 980 meV above the valence band states that roughly follows the dispersion of the STO bulk bands which is not present in the case of an SrO-terminated slab. Because of the dispersing nature of the surface state in b), it is unlikely the origin of the mid-gap state discussed in Figure 3.6, despite the TiO_2-termination that results from the Arkansas preparation. As seen in d) and f), a likely explanation for this mid-gap state is the termination of the Ti dangling bond with H. As discussed in the text, for this termination to occur, it must be preceded by either a substitution of a surface O with F, or the formation of a hydroxyl group.

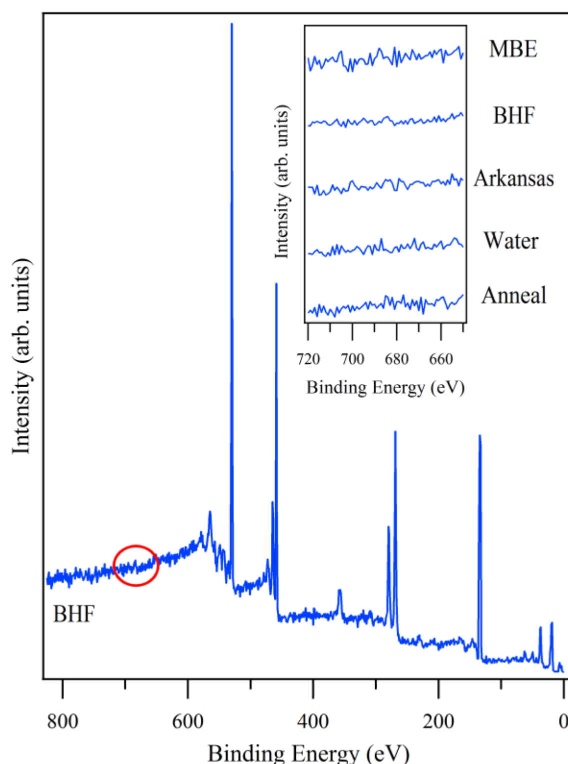

Figure 3.9. Normal emission XPS survey spectrum for a STO(001) sample prepared by BHF etching. The F 1*s* core level has a binding energy of ~685 eV, and, if present, should be located in the region highlighted with a red circle. Despite etching with BHF, the concentration of F on the surface is negligible (we estimate ≤ 1% of all anions within the probe depth). Other sample preparations yield equally low concentrations of F (see inset).

A more likely origin for the gap state at $E\text{-}E_F \approx$ -2.75 eV can be explained by DFT calculations for the slabs shown in Figures 3.7 b) and d). Calculations suggest that this non-dispersing state has its origin in the H-Ti bond present in both of these slabs, and that the H-Ti bond is unlikely to form without additional modifications to the surface. The first scenario considered, that enables the H-Ti bond, is shown in Figure 3.7 b), where one surface O is substituted by F. Theory shows that, in the presence of this substituted F, the H will not remain at an O site and relaxes to the Ti site. Theoretical calculations for this slab are shown in Figure 3.8 d) and show the presence of states both above and below the STO valence band. The non-dispersing, localized state that is ~810 meV above the top of the valence band originates from the H-Ti bond which is consistent with previous

findings.[58] The energy of this state, as well as its dispersive character, is virtually identical to the gap state seen in the photoemission data. The charge density of this non-dispersing state is shown in Figure 3.10 a). It is obvious that this state is highly localized on H and Ti, with some charge on the neighboring O. There is no charge density on the F substituted on the surface. The second scenario that enables this H-Ti bond is shown in Figure 3.7 d) where one H and one O form a hydroxyl group, and an additional H bonds to the Ti. For this system the same non-dispersing state is present (see Figure 3.8 f)) which has a very similar localized charge density (Figure 3.10 b)). Similar to the first scenario, the introduction of a single H to the surface will first form a hydroxyl group, but with the addition of a second H, the formation of the H-Ti bond is energetically more favorable than the creation of a second hydroxyl group. A further confirmation of this non-dispersing state having its origin at the Ti-H bond is the fact that neither a F-O substitution (first scenario and Figure 3.8 c)) nor the formation of a single hydroxyl group (second scenario and Figure 3.8 e)) alone give rise to this state—it only appears after the formation of a H-Ti bond (see Figures 3.8 d) and f)). It should also be noted, that it is not necessary for every surface unit cell to have adsorbed H, in order for the non-dispersing state to be present. DFT calculations reveal the presence of this non-dispersing state for surfaces where only one in four surface unit cells has both a single hydroxyl group and a H-Ti bond (results not shown). There are also a number of surface modifications that result from H adsorption. The calculated ionic reconstruction due to different coverage of H is given in Table 3.1. An obvious trend is that when H bonds with either O or Ti, O or Ti rises out of the surface relative to the original clean surface of TiO_2. A surface-sensitive technique, such as surface X-ray diffraction could be sensitive to these ionic reconstructions, assuming a sufficient number of surface unit cells have the presence of adsorbed H. Furthermore, the presence of both hydroxyl groups, as well as H-Ti bonds on the surface could be verified by their vibrational signature, which could be studied with attenuated total reflection Fourier transform infrared spectroscopy. In light of these DFT calculations, a more likely explanation for the absence of the dispersing surface state seen in Figure 3.8 b), is the presence of adsorbed H on the STO surface, which serves to kill this dispersing state. This

dispersing state is comprised entirely of surface O *p*-states, and is destroyed by the presence of H, which buries the energy levels of both surface O bands deep in the valence band. Similarly, fully hydrogenating the STO surface leads to an energy shift of the non-dispersing, flat band found in Figure 3.8 f); the flat band is actually still present, but it gets pushed down in energy and is found now within the bulk valence band states, and becomes difficult to observe with ARPES.

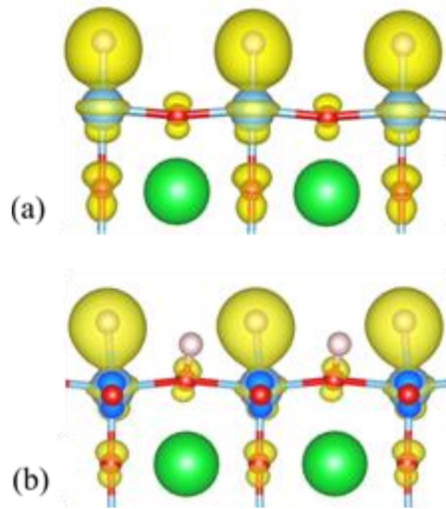

Figure 3.10. a) The charge density of the non-dispersing band for the F-substituted slab with H on Ti. There is no charge density on the F (not shown). b) The charge density of the nondispersing band for the H on O, H on Ti slab.

H present	Layer 1 Ti	Layer 1 O a*	Layer 1 O b*	Layer 2 Sr	Layer 2 O
O-H	0.02	0.48	0.03	-0.30	0.07
O-H, Ti-H	0.11	0.24	-0.15	-0.17	-0.02
2 O-H, Ti-H	0.11	0.24	0.24	-0.30	0.10

*O a corresponds to the O that is bonded to the first H. O b corresponds to the O bound to the second H (2 O-H, Ti-H surface only).

Table 3.1. The ionic motion (Å) of hydrogenated surfaces with respect to the clean TiO_2 surface. A positive number means the ion is moving towards vacuum, and a negative number means the ion is moving towards the bulk.

In Figures 3.8 c) and d), it is likely that the states below the valence band, with an energy of E-$E_F \approx$ -9 to -12 eV, are related to the presence of fluorine on the surface. This assignment is also supported by XPS data from a previous work which shows an increased spectral intensity below the valence band for samples etched in BHF, which have, on average, a ~13% fluorine for oxygen substitution on the surface.[113] Furthermore, recent photoemission data on STO exposed to a 4000 L H-dosage (1 L = 9.75×10^{-7} Torr s) also shows an increased spectral intensity below the valence band and suggests that the states below the valence band in Figures 3.8 e)-g) are related to the adsorption of H.[123,124] DFT calculations show that these low bands belong to the O p-states, whose energies are pushed down due to the ionized H^+ of the hydroxyl group formed at the surface; note that in Figures 3.8 e) and f) there is one low band present corresponding to the hydroxyl group, and in Figure 3.8 g), there are two low bands corresponding to the two hydroxyl groups present on the surface. The DFT calculations also suggest that the low energy bands in Figure 3.8 d), originate from the F p-states.

What likely occurs during sample etching, with both BHF and the Arkansas method, is a partial hydrogenation of the STO surface, and the formation of a H-Ti bond, in much the same fashion that the dangling bonds on Si surfaces are passivated with H when etched with BHF (see, for example Ref. [164] and references therein). This H-Ti bond on the STO surface then gives rise to this non-dispersing gap state present in the photoemission data. If this gap state is indeed related to the hydrogenation of the STO surface, as theory suggests, there are two consequences. First, the hydrogenation is surprisingly thermally stable, and the state remains unchanged even after a 4 hour anneal at 875°C. This is in strong contrast to the case of Si, where all H is desorbed from Si surfaces with an anneal of less than 600°C.[165] Second, as DFT does not predict a non-dispersing state in the gap for a fully hydrogenated surface (see Figure 3.8 g)), a third H approaching the surface must encounter a relatively large potential barrier, making the complete hydrogenation of the surface unlikely. To quantify these results, the energy of a slab shown in Figure 3.7 c) (the slab with one O-H group) with a H_2 molecule located far in vacuum, is compared with the slab in Figure 3.7 d) (which contains an O-H group and a

H-Ti bond). The slab in Figure 3.7 d) is lower in energy by 0.152 eV per cell, suggesting that, in the presence of H_2, the surface will prefer to break the H_2 and have the H atoms attach to Ti sites. However, when one compares the slab in Figure 3.7 d) with a H_2 molecule located far in vacuum to the slab in Figure 3.7 e) (the fully hydrogenated surface), one sees that the H_2 molecule plus the slab in Figure 3.7 d) is lower in energy by 0.543 eV per slab indicating that the fully hydrogenated slab is not energetically favorable. Thus, it is expected that in the presence of sufficient H_2, the surface will hydrogenate until each TiO_2 surface unit has one O-H and one Ti-H bond, but will not fully hydrogenate, which may explain why many of the ARPES images show this flat band that is not present in DFT calculations for the fully hydrogenated surface.

A thorough comparison of different theoretical calculations and ARPES data is shown in Figure 3.11. To facilitate the comparison, prominent features in the bulk calculations are highlighted with white circles in Figure 3.11 a). These same white circles are then overlaid on other calculations, and on the ARPES data. It is interesting to note that the theoretical calculations for bulk STO account for virtually all observed ARPES features corresponding to the STO valence band for photon energies of $h\nu = 40.81$ and 21.22 eV as seen in Figures 3.11 i) and j), even though all photoemission matrix elements effects have been ignored. Furthermore, the overall bandwidth, of ~4.8 eV is in perfect agreement with DFT calculations, and in reasonable agreement with tight-binding calculations.

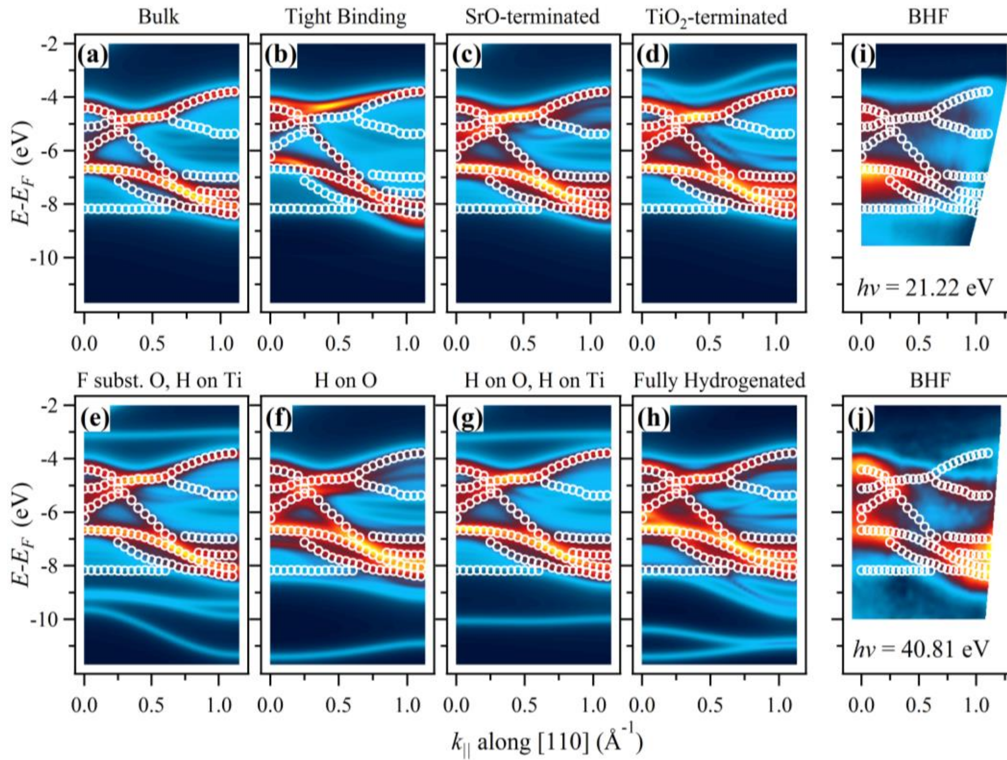

Figure 3.11. Comparison of theoretical calculations for various STO systems with ARPES data for the BHF-prepared sample. a) The calculation for bulk STO band structure (see also Figure 3.2 a)-b), where prominent features are highlighted with white open circles. For ease of comparison, these same open circles are overlaid on the data in b)-j) which corresponds to data in Figure 3.2 c), Figures 3.8 a), b), d)-g) and Figures 3.3 e), f) respectively. It is apparent that the different STO terminations hardly affect band structure predicted by DFT bulk calculations, but can give rise to surface states both above and below the valence band as seen in d)-h).

3.1.3 Conclusion

High-resolution ARPES measurements showed that a simple degreasing of STO single crystals, accompanied by a subsequent anneal in UHV is not an adequate surface preparation of STO. Other surface preparations such as MBE growth, the Arkansas method, or etching with BHF, and to a lesser extent, simply leaching the STO with water result in surfaces with much less disorder. It was also found that ARPES was an excellent probe of surface disorder.

Density functional theory calculations for bulk STO account for virtually all dispersing features in the ARPES data. A tight-binding model of the band structure, while in reasonable agreement with ARPES data, is not quite as successful as the DFT calculations. The agreement of tight-binding calculations with ARPES data may be improved with additional, fine tuning of the tight-binding parameters.

Using ARPES to study the gap region showed that gap states depend strongly on surface preparation methods. A non-dispersing oxygen vacancy state, located ~1 eV below the Fermi level, is present in vacuum-annealed and water-leached samples, whereas a non-dispersing, mid-gap state was found ~800 meV above the top of the valence band for samples which underwent etching. In contrast, MBE-grown thin films show very little indication of any gap states. This suggests that it should be possible to use different surface preparations to tailor interface properties between STO and other complex metal oxides, and it would be interesting to explore what affect, if any, different STO surface preparations have on the 2DEG at the interface of $LaAlO_3$ and STO. Theoretical modeling of STO slabs using DFT within the LDA for the exchange correlation, indicates that the mid-gap state is not related to the SrO- and TiO_2-terminated surfaces, but rather, due to a partial hydrogenation of the STO surface that occurs during etching. A theoretical study of the charge density for this non-dispersing, mid-gap state shows that its origin lies in the formation of a H-Ti bond on the TiO_2-terminated STO surface. Further theoretical studies of surface properties show that for this H-Ti bond to form it must be preceded by either a F substitution of a surface O, or the formation of a single hydroxyl group on the 1×1 surface unit cell. These two surface-modifications that enable the H-Ti bond to form both give rise to electronic states just below the STO valence band. The H-Ti bond is very thermally stable, and is not broken even with an anneal of 875°C.

3.2 THE $BaTiO_3$(001) SURFACE

3.2.1 Computational Details

DFT was used to model the bulk and (001) surface of BTO. All calculations were done using the local density approximation and projector augmented-wave pseudopotentials as included in the VASP code.[65,66,131–134] We used the Perdew-Zunger form of the exchange-correlation potential.[135] The valence configuration of $3p^6 4s^2 3d^2$ was used for Ti, $5s^2 5p^6 6s^2$ for Ba, $2s^2 2p^4$ for O, and $1s^1$ for H. A kinetic energy cutoff of E_{cutoff} = 600 eV was used. For the Brillouin zone integration, the following Monkhorst-Pack[136] *k*-point meshes were used: 8×8×8 for bulk BTO, 8×8×1 for the (1×1)-terminated TiO_2 surface, and 6×6×1 for the (√2×√2) surface. Bulk BTO was optimized, and all structures were optimized with respect to the ionic positions until the forces on all atoms were less than 50 meV/Å. The energy was converged to 10^{-3} meV per atom. The lattice constant *a* of tetragonal BTO was calculated to be 3.96 Å, with a *c/a* ratio of 1.005, in good agreement with an experimental *a* of 3.99 Å and *c/a* ratio of 1.011,[166] and previously reported theoretical values of 4.00 Å and *c/a* = 1.010.[167] All slabs were symmetrically terminated with TiO_2, with the slabs being 10.5 UC thick, augmented by 15 Å of vacuum. Following previous work on the STO(001) surface,[58,59] we consider O and Ti as possible adsorption sites for H.

3.2.2 Electronic Structure

First, we examine the (1×1) surface. The electronic structure of the system is given in Figure 3.12. In Figure 3.12 a), we see that the Ti surface states are located in the middle of the conduction band, and are not particularly distinct from them. In Figure 3.12. b), we can see there is a mid-gap state that is mainly due to the surface O, which is very similar to that of the STO surface. This state extends to ~1.5 eV above the top of the valence band of the bulk O state. Although this state is higher energy than the bulk, it is lower than the

conduction band bottom and the surface remains insulating. Our results are in good agreement with prior calculations of the BTO(001) surface.[168]

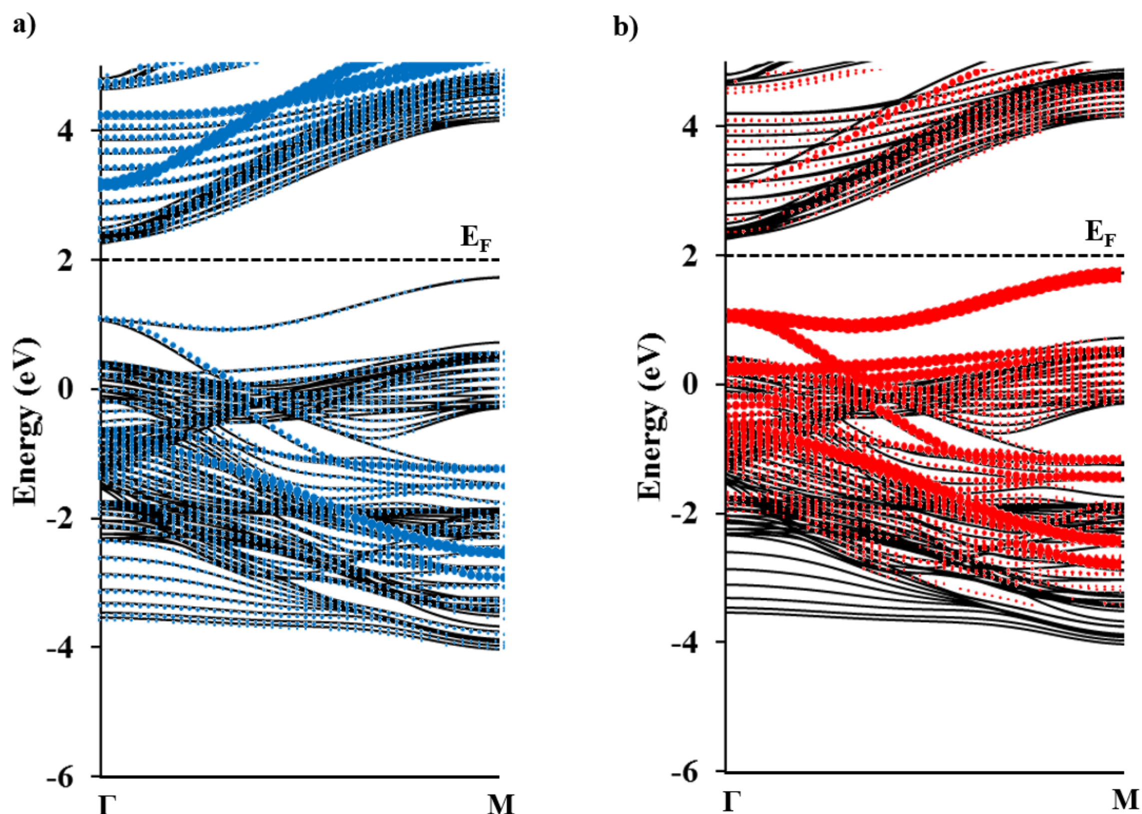

Figure 3.12. The band structure of the clean TiO_2-terminated surface. The Fermi energy is indicated with a dotted line. a) The contribution of the surface Ti atom is shown in blue. b) The contribution of the surface O atoms are shown in red.

This surface gives us three possible adsorption sites; one Ti, and two inequivalent O sites. The order of adsorption is given in Figure 3.13. First, the H adsorbs on one of the O sites, creating an OH complex. The electronic structure for this adsorption is shown in Figure 3.14. Immediately we see a large change in the electronic structure. First, we note that the Fermi energy is now in the conduction band, indicating that the surface is metallic. We also notice that the mid-gap surface state of the clean surface is absent; this is in contrast with the case of STO, in which the surface state of O is altered, but still distinct

from the rest of the valence band. In Figure 3.14 a), we see that the charge obtained from the adsorbed H is present mostly on the surface Ti state, which has been lowered from the middle of the conduction band and now forms the bottom of the conduction band. In Figure 3.14 b), we see the contribution of O in the OH complex; we see that this state has been lowered from the mid-gap state to a weakly-dispersive state below the valence band. In Figure 3.14 c), we see that the H contribution is solely due to this sub-valence band state; however, due to the metallicity of the surface, we also conclude that while some of the charge remains on the OH group, a significant amount enters the conduction band of BTO. We can view the change in charge density in the system (Figure 3.17 a)) by the following method: We take the charge density of the 1H adsorbed system, and subtract the charge density of the isolated slab, and isolated H atoms, from a separate calculation. We use the same relaxed atomic positions as for the H adsorbed case, which guarantees that any change in charge density is not due to ionic motion. We see that there is a gain in charge density between the O and H, indicating an O-H bond, and that there is also a gain in charge density on the Ti surface sites, indicating that charge is entering the conduction band.

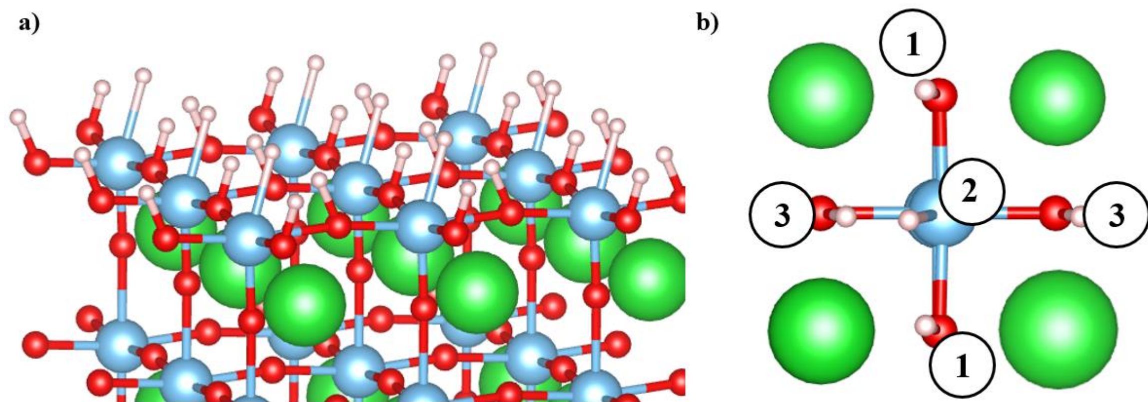

Figure 3.13. a) The TiO_2-terminated surface, with 3 H adsorbed. b) The order of adsorption. 1) H adsorbs on one of the O sites. 2) H adsorbs on the Ti site. 3) H adsorbs on the remaining O site.

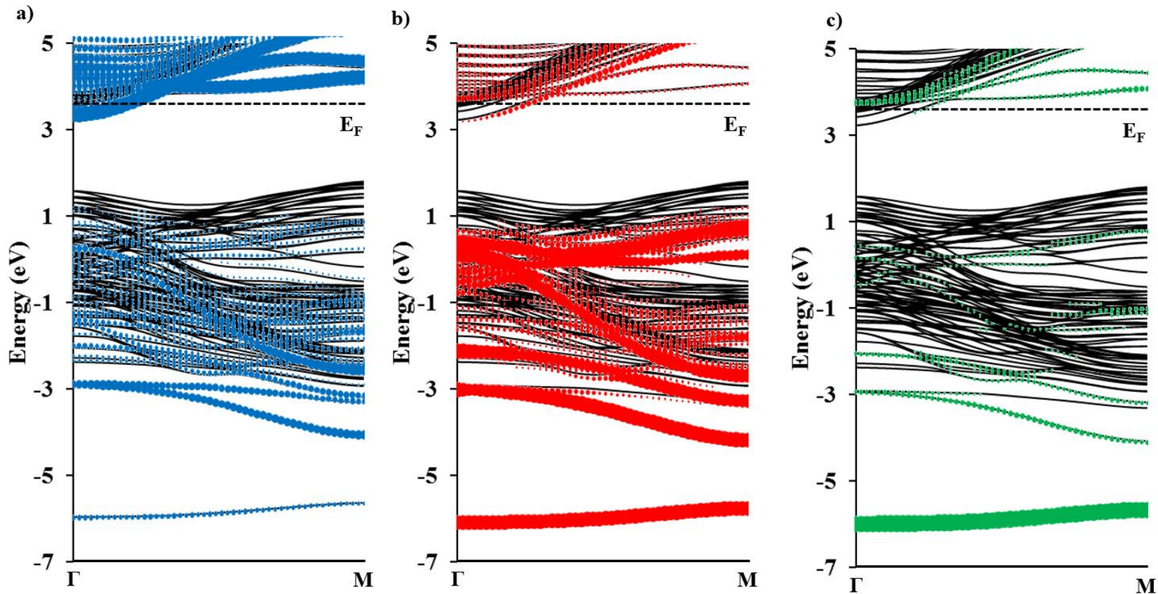

Figure 3.14. The band structure for the H adsorbed (1×1) surface. a) The surface Ti contribution in blue. b) The O of the OH complex contribution in red. c) The adsorbed H contribution in green.

Now, when we add the second H to the BTO surface, it adsorbs on the Ti site; the Ti-H bond length is 1.76 Å. In Figure 3.15, we plot the band structure of this surface. Again, there are obvious differences for the adsorption of two H atoms than for the adsorption of only one. The surface is again insulating, and the Fermi level is pinned by a nondispersive midgap state. Examination of Figure 3.15 a) shows that the surface Ti contribution is in the conduction band, where the states are again moved up in the middle of the conduction band; there is also some contribution to the mid-gap state. Figure 3.15 b) shows that there is no significant change between the O in the OH group than from the surface with one adsorbed H. Finally, Figure 3.15 c) shows that the H contribution is in the mid-gap state and the sub-valence band state, corresponding to the TiH and OH group respectively. The return of an insulating surface, simultaneous with the essentially unchanged condition of the OH group, shows that any charge donated to the system from the OH complex must be balanced by any charge accepted by the TiH complex. In Figure 3.17 b), we see an increase in charge density on the H in the TiH complex, agreeing with our assessment that the H is adsorbing charge from the system. This can be explained by back-donation;[58,169] the H

adsorbed by O in the 1H case donates charge to the system, which settles in the surface Ti *d* states. This allows Ti to become more chemically active, which attracts H; the adsorbed H in the TiH complex then appropriates the charge from Ti, which causess the system to become insulating.

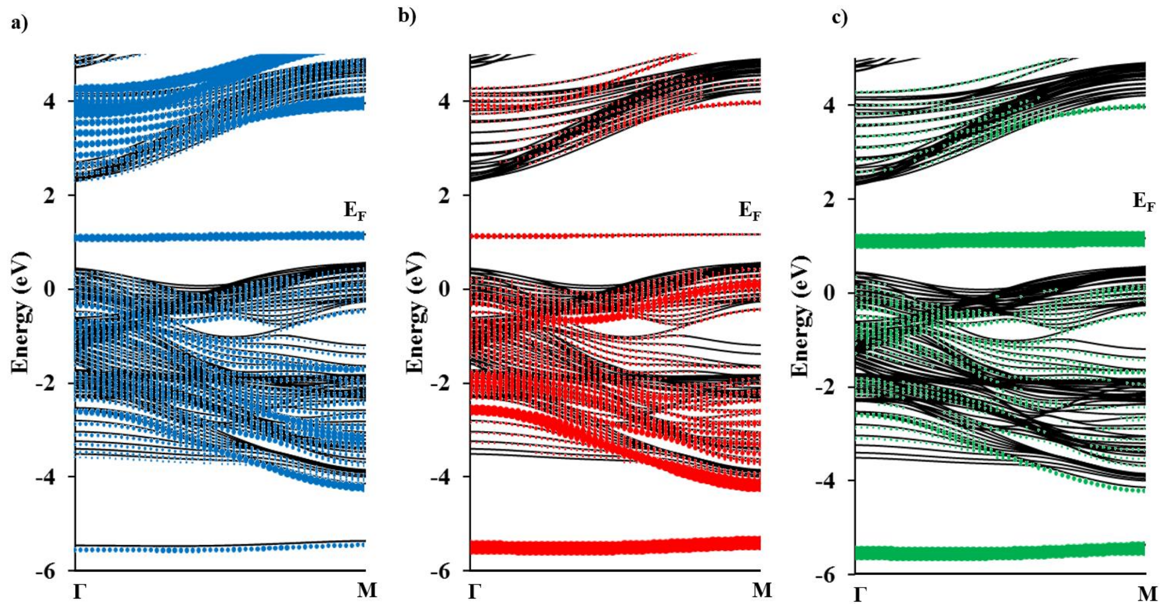

Figure 3.15. The band structure for the 2H adsorbed (1×1) surface. a) The surface Ti contribution in blue. b) The O of the OH group contribution in red. c) The adsorbed H contribution in green.

Finally, we occupy the last O site and the surface is fully hydrogenated. We show the electronic structure of the system in Figure 3.16. Again, the system returns to being metallic; the overall band structure looks quite similar to that of the one H adsorbed case, with the expectation of being two sub-valence states. In Figure 3.17 a), we see that the Ti conduction bands have yet again been lowered to the bottom of the conduction band. Figures 3.17 b) and c) look essentially the same as for the one adsorbed H case, except for the doubling of O and H sub-valence states. There is an interesting H contribution found near the M point, in the center of the valence band, this is due to the H bonded to Ti. This state is in a different place than in the 2H case, where the state is midgap. Also, there are

very few states of the surface Ti at this H state, indicating that Ti and H hybridize only weakly. The Ti-H bond length is increased to 1.94 Å, a 0.18 Å change from the Ti-H complex for the 2H case. The change in bond Ti-H bond length and hybridization can be explained as follows. We examine the charge density difference in Figure 3.17 c) and see that there is a gain in charge density for the H in the TiH complex. The third H bonding with O again donates charge to the system, which is then again appropriated to the H in TiH complex, which weakens the bond between Ti and H, leading to an increased bond length. However, the charge donated to the system is not entirely adsorbed by the H in the TiH complex, and some remains in the conduction band of STO.

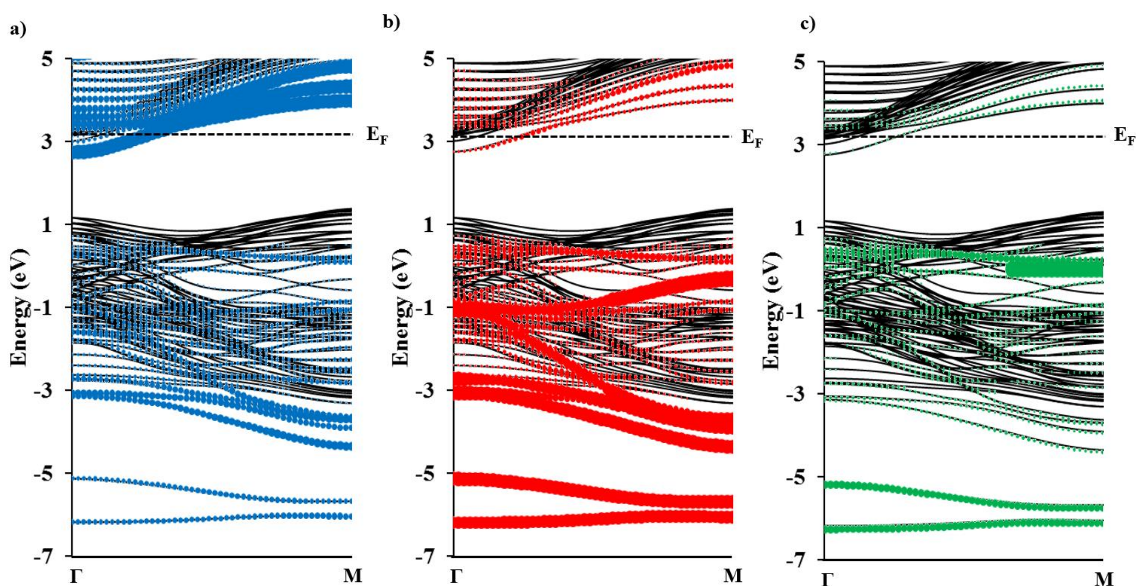

Figure 3.16. The band structure for the 3H adsorbed (1×1) surface. a) The surface Ti contribution in blue. b) The surface O contribution in red. c) The H contribution in green.

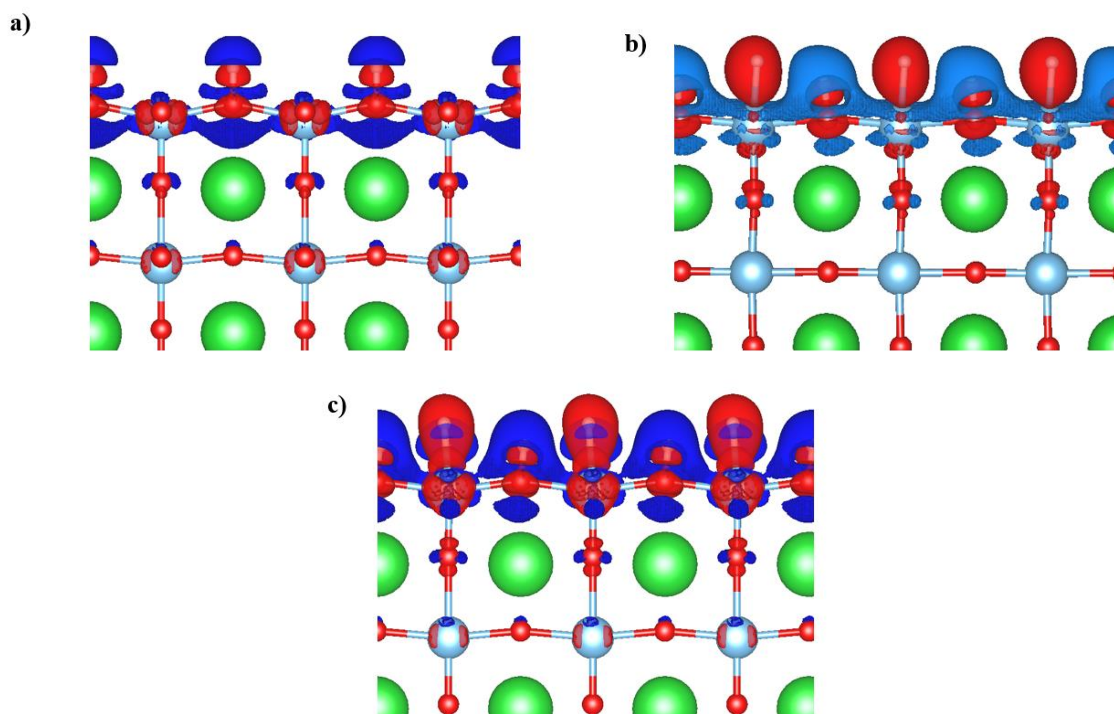

Figure 3.17. The charge density difference plots for the a) 1H, b) 2H and c) 3H cases. The red indicates an increase in charge density, and the blue indicates a decrease in charge density.

Now, we will examine the adsorption of H on the BTO(001) surface, but with a larger surface area. We use a ($\sqrt{2}\times\sqrt{2}$) surface, which allows for six distinct adsorption sites; two Ti, and four H. We adsorb four H on the surface; the order of adsorption is shown in Figure 3.18.

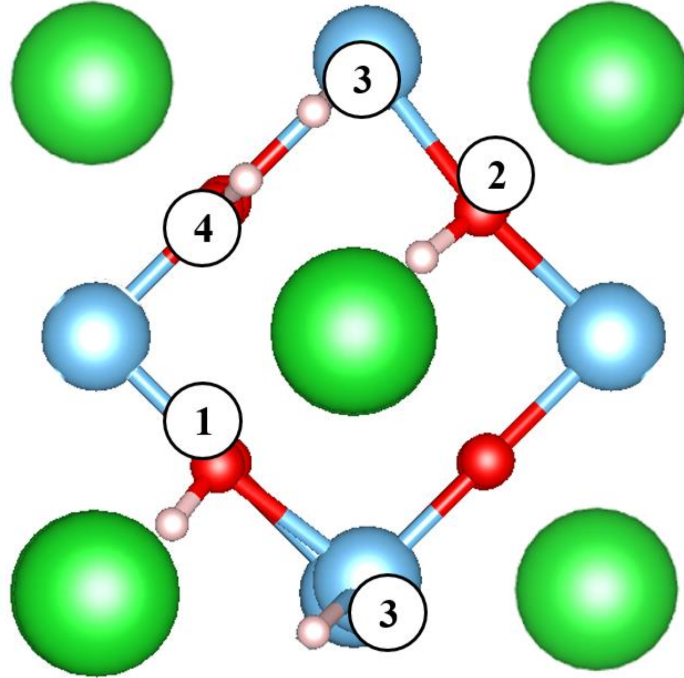

Figure 3.18. The order of adsorption for the (√2×√2) surface. 1) The H adsorbs on an O site. 2) The H adsorbs on another O site, farthest from the original OH complex. 3) The H adsorbs on one of the Ti sites. 4) The H adsorbs on one of the other free O sites.

The band plots for the 1H and 2H adsorption are essentially the same as those for the 1H case on the (1×1) surface, and are not shown here. The 3H case is shown in Figure 3.19; in this case, there are two H adsorbed on O and one on Ti. We see that this is different than the 2H case with the TiH complex, because the system remains metallic and does not become insulating as in the previous case. This is due to the fact that there is a two to one ratio of OH complexes versus TiH complexes, in contrast to the (1×1) surface, where the charge donated by the OH complex is balanced by the charge accepted by the TiH complex. Thus, as we can see in Figure 3.19 a), the electronic structure is a mix of the 1H and 2H cases on the (1×1) surface; the Fermi level is in the conduction band, but there is still a strongly localized TiH state located midgap.

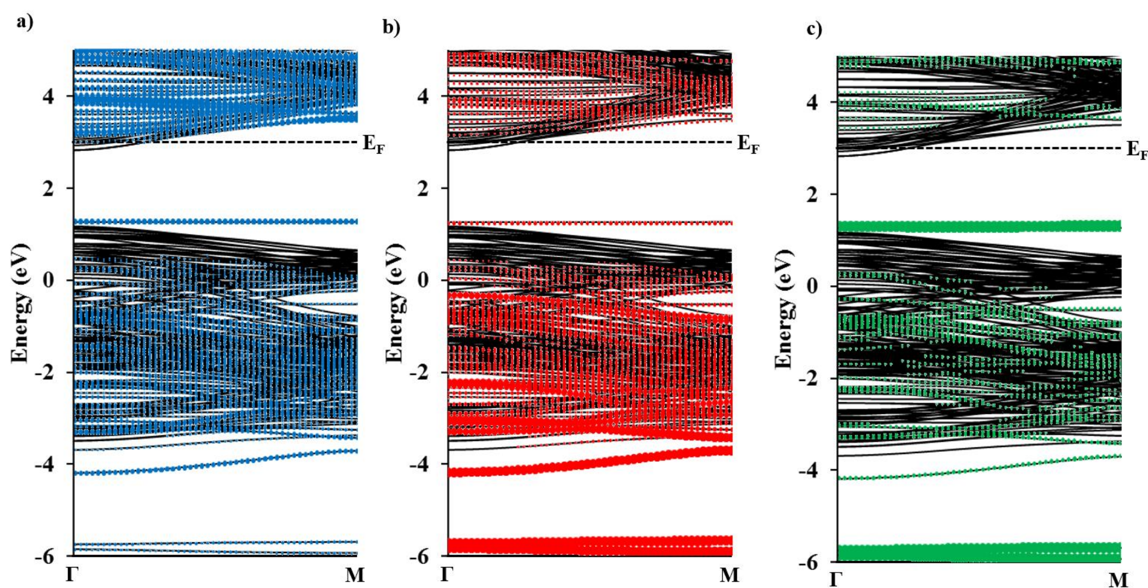

Figure 3.19. The band structure for the 3H adsorbed (√2×√2) surface. a) The surface Ti contribution in blue. b) The surface O contribution in red. c) The H contribution in green.

Finally, we add a fourth H to get the 4H surface. From the previous calculation on the (1×1) surface, we expect that we will have two OH complexes and two TiH complexes; however, this is not the case for the (√2×√2) surface, where we form three OH complexes and one TiH complex. In Figure 3.20, we see that the system essentially resembles that of the (1×1) 3H surface; the Fermi level is in the conduction band, and Figure 3.20 a) shows that the surface Ti states are brought down in energy and occupied, as before. The Ti-H bond length is 1.91 Å, increased from the prior bond length as before, indicating that the same charging mechanism in the Ti-H complex is occurring here as it did for the (1×1) case. The key difference between the (1×1) and the (√2×√2) surface is that the insulating surface never occurs, as it does for the (1×1) surface; the system always stays metallic, due there being an uneven number of TiH and OH complexes.

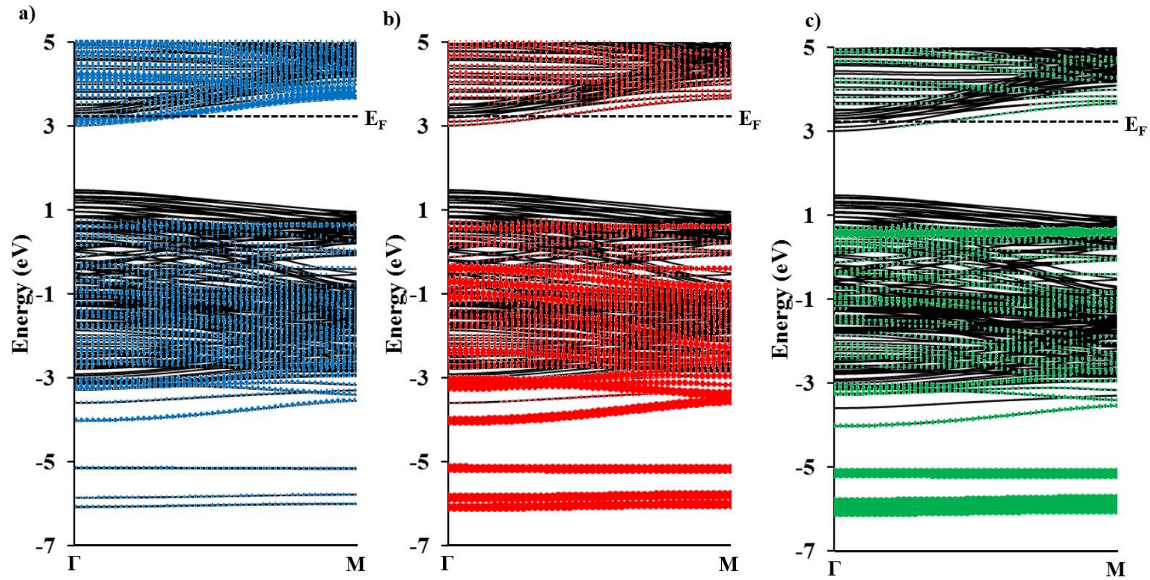

Figure 3.20. The band structure for the 3H adsorbed (√2×√2) surface. a) The surface Ti contribution in blue. b) The surface O contribution in red. c) The H contribution in green.

3.2.3. Rumpling

We would also like to see the effect of H adsorption on the polarization of BTO. The rumpling is defined by the relative shift in the z direction (perpendicular to the surface) of the Ti and O atoms. As a good approximation, the polarization in linear with respect to the rumpling,[83] so examining the rumpling is a simple way of approximating the effects of adsorbed atoms on the system polarization. The rumpling for the clean surface and adsorbed H are given in Figure 3.21 a). We see that the rumpling of the surface layer is roughly equal to that of the bulk, but it dies very rapidly and the majority of the system has no rumpling.

Now, we see the effect of adsorbed H on the surface. The rumpling is shown for the one adsorbed H surface in Figure 3.21 b). We see that the rumpling for the O with H adsorbed is massively enhanced at the surface (red line), reaching roughly 4 times the bulk

value. Although the O without H adsorbed (blue line) is increased near the surface, it is not as large. Three layers from the surface, the rumpling for both O become the same for the thickness of the slab. In Figure 3.21 c), we see that although the rumpling is increased at the surface, it dies quickly and the rest of the TiO_2 layers become flat, essentially the same as the clean surface. Also, the first two layers of this slab show mixed termination (the rumpling for the different O are opposite). Finally, in Figure 3.21 d) we see that the rumpling is again increased with respect to the clean surface, similarly to the case with one adsorbed H. We also see that, even though the entire surface is hydrogenated, the two O do not have equal rumpling. An important note, is that the 1H and 3H adsorbed systems having rumpling enhancements that penetrate the entire slab (the center of the slab is flat, as it must be due to symmetry). In other words, the rumpling enhancement of H is not purely a surface effect.

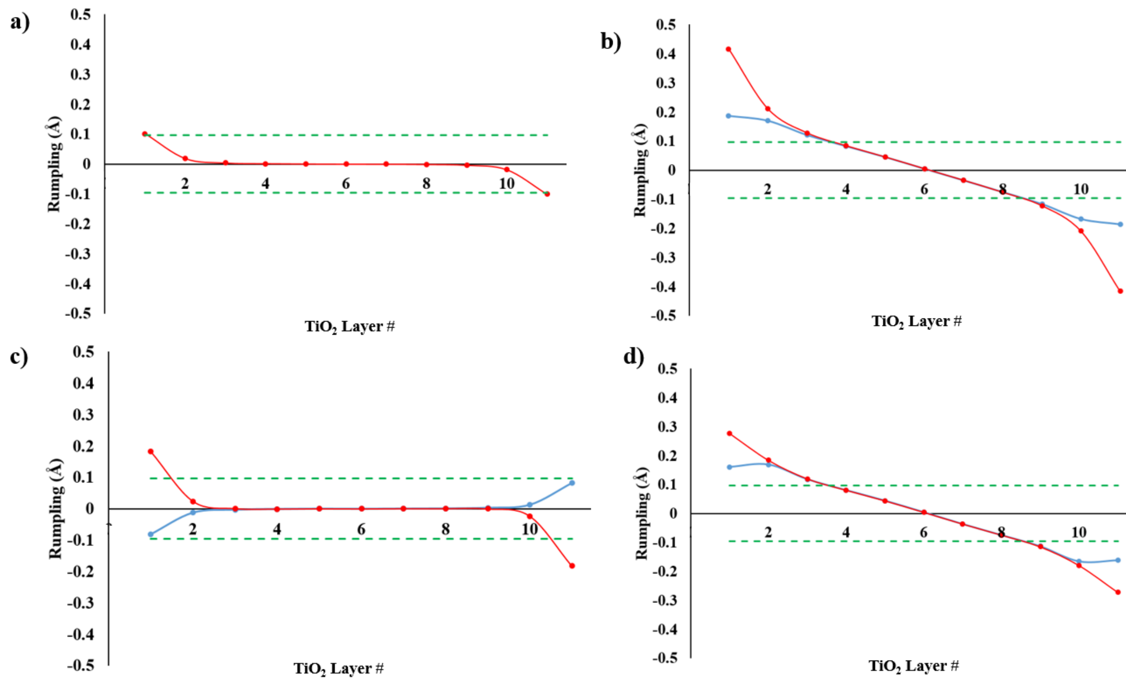

Figure 3.21. The rumpling of the TiO_2 layers for a) the clean BTO(001) surface, b) the 1H adsorbed surface, c) the 2H adsorbed surface and d) the 3H adsorbed surface. The green dotted line is the rumpling of bulk BTO. In b) and c), the red represents the rumpling between the O with adsorbed H and Ti, and the blue represents the rumpling between the O without adsorbed H and Ti. In d), although both O have adsorbed H, their rumpling is inequivalent near the surface.

The reason for the rumpling can be explained by an electrostatic argument. The slab with no H adsorption is essentially unrumpled, because the cost of the electric field caused by the polarization of the system is large. However, in the 1H case, when the electron from H pours into the system, the bare H adsorbed on the surface is positively charged and no longer screened by the electron present in atomic H, so it creates a large electric field pointing away from the surface and toward the bulk. To combat this large field, the electrons present in the conduction band have the ability to partially screen this field; however, the Ti and O have the ability to polarize in order to reduce this field as well. In the 2H case, all the charge remains at the adsorbed H (the charge donated by the OH group

is accepted by that of the TiH group), so that there is no bare H charge and no field, so no polarization of the BTO develops. The 3H case is essentially the same as that for the 1H case. Thus, we see that the polarization developed by BTO is due to screening of the protons adsorbed on the BTO surface.

Next, we examine the rumpling of the (√2×√2) surface, given in Figure 3.22. The surface rumpling is complex, due to the many possible combinations of rumpling given by the inequivalent four O and two Ti sites, but we see that regardless, rumpling is the same in all cases by the third TiO_2 layer. In all the H adsorptions inspected for the (√2×√2) surface, there is free charge located in the Ti conduction band, which corresponds to the development of rumpling to screen the charge, as is seen in all cases in Figure 3.22. In all cases, the rumpling is massively enhanced near the surface, and the system remains rumpled until the very center of the slab.

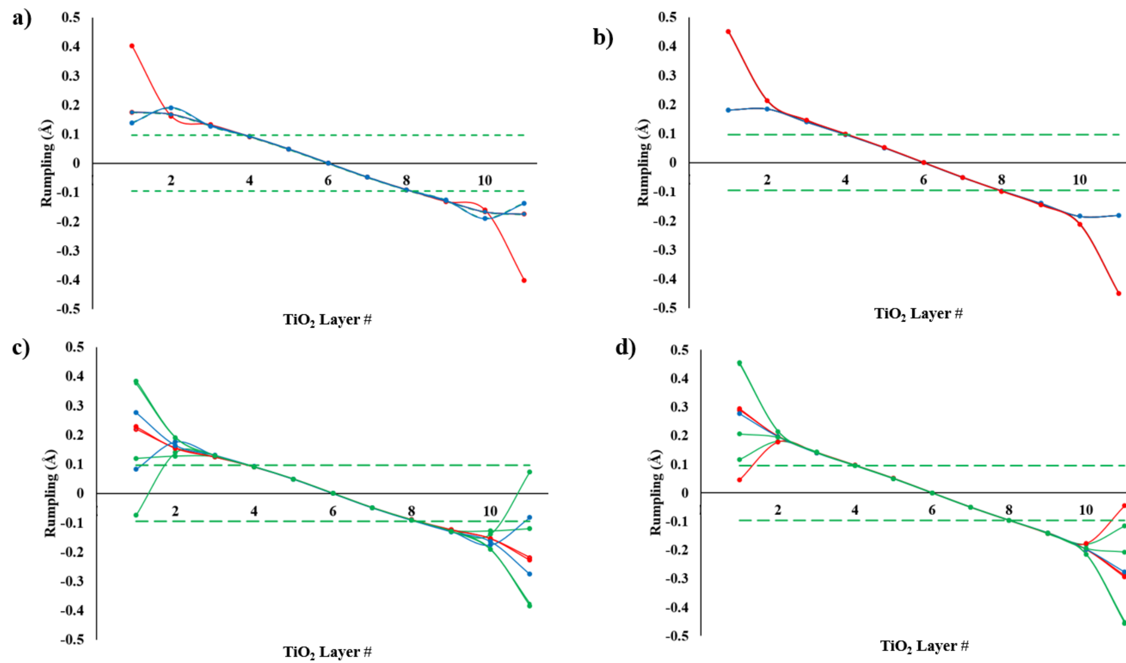

Figure 3.22. The rumpling of the ($\sqrt{2}\times\sqrt{2}$) TiO_2 layers for a) the 1H adsorbed surface, b) the 2H adsorbed surface, c) the 3H adsorbed surface and d) the 4H adsorbed surface. The green dotted line is the rumpling of bulk BTO. The red line indicates rumpling between a pair of Ti and O where both have adsorbed H, the green line indicates rumpling between a pair of Ti and H where one of the atoms has an adsorbed H, and blue indicates rumpling between a pair of Ti and H with no adsorbed H.

3.2.4. Conclusion

We studied the effect of H adsorption on both the (1×1) and ($\sqrt{2}\times\sqrt{2}$) TiO_2-terminated (001)BTO surfaces. For the (1×1) surface, 1H and 3H adsorption led to a metallic surface, whereas no adsorption and 2H adsorption led to an insulating surface, in agreement with prior DFT calculations of the STO(001) surface. With the 3H adsorbed case, we calculate the weakening of the Ti-H bond due to excess adsorption of charge donated by the OH complexes. For the ($\sqrt{2}\times\sqrt{2}$) surface, we see that the system remains metallic up to 4H adsorption, due to the imbalance of TiH and OH complexes. We see that in all cases, the insulating systems do not support a rumpling or polarization in BTO, whereas all metallic systems to support a polarization in BTO. The cause of this polarization is due to the system reducing the electric field caused by adsorbed bare H atoms, which does not occur for the insulating systems.

Chapter 4: Thin Pt Films on $BaTiO_3$[†]

Using density functional theory, we analyze the wetting conditions for Pt on the (001) surface of ferroelectric $BaTiO_3$ (BTO). We estimate the surface energy of (100), (110) and (111)Pt to be 2.42, 2.49 and 2.00 J/m^2, respectively. We find the BTO surface energy to vary between 0.26 and 2.28 J/m^2 depending on termination, polarization, and chemical environment. The interface energy between TiO_2-terminated out-of-plane polarized BTO and (100)Pt is found to be between 1.64 and 2.62 J/m^2, indicating that (100)Pt cannot wet BTO for this interface. A similar result is found for an interface with (110)Pt. Cross-sectional transmission electron microscopy of Pt films grown on BTO by molecular beam epitaxy with a low flux at high deposition temperature shows Volmer-Weber islands, consistent with first principles calculations.

4.1 Introduction

Properties of thin metal films grown on transition metal oxide substrates are important in a variety of technological applications, such as catalysis, electrical contacts, and capping layers.[170] While in the case of contacts and capping layers where a smooth continuous film, preferably epitaxial, is needed, in the case of catalysis, the use of nano-crystalline islands on the oxide support is beneficial to obtaining larger surface to volume ratios. Metal-oxide interfaces have also been the subject of many fundamental studies concerning their structure and electronic properties.[171–173] The growth of epitaxial interfaces is determined by a variety of factors; however, for growth near equilibrium, the lattice mismatch and the relative surface and interface energies dictate what the global nature of the interface would be.[174,175]

$BaTiO_3$ (BTO) is a ferroelectric oxide that can be grown on Si and Ge substrates with the use of an appropriate buffer.[175–177] The interest in putting BTO on semiconductors stems from the potential for realizing a ferroelectric field effect transistor, which is

---

[†] The work described in this chapter has been published as "Wetting at the $BaTiO_3$/Pt interface", K.D. Fredrickson, A.B. Posadas, A.A. Demkov, C. Dubourdieu and J. Bruley, J. Appl. Phys. **113**, 184102 (2013). K.D.F. designed and performed the first principles calculations. A.B.P. grew the samples. C.D. and J.B. performed the TEM. A.A.D. contributed to the theoretical calculations and the overall design of the work.

advantageous over regular transistors; the state of the transistor is nonvolatile and does not require any standby power.[178,179] However, one of the key requirements for achieving this is that the ferroelectric must be single crystalline with a single domain over the entire size of the device. Typical deposition techniques that can achieve single crystalline BTO are normally done at temperatures above 600°C, which is higher than the ferroelectric transition temperature of the material. This means that the BTO is grown in a paraelectric state and becomes ferroelectric during the cool down process. Achieving a single domain state requires that the lattice and thermal expansion matching be favorable, and that the film is electrically screened. The screening aspect can be achieved by using a metal overlayer on top of the ferroelectric during the cool down step after growth. When deposited at temperature higher than the ferroelectric transition temperature (105° C in BTO),[180] a metallic film can induce formation of a single domain as BTO undergoes the phase transition upon cooling. The formation of a metallic overlay on BTO at high temperature is the subject of our study.

The rest of the paper is organized as follows. We briefly describe the computational methods used in this work in Section 4.2. In Section 4.3, we discuss the theoretical calculations of the surface energy of BTO with both BaO and TiO_2 terminations, and with ferroelectric polarization both in-plane and out-of-plane. We also examine the interfacial energy of TiO_2-terminated out-of-plane polarized $BaTiO_3$ and Pt. In Section 4.4, we discuss the experimental results for the high temperature growth of Pt on a BTO substrate, particularly characterization using high resolution transmission electron microscopy. In Section 4.5, we discuss wetting and compare theoretical predictions with experimental results.

4.2 Computational Details

All calculations are done using density functional theory with the local density approximation and plane augmented-wave pseudopotentials as included in the VASP code.[65,66,131–134] We employ the Perdew-Zunger form of the exchange-correlation potential.[135] We use the valence configuration $3p^6 4s^2 3d^2$ for Ti, $5s^2 5p^6 6s^2$ for Ba, $2s^2 2p^4$ for O, and $6s^1 5d^9$ for Pt. We use a 600 eV kinetic energy cutoff. For the Brillouin zone

integration, we use the following Monkhorst-Pack[136] k-point meshes: 8×8×8 for bulk BTO, 17×17×17 for bulk Pt, 8×8×2 for the BTO/(100) Pt structures and BTO slabs, 8×4×1 for the BTO/(110) Pt structure, 17×17×1 for the (100) Pt slab, 17x24x1 for the (110) Pt slab, and 24×24×1 for the (111) Pt slab. To remain consistent, we also calculate surface energies for 8×8×2 (100) Pt, 8×11×2 (110) Pt, and 12×12×2 (111) Pt so that we can compare surface energies with the same approximate k-point mesh to those of the interfaces for our wetting calculations. Bulk BTO and Pt are fully optimized, and all structures are optimized with respect to the ionic positions until the forces on all atoms are less than 10 meV/Å; for the (110) Pt-BTO interface we optimize until the forces are less than 60 meV/Å. The energy is converged to 10^{-3} meV/cell. The relaxation is not constrained by symmetry.

At high temperature BTO is cubic, but at 105°C it transforms to a tetragonal ferroelectric phase. As we are interested in the room temperature properties of BTO, we restrict ourselves to studying the tetragonal phase. Our calculated lattice constant *a* of 3.96 Å and c/a ratio of 1.005 compare favorably with the experimental values of a = 3.99 Å and c/a = 1.011,[166] and with previously reported theoretical values of a = 4.00 Å and c/a = 1.010.[167]

To calculate the surface energy of BTO, we use a 5.5 unit cell (UC) thick (1×1) BTO slab augmented by 15 Å of vacuum. The slab is terminated symmetrically with either a BaO or TiO_2 surface, and with the polarization either in-plane or out-of-plane. We allow the structure to relax completely. To calculate the surface energy of Pt, we consider 37 Å thick (100)-oriented Pt slab terminated symmetrically and allowing full relaxation. We also consider (111) and (110) oriented slabs that are 20 and 25 Å thick, respectively.

For the interface calculations we use BTO slabs with thickness of 5, 10, 15, 20, and 25 UCs. We only consider the TiO_2 termination because of the well-documented chemical stability of this surface.[103,104] The oxide is capped on both sides with five monolayers (ML) of Pt (9.8 Å), followed by 7.5 Å of vacuum, for a total of 15 Å of vacuum as shown in Figure 4.1. The electrostatic potential must be equal on both sides of the cell, and the vacuum region allows us to mitigate the residual field resulting from incomplete screening. To make sure that the vacuum for our calculation is thick enough, we examine the plane-

averaged potential of our BTO/Pt structures and verify that the potential of the system reaches a constant value in the vacuum region. We initially polarize BTO in one direction with the same rumpling (defined as the difference in position of Ti and O atoms along the cell) as in the bulk and then allow the structure to relax. Metal electrodes screen the charge and stabilize the ferroelectric behavior of BTO. Pt is fcc at room temperature, with an experimental lattice constant of 3.920 Å. We calculate the lattice constant as 3.906 Å, in good agreement with experiment. (100)-oriented Pt is reasonably well lattice matched to BTO resulting in only 1.4% tensile strain in the metal layer.

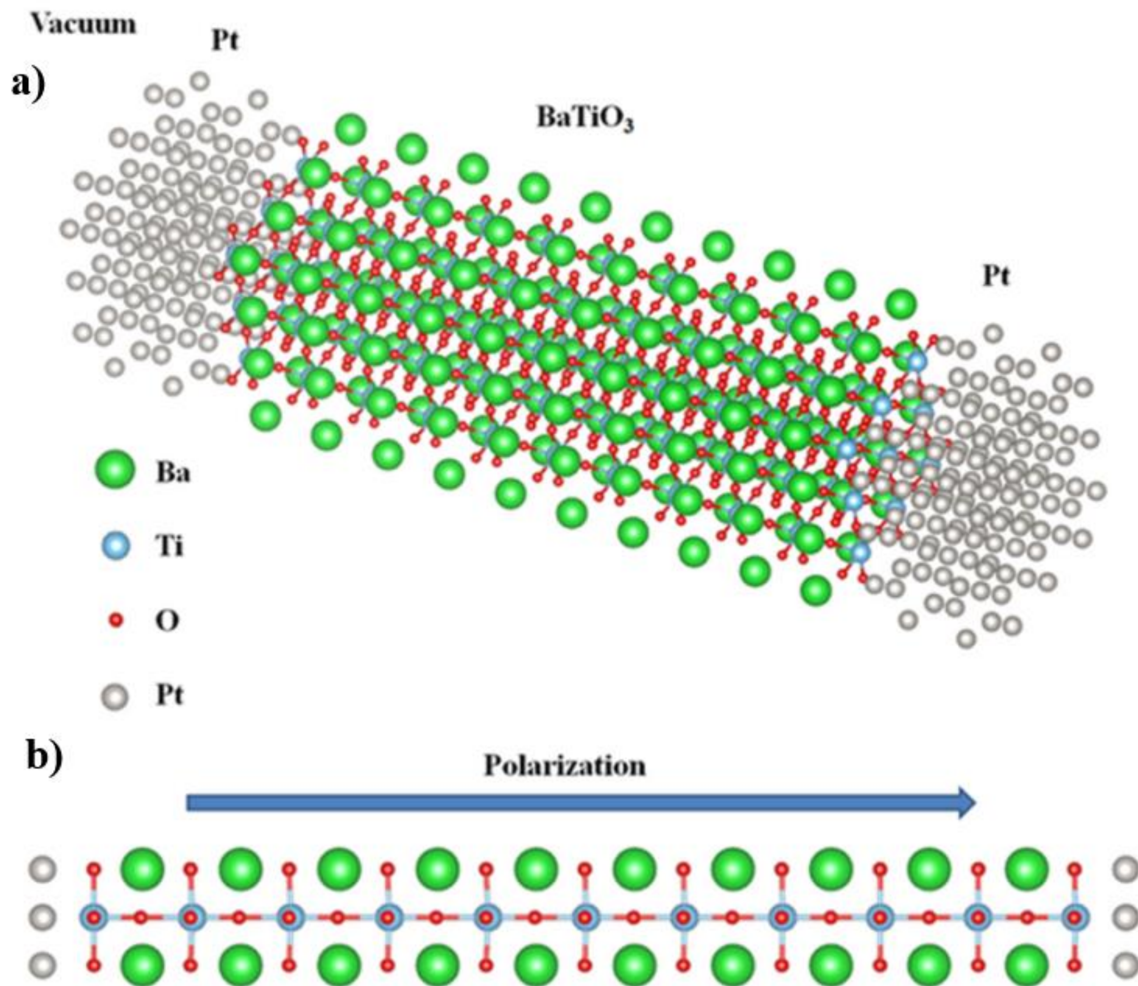

Figure 4.1. a) The simulation cell containing the BTO/(100)Pt slab. The slab shown contains ten UCs of BTO. b) Zoomed-in portion that shows polarization of BTO.

4.3 Theoretical Results

First, we examine the polarization of the heterostructures as a function of Pt thickness. Upon relaxation, the polarization stays perpendicular to the interface, and no rumpling parallel to the interface develops. The rumpling of the BTO is given in Figure 4.2. We see that 5.5 UC of BTO (~2.2 nm) is too thin to stabilize a ferroelectric polarization; this is in agreement with prior reports that the critical thickness in LDA is ~2.4 nm.[36] Films of 10.5, 15.5 and 20.5 UC show a monophase ferroelectric polarization. Although the rumpling in BTO is nonuniform, the thicker BTO is, the closer the rumpling approaches the bulk value. There are two other curious features that we point out: First, although the polarization drops rapidly near the right end of the slab, it jumps up again at the BTO/Pt interface. This is due to Pt-Ti bonding, and the tendency of O and Pt to resist bonding. Density of states calculations show that this layer is metallic, and therefore we do not expect this layer to resemble very much a TiO_2 layer in bulk BTO. Secondly, on the left side of the slab, we can see that this TiO_2 layer is unrumpled; this is probably due to the two competing factors of Pt-Ti bonding and nearby polarization (the polarization from nearby TiO_2 layers encourages neighboring TiO_2 layers to polarize in the same direction).

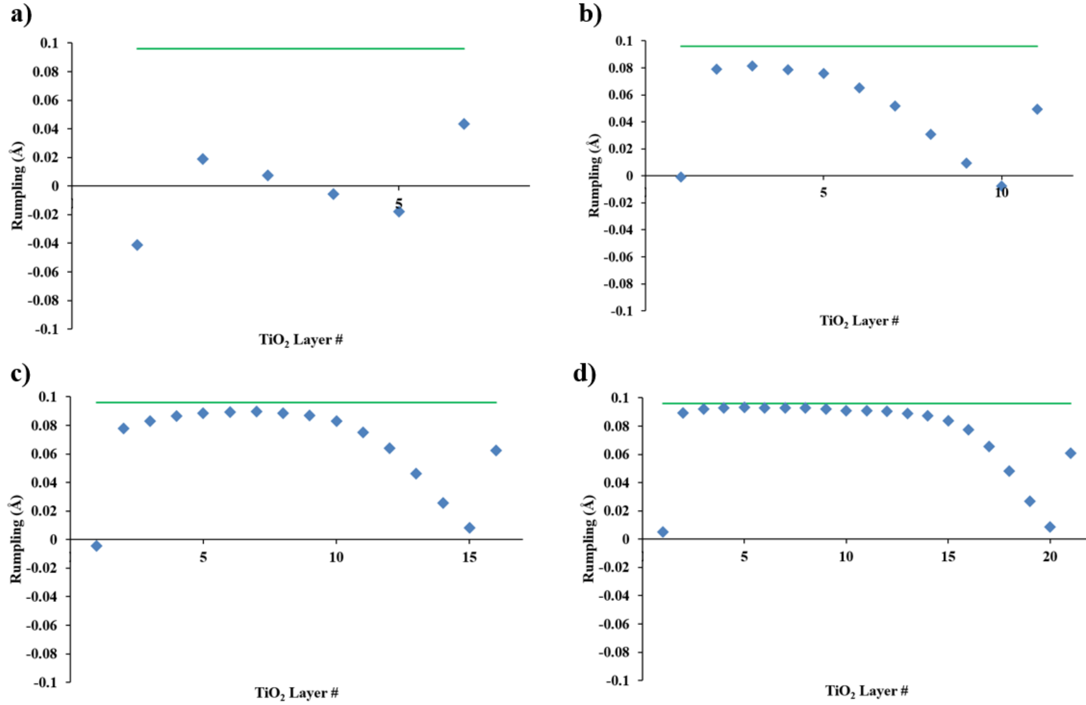

Figure 4.2. The rumpling for each TiO_2 plane for the BTO/Pt structures with a) 5.5 UC b) 10.5 UC c) 15.5 UC and d) 20.5 UC of BTO. The green line is rumpling for bulk BTO.

The thermodynamic wetting criteria is

$$\gamma_{substrate} > \gamma_{\mathrm{interface}} + \gamma_{film} \tag{4.1}$$

where γ is the surface or interface energy. In our calculations, BTO is the substrate and Pt is the film, and all quantities in equation one can be readily calculated. First, we fully relax a Pt slab and estimate its surface energy as

$$\gamma_{Pt} = \frac{1}{2A}(E_{Pt-Slab} - N_{Pt}E_{Pt}) \tag{4.2}$$

where N_{Pt} is the number of Pt atoms in the slab and E_{Pt} is the energy per atom in bulk Pt. N_{Pt} is 38 in our calculation, corresponding to a film with a thickness of 37 Å, and A is the surface area of the slab. The result is in good agreement with reported experiment and previous LDA and generalized-gradient approximation (GGA) calculations.[97,181–183] For completeness we also consider Pt slabs with the (110) and (111) orientations. In Table 4.1,

we compare our result with those in the literature. It is clear that (111) is the lowest energy orientation of Pt. The main reason for the discrepancy with the earlier work is the use of a much thicker slab and allowing for full relaxation in our study.[181] In comparison to Reference [182], we see that the experimental value of the surface energy is calculated from the surface tension of liquid Pt, converted to surface energy at the melting point, and then extrapolated down to 0 K from entropy terms. The authors acknowledged that the method to determine the vibrational entropy of the surface is crude and is taken as a constant for surfaces of all metals. The configurational entropy of the surface is likewise estimated to remain constant over all materials, so the direct measurement of the surface energy is very difficult. Taking this into account, the agreement of our 0 K theoretical calculations of the surface energy with experiment is reasonable.

Surface	This work DFT-LDA	Theory [a] DFT-LDA	Theory [b], DFT-GGA	Experiment
(100)	2.420	2.454	2.734	
(111)	2.002	2.013	2.299	2.489 [c], 2.475 [d]
(110)	2.485	2.502	2.819	

[a]Reference [97]

[b]Reference [181]

[c]Reference [182]

[d]Reference [183]

Table 4.1. Surface energies of Pt (J/m^2).

To calculate the surface energy of BTO and the Pt/BTO interface energy, we use a first-principles thermodynamic technique involving chemical potentials.[184] Following Ref. [184], we reference the chemical potentials of BaO, TiO_2, and Pt to the rock salt, rutile, and fcc bulk phases, respectively. The equilibrium condition of the surface with the bulk is given by:

$$E_{BTO} - E_{TiO_2} - E_{BaO} = -E_f = \mu_{TiO_2} + \mu_{BaO} \quad (4.3)$$

where E_{BTO}, E_{TiO_2}, and E_{BaO} are the bulk energies of BTO, rutile TiO_2 and BaO respectively, measured relative to isolated iron cores and electrons. E_f is the energy of formation of BTO, and μ_{TiO_2} and μ_{BaO} are the chemical potentials of TiO_2 and BaO respectively. We calculate the bulk formation energy of tetragonal BTO to be 1.69 eV. We note that either chemical potential can be expressed in terms of the other and the formation energy and choose to eliminate μ_{BaO} and work with μ_{TiO_2}.

We calculate the surface free energy for BaO- and TiO_2-terminated BTO slabs, with BTO polarized both in-plane and out-of-plane, using:

$$\gamma_{BTO} = \frac{1}{2A}(E_{BTO-Slab} - N_{BaO}(E_{BaO} - \mu_{TiO_2} - E_f) - N_{TiO_2}(\mu_{TiO_2} + E_{TiO_2})) \tag{4.4}$$

There is, however, an extra complication. Owing to the periodic boundary conditions, the relaxed slabs have a mirror plane in the center. And without metal contacts that can screen, relaxation creates slabs that are polarized either inwards (for the TiO_2-terminated surface), or outwards (for the BaO-terminated surface) with respect to vacuum as shown in Figure 4.3. This essentially leads to a 180° "head-to-head" (or "tail-to-tail") domain wall (DW) that needs to be accounted for. To estimate the DW energy, we take the relaxed TiO_2-terminated slab from our surface calculation and remove vacuum (in doing so we also remove one of the TiO_2 planes in order to have the stoichiometric structure). We depolarize the edge of the unit cell so that the structure contains two (nonequivalent) DWs. Then, we calculate the energy of the structure, subtract the bulk energy, and divide by two to obtain an average DW energy of 0.089 J/m^2. We repeat the same procedure for the BaO terminated slab, and find a DW energy of 0.132 J/m^2. Taking the average of two numbers we find an average DW energy of 0.110 J/m^2. We would like to point out that this type of a DW is an artifact of our calculations. The 180° DWs typically considered in the literature separate regions of parallel but opposite polarizations, with the domains of polarization side-to-side instead of head-to-head.[185–188] The energy of a "parallel" DW is significantly lower than that of the "head to head" DW described here, and is of the order of 0.005 J/m^2.

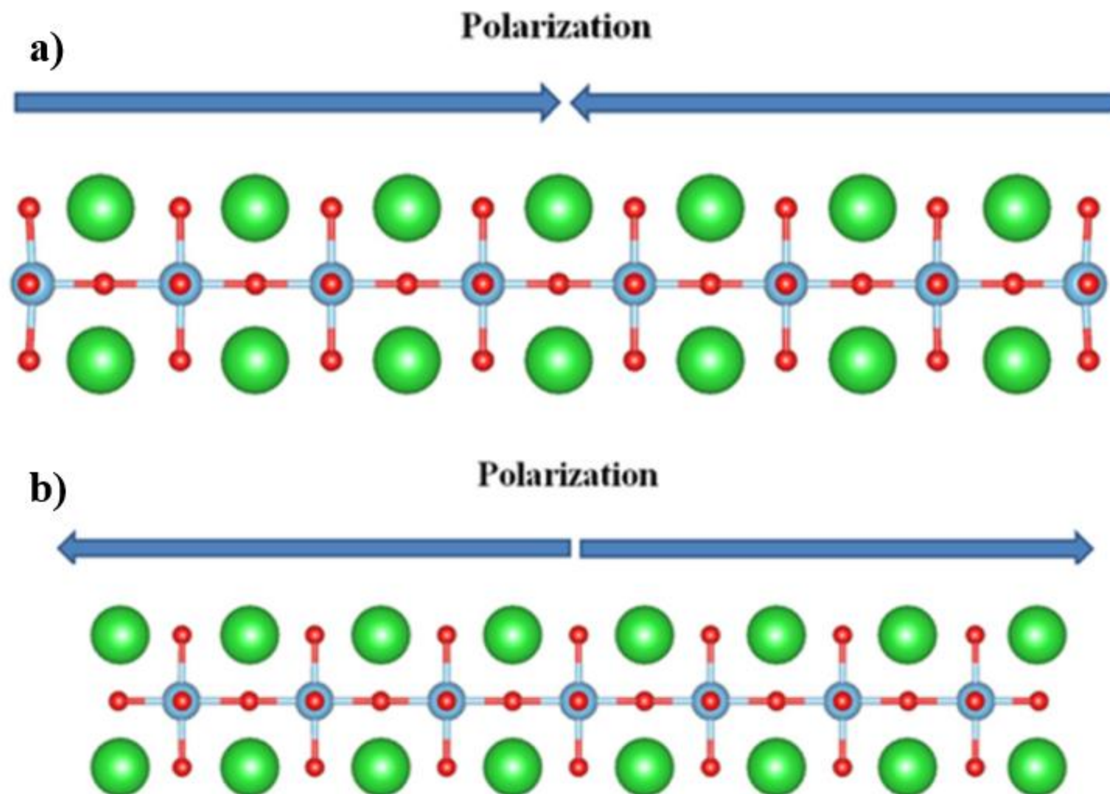

Figure 4.3. Polarized slabs of a) TiO_2 terminated and b) BaO terminated BTO.

We correct for the head-to-head DW and plot the BTO surface energy in Figure 4.4. We see that the energy of the BaO-terminated surface is always lower than that of the TiO_2-terminated one, regardless of polarization. Also, the surface energy of the out-of-plane polarized slab is always lower than that of the in-plane polarized slab. The latter effect can be traced to the surface relaxation. For example, when the TiO_2 terminated surface is created, Ti atoms sink inwards thus creating a polarization pattern consistent with the out-of-plane polarization. It is worth noting, that our calculations do not include the actual domain structure of the film found in experiment, and are therefore applicable only qualitatively.

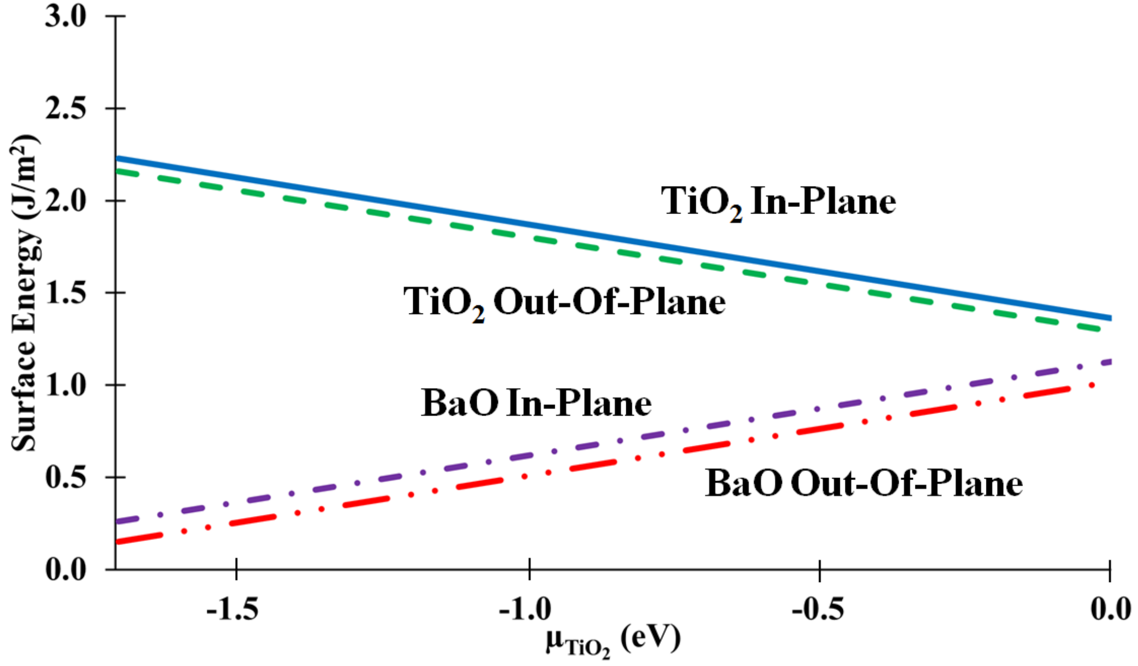

Figure 4.4. Surface energy of BaO and TiO_2-terminated BTO slabs.

We can also use the first-principles thermodynamic technique in a slightly different way, not assuming that the metals are already oxidized.[189] We calculate the Gibbs free energy Ω as

$$\Omega = \frac{1}{2A}(E_{Slab} - N_{Ba}(\mu_{Ba} + E_{Ba}) - N_{Ti}(\mu_{Ti} + E_{Ti}) - N_O(\mu_O + E_O)) \tag{4.5}$$

where we now calculate the free energy with respect to bulk Ba, bulk Ti, and the O_2 molecule. We also assume the following restrictions:

$$\mu_{Ba} + \mu_{Ti} + 3\mu_O = E_{BTO} - E_{Ba} - E_{Ti} - 3E_O = E_f^{BTO} \tag{4.6}$$

$$\mu_{Ba} \le 0, \; \mu_{Ti} \le 0 \tag{4.7}$$

$$\mu_{Ba} + \mu_O \le E_f^{BaO}, \; \mu_{Ti} + 2\mu_O \le E_f^{TiO_2} \tag{4.8}$$

Equation 4.6 ensures that the BTO surface is in equilibrium with the BTO bulk. Equations 4.7 ensure that no Ba or Ti will form on the surface. Equations 4.8 ensure that BaO and TiO_2 will not form on the surface.

Arbitrarily eliminating μ_{Ti} leads to a diagram shown in Figure 4.5, wherein we plot the comparison of the surface energies against μ_{Ba} and μ_{O}. We indicate, in the shape bordered by our given restrictions, which termination leads to a lower surface energy. We discover that the surface energy of the BaO-terminated surface is always the lowest within the restrictions given by Equations 4.6-4.8. This agrees with our more elementary treatment, which also shows that the BaO-terminated surface is always the lowest energy regardless of μ_{Ba}.

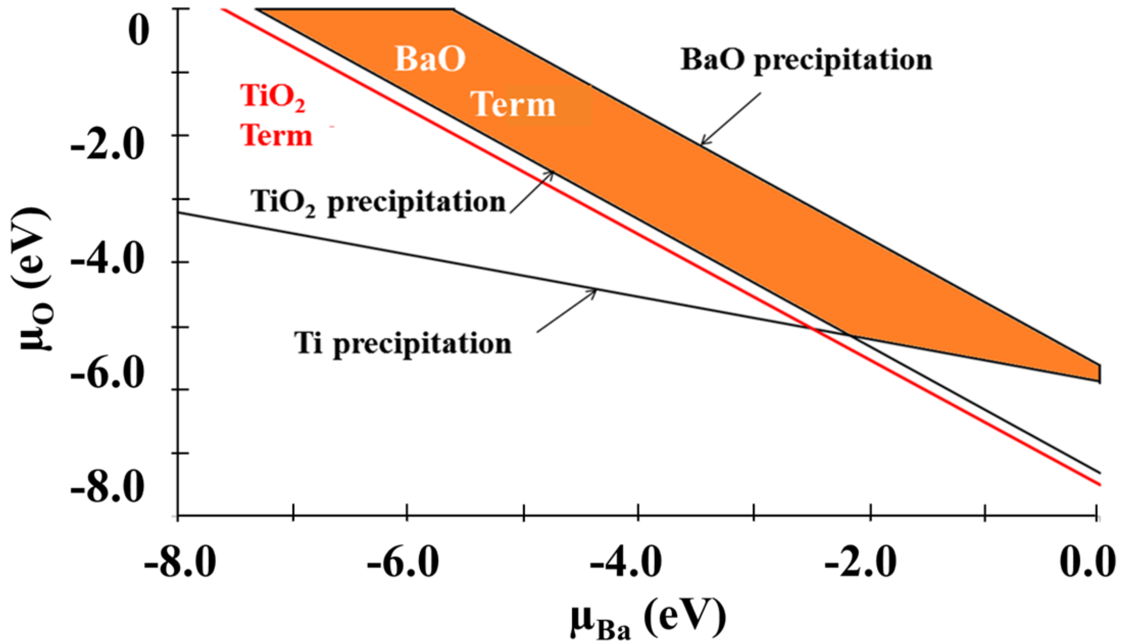

Figure 4.5. Surface energies of out-of-plane polarized BaO- and TiO_2-terminated BTO slabs. Below the red line, the surface energy of the TiO_2-terminated slab is the lowest, but as this this never occurs within the restrictions, the surface energy of the BaO-terminated slab is always the lowest.

Using equation 3, we calculate the interfacial free energy F as

$$F = \frac{1}{2A}(E_{BTO-Pt} - N_{BaO}(E_{BaO} - \mu_{TiO_2} - E_f) - N_{TiO_2}(\mu_{TiO_2} + E_{TiO_2}) - N_{Pt}E_{Pt} - 2E_{Pt-Surface}) \tag{4.9}$$

where this equation is for the Pt/BTO interface. The interface energies for the range of thicknesses, and the surface energy of Pt(100) are plotted against μ_{BaO} in Figure 4.5 a). As

the (100) Pt surface energy is greater than that of BTO for every thermodynamically allowed value of μ_{TiO2}, we conclude that (100)-terminated Pt will not wet BTO but will grow as three dimensional islands according to the Volmer-Weber growth mode.

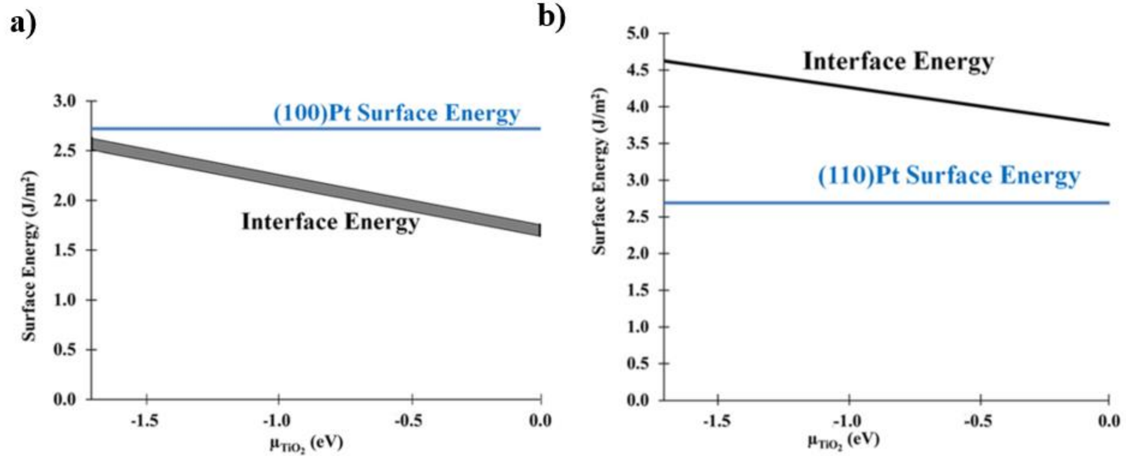

Figure 4.6. Surface energy of Pt and energy of the Pt/BTO interface as a function of the chemical potential for the a) (100) and b) (110) interface. The shaded area in a) indicates the variation of the interface energy with the thickness of the BTO slab.

The (100) Pt surface is, of course, not the only possible Pt termination for an interface with BTO. Examining the transmission electron microscopy (TEM) images of the experimentally grown BTO/Pt interface, we surmise that the observed interface is a (110)Pt/BTO structure, principally due to the arrangement of Pt in zig-zag chains. The TEM image of such an interface is shown in Figure 4.7 a), and comparison to the calculated interface is shown in Figure 4.7 b). Following the same procedure for the (100)-terminated Pt interface, we calculate the (110)-interfacial Pt/BTO energy and plot it in Figure 4.6 b). As the interfacial energy is greater than the Pt surface energy at every value of μ_{TiO2}, we see that Pt will not wet this interface either, and we expect that Pt will also grow as three dimensional islands.

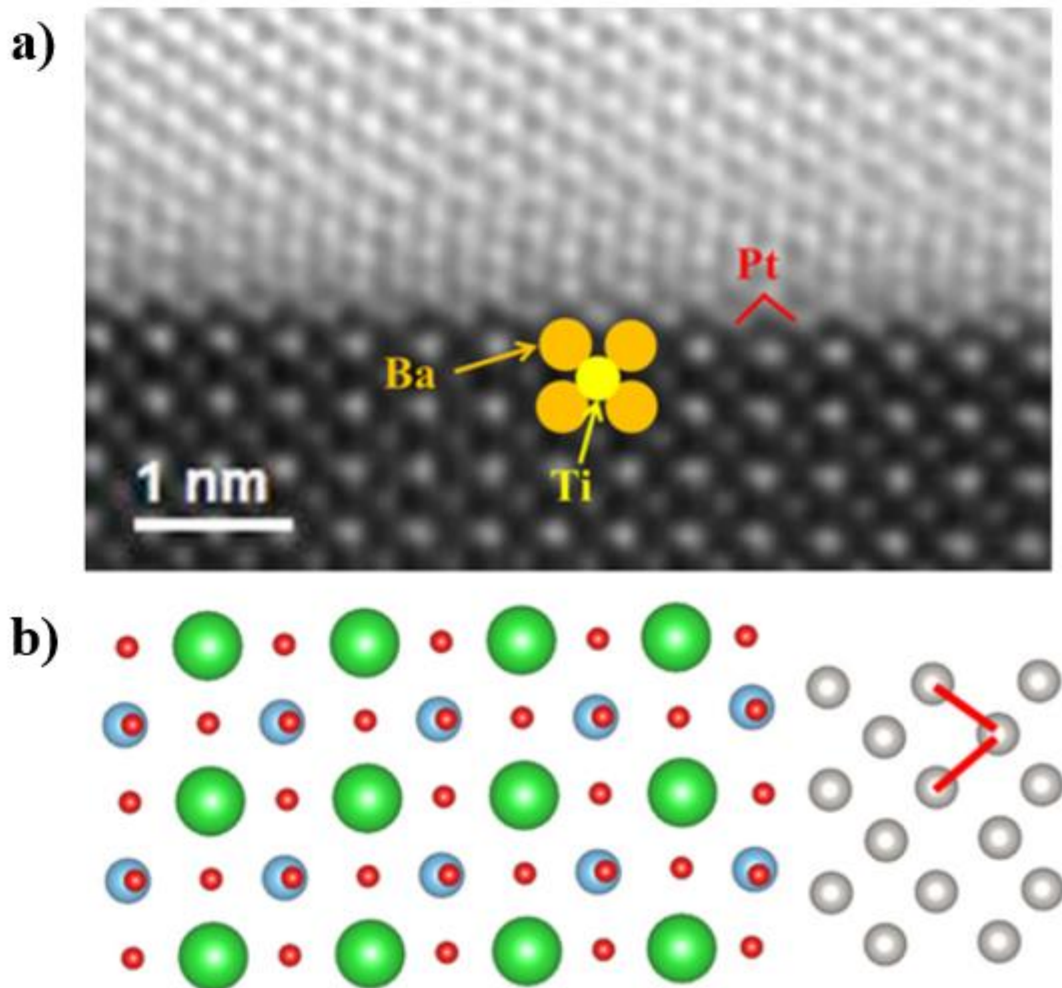

Figure 4.7. a) The TEM image of the Pt/BTO interface. The zig-zag chains of Pt are identified in red. b) The model used to calculate properties of this interface, with the zig-zag Pt identified in red. The model is rotated 90º with respect to the TEM image.

The rumpling for the BTO/(110)Pt are slightly more complicated than those for the BTOPt(100) case, because there are three directions of rumpling to consider, rather than two, because the directions parallel to the interface are no longer equivalent (Figure 4.8). We plot the rumpling of the (110)Pt/BTO/(110)Pt structure in the a, b and c directions in

Figure 4.9. We see that there is significant rumpling in the a direction, although it is half the bulk value of BTO. In the b direction, although there is significant rumpling at the interface, the rumpling becomes essentially 0 at the center of the BTO. The c direction is more complicated, as there are three inequivalent rumplings between the Ti and three inequivalent O; we plot the average in Figure 4.9 c). Although these vary wildly at the interface, in the center of the slab they are all the same, and the rumpling looks very similar to that of the (100)Pt/BTO/(100)Pt structure.

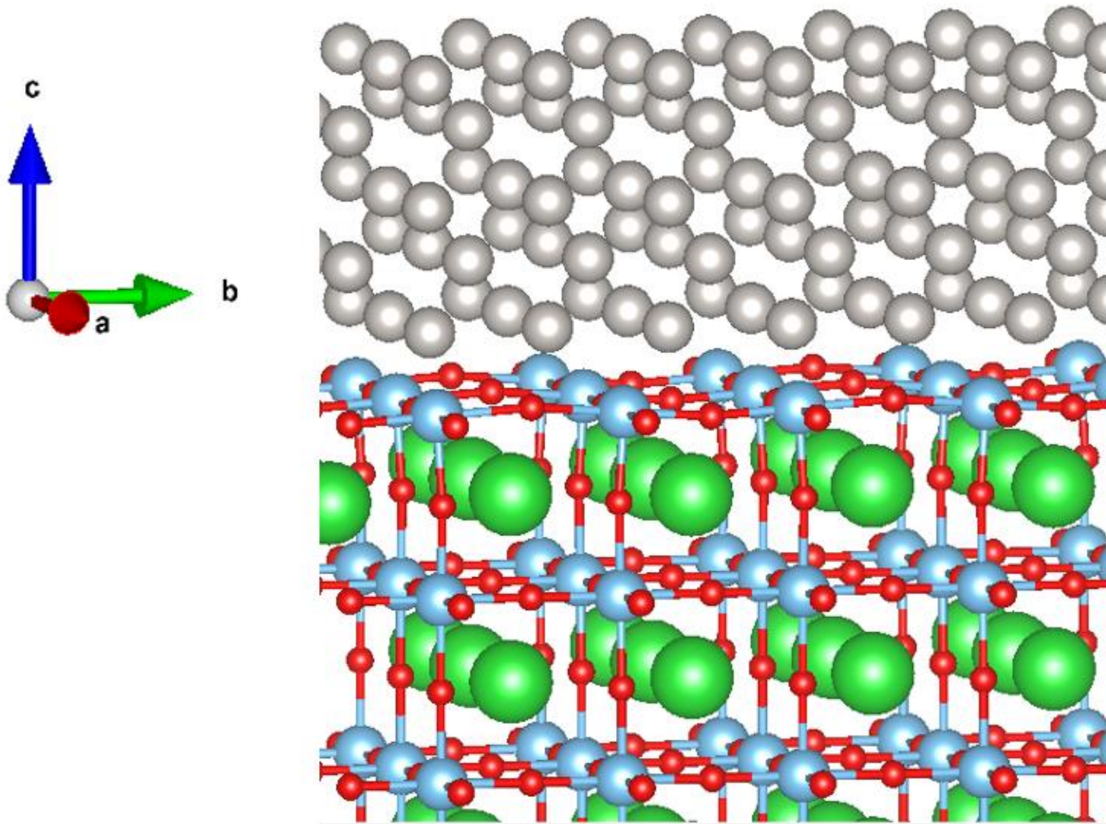

Figure 4.8. The BTO/(110)Pt interface, showing the three directions of rumpling.

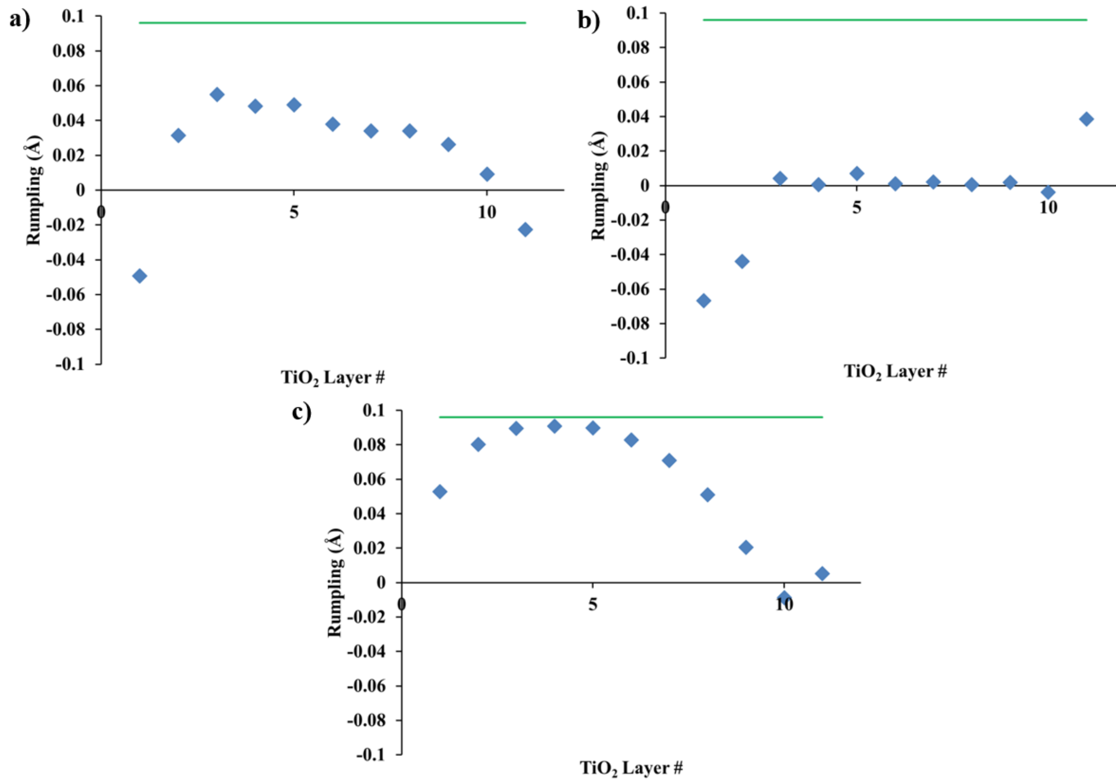

Figure 4.9. Rumpling of the (110)Pt/BTO/(110)Pt structure in the a) a, b) b and c) c directions.

4.4 Experimental Results

In order to experimentally realize these Pt/BTO heterostructures, epitaxial BTO thin films were first grown on $SrTiO_3$ (STO)/Si substrates with a fully relaxed $SrTiO_3$ layer using molecular beam epitaxy (MBE). The substrates used were p-type epi-grade Si(100) diced into 20 mm × 20 mm squares that have been degreased (acetone, isopropanol, and water for 5 min each with sonication) and exposed to ultraviolet/ozone for 15 min prior to loading into the growth chamber. Prior to growth, the substrates are outgassed for 10 min at 650°C then the native SiO_2 layer is removed using Sr-assisted deoxidation which involves depositing two monolayers of Sr metal at 650°C then heating to 800°C until a clear 2×1 reconstruction of the Si(001) surface is observed.[190] The sample is then cooled to 575°C and additional Sr is deposited to form a ½ monolayer Sr Zintl interlayer.[191]

The STO layer is then grown at 500°C and 2×10^{-7} Torr of molecular oxygen by co-deposition of Sr and Ti[192] to a total thickness of 16 unit cells (6.4 nm), which is a thickness

at which STO on Si is already fully relaxed.[193] Further details of the STO deposition process on Si can be found in Ref. [194]. After the STO growth, the substrate is heated at 20°C/min to 700°C while simultaneously ramping the O_2 pressure to 5×10^{-6} Torr. When the target O_2 pressure and substrate temperature are reached, BTO growth by means of alternating monolayer dosing of Ba and Ti is initiated, with Ba first and Ti last, ensuring a TiO_2-terminated BTO surface. The entire growth process is monitored *in situ* by RHEED to ensure high crystallinity and stoichiometry. After 20 nm of BTO is grown, the sample is cooled at 5°C/min in O_2 to 500°C. Pt metal is then deposited on BTO at 500°C in vacuum from an electron beam evaporation source operated at 7.75 kV and 200 mA emission resulting in a flux of $1\text{x}10^{13}$ atoms/cm^2-s. The equivalent of 10 nm of Pt is deposited on the heated TiO_2-terminated BTO surface. The low flux and relatively high temperature of Pt deposition is designed to approximate growth close to equilibrium to facilitate the theoretical interpretation of the suitability of Pt as a screening metal layer. After Pt deposition, the sample is cooled at 5°C/min to room temperature in vacuum.

The sample is characterized by cross-section TEM to determine the degree of wetting between Pt and BTO and to ascertain the interface structure to be used in the calculation of the interface energy. A thin lamella suitable for TEM was cut from the sample using a focused ion beam. Figure 4.10 shows a low-magnification cross-section TEM image of the Pt/BTO/STO/Si structure. The figure shows that the Pt is discontinuous and forms faceted islands. Figure 4.11 shows a higher magnification TEM image showing the different layers more clearly. The figure also shows that a thin (~3 nm) SiO_2 interlayer has formed between the Si and STO as a result of the BTO deposition at high temperature and high oxygen partial pressure. We can see from the images that Pt islands consist of three basic shapes when they grow on the BTO surface: these include cubes (Figure 4.12 a)), diamonds (Figure 4.12 b)) and islands that have multiple irregular facets (Figure 4.12 c)). Although the detailed shapes vary, they all appear to be roughly the same size, on the order of 20 nm in width and height. High resolution imaging confirms that Pt is epitaxial on BTO. Crystalline orientation relationship of the Pt to the underlying BTO substrate is assessed from the computed diffractogram of the lattice images from regions of the Pt. We

observed instances of either the (100) or (110) Pt planes lying parallel to the BTO (001) surface. The most common facets of the Pt are from the low index (111) and (110) families. In some cases it seems that the Pt is embedded in the BTO surface, destroying part of the BTO surface in order to sink into the slab. The composition of this layer is not measured in this study, but from the light contrast level it is likely to be of lower density with respect to the Pt and BTO.

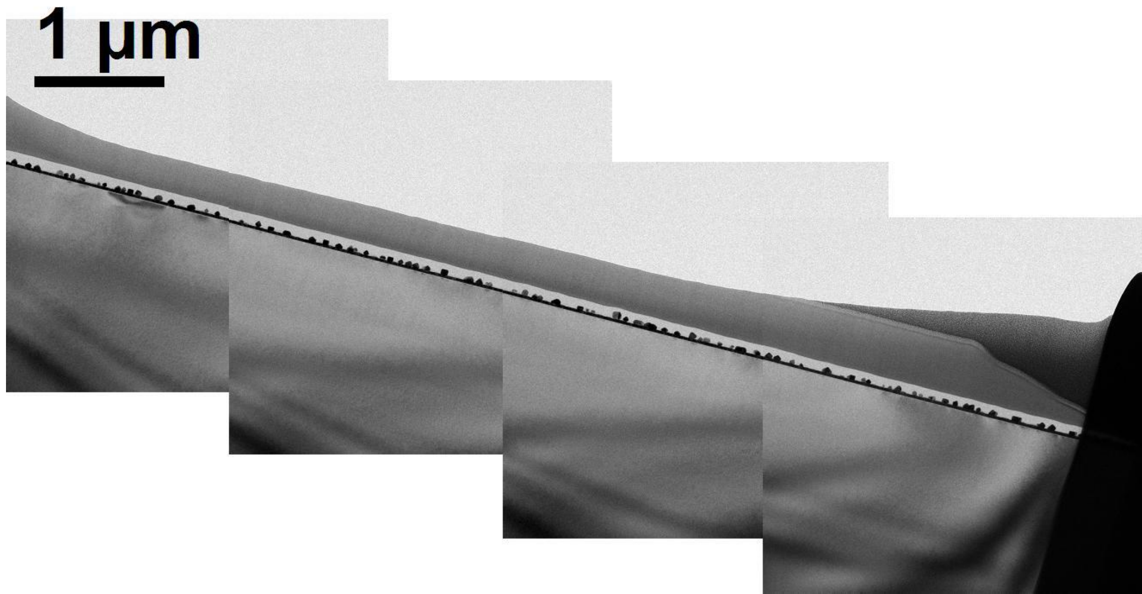

Figure 4.10. Low-magnification cross-section TEM image of the Pt/BTO/STO/Si structure.

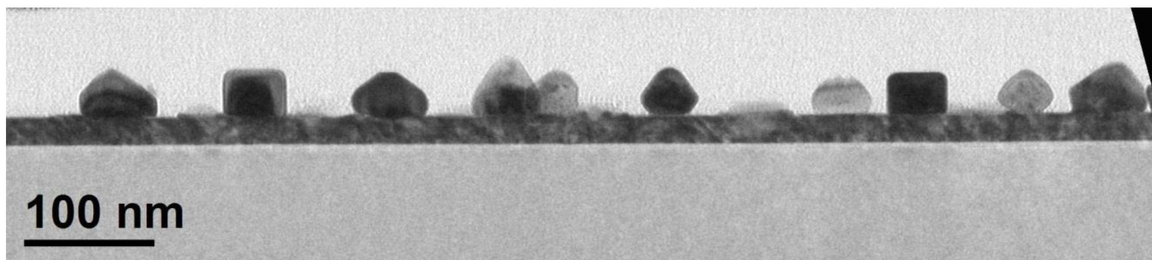

Figure 4.11. Higher magnification TEM image.

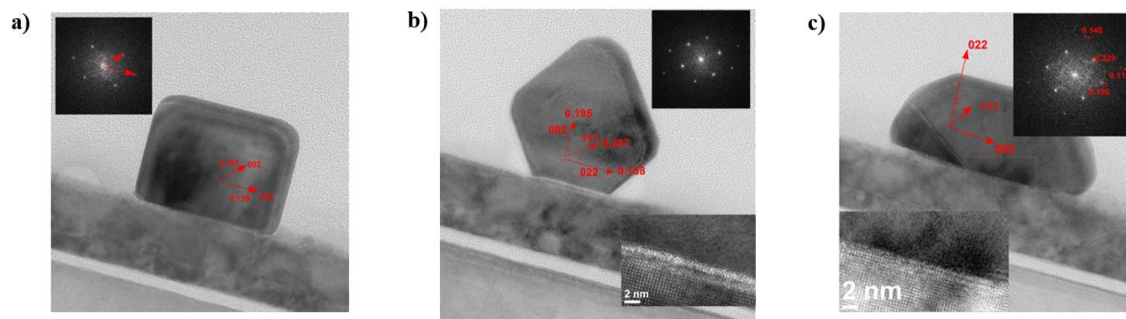

Figure 4.12. a) A cubic island. b) A diamond island. c) An irregular island.

Electron energy-loss spectrum-image data were recorded using dual-EELS Gatan Quantum spectrometer fitted to a FEI Titan STEM. For each map, two spectrum images were concurrently recorded along with the dark field STEM image. The first map was taken with a readout time of 10ms from low energy range from 200 up to 1200 eV and the second with a readout time of 40ms in the range from 1400 eV up to 2400 eV. In the low energy range, the edges of Ti-L at 456 eV, O-K at 532 eV, and Ba-M at 721eV were processed by fitting a standard power law background in an approximately 309eV wide region preceding the edge. The net counts were determined using approximately 30eV windows. In the high loss region, the net counts under the Si K at 1839 eV, Sr L at 1940 eV, and Pt M at 2122 eV were determined by using multiple least squares fitting algorithm built into the digital micrograph software. The characteristic edge shapes were extracted from the bulk regions of the sample and were fitted to the spectrum image data with a background removed by fitting a power-law in a 150eV wide window preceding the Si edge. Two maps are shown here. The first shown in Figure 4.13 was recorded at a pixel spacing of 0.26 nm with a 37 by 41 nm field of view. It shows the Pt recess with respect to the top of the BTO. The interface between the STO and BTO is seen to be sharp. In addition, there appears to be a small amount of Ba coverage on the outer Pt surface. The 2nd map shown in Figure 4.14 is an atomic column resolved elemental overlay showing the Pt/BTO interface. The pixel spacing in this map is 0.04 nm and the field of view is approximately 2.2 x 2 nm. Whilst atomic resolution is not visible in the Pt map, the red columns of Ba and green columns of Ti suggest that the interface is Ti rich. This is more readily seen in the line profiles (Figure

4.15) extracted from summing the intensities over a 0.4 nm wide region parallel to the interface.

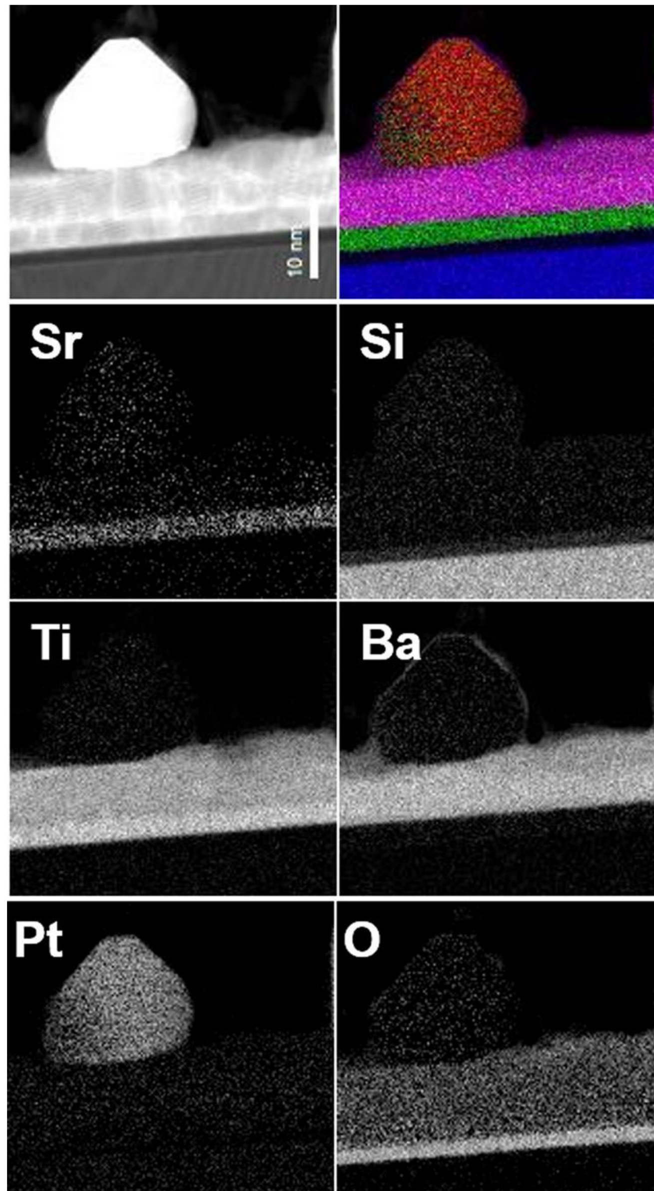

4.13. Elemental maps showing Sr, Si, Ti, Ba, Pt, and O distributions, extracted from area under ionization edge after fitting power law background. Top left image represents the high-angle annular dark-field image acquired during the acquisition of the spectrum-image and the top right image represent a color overlay of the Si (blue), Sr (green), Pt (red), and Ba (magenta) elements. Pixel separation 2.6 Å, map size 195 by 143 pixels. Probe size less than 2Å.

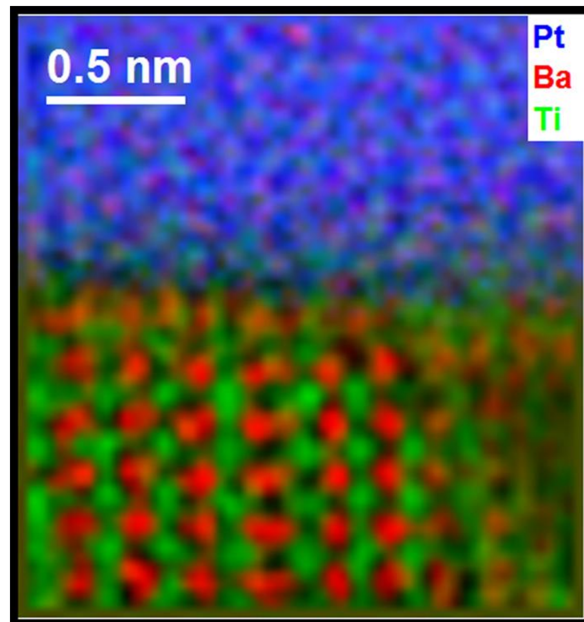

Figure 4.14. Atomic resolution elemental overlay of the Pt (blue), Ba (red), and Ti (green) showing the interface layers. Pixel separation 0.4 Å, map size 64 by 60 pixels.

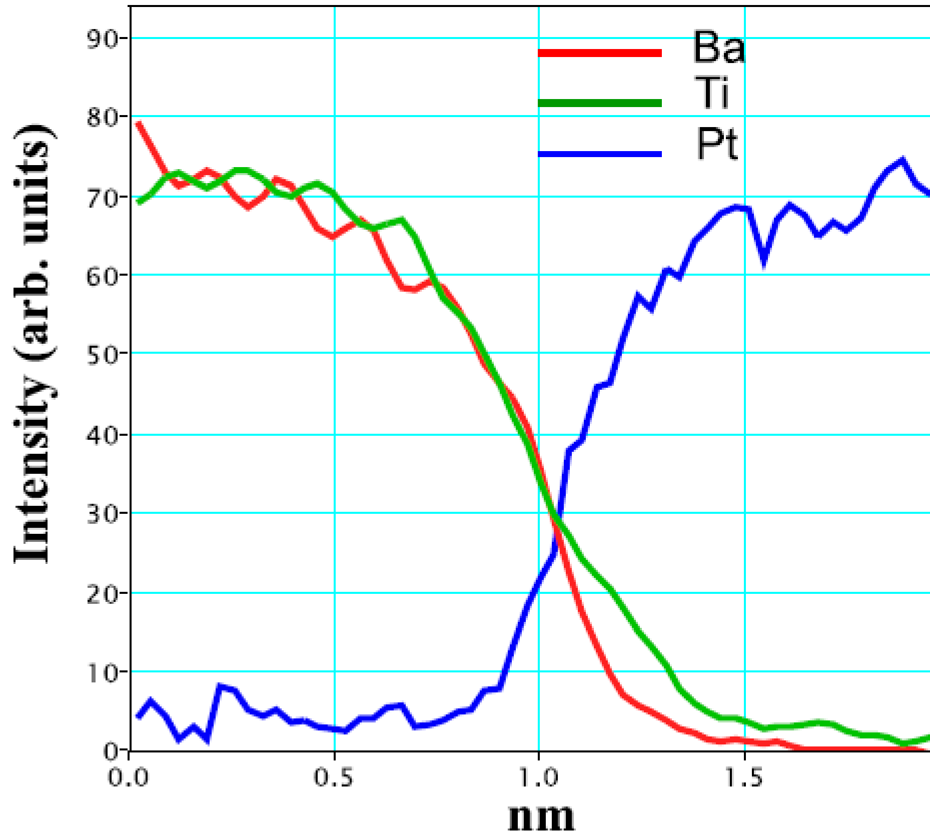

Figure 4.15. Lines of Pt, Ba, and Ti are extracted by summing the signal from a 0.4 nm wide box parallel to the interface along a trajectory perpendicular to the Pt/BTO interface.

Using the electron diffraction data we elucidate the direction of growth, and interface orientation of the islands, along with the crystallographic directions of the exposed surfaces. To gain further insight in the average size of the islands, we consider a simple model comparing a continuous Pt film on BTO with that broken into islands. The volume of Pt is assumed to be conserved, and therefore is not included in the model. We first consider a film of Pt covering the entire BTO sample with a surface area A_0 of 400 mm^2, and having a height h_0 of 10 nm, corresponding to the experimental values of the nominal substrate area and deposited thickness. The energy contributions of the film are the interfacial energy with BTO and the surface energies of the five free sides of the film:

$$E_{Film} = A_0(\gamma_{110-Interface} + \gamma_{Pt}) + 4\sqrt{A_0}h_0\gamma_{Pt} \quad (4.10)$$

where $\gamma_{110\text{-Interface}}$ is the interface energy of BTO/Pt, and γ_{Pt} is the surface energy of Pt (we average over the values of the (100) and (110) surface energies for simplicity). We assume that this film then separates into *N* equally sized islands (height differing from depth and width) with the same total volume as the original film (this is why no bulk volume energy contribution is considered in Equation 10). The energy of the islands is then estimated to be

$$E_{Islands} = x^2N(\gamma_{110-Interface} + \gamma_{Pt(110)}) + 2xhN(\gamma_{Pt(110)} + \gamma_{Pt(100)}) + (A_0 - x^2N)\gamma_{BTO} \quad (4.11)$$

where γ_{BTO} is the surface energy of BTO, *N* is the number of islands, *x* is the width and depth of the island, and *h* is its height. The first term is the interfacial and surface energies of Pt islands, the second term is the energy of the sides of the islands, and the third term is the energy contribution due to the exposed surface of BTO. The volume conservation constraint is given by

$$Nx^2h = A_0h_0 \quad (4.12)$$

Setting equations 10 and 11 equal to each other, we have two equations and three unknowns (*N*, *x* and *h*). However, *N* can be estimated from the TEM images. We observe that the islands are an average of 113 nm apart. Assuming that the islands are spaced equally, we find the number density of islands to be 7.83×10^{-5} nm^{-2} and the total number of islands to be 3.13×10^{10}. We then solve for *x* and *h*, and discard one of the solutions that has a negative *x* value. Two physical solutions suggest an island with width and depth of 22 nm and height of 26 nm, or one with the width and depth of 100 nm and a height of 12 nm. Both sets are quite reasonable with the first one being in somewhat better agreement with the measured values of 50 nm width and 36 nm height.

The above analysis assumes that the energies of the continuous film and of the islands are the same. We may also assume that there is a driving force for island formation resulting in an energy difference Δ between the two systems. Equation 10 then becomes

$$E_{Film} = A_0(\gamma_{110-Interface} + \gamma_{Pt}) + 4\sqrt{A_0}h_0\gamma_{Pt} + \Delta \quad (4.13)$$

If we start with the observed height and width of the islands as our known quantities and set equations 13 and 11 equal to each other, again with the volume constraint in equation 12, we find the total number of islands to be 4.44×10^{10} corresponding to a number density of 1.11×10^{-4} nm^{-2}. This is in reasonable agreement with the experimentally observed island density. The energy difference Δ is calculated to be -3.72×10^{15} eV, or -8.38×10^{4} eV/island; thus, the Δ per volume of an island is -9.31×10^{-4} eV/Å^3 and the Δ per atom of an island is -1.4×10^{-2} eV/atom.

4.5 CONCLUSION

Using first principles calculations we consider the thermodynamics of BTO wetting by Pt. We find that the surface energy of thin single domain BTO films polarized out-of-plane is lower than that for films polarized in-plane. We estimate the energy of the Pt/BTO interface to be between 2.51-1.64 J/m^2, depending on chemical environment. Despite a reasonable match of the lattice constant, the surface energy of both (100) and (110) Pt is too high to wet BTO. Cross-sectional transmission electron microscopy of Pt films grown on BTO by molecular beam epitaxy at high temperature and low flux shows Volmer-Weber islands consistent with first principles calculations of the surface and interface energies.

Chapter 5: Atomic and electronic structure of ferroelectric $BaTiO_3$/Ge(001) and $BaTiO_3$/$SrTiO_3$/Ge(001) heterostructures‡

In this chapter, we demonstrate the epitaxial growth of $BaTiO_3$ on Ge(001) by molecular beam epitaxy using a thin Zintl template buffer layer. A combination of density functional theory, atomic-resolution electron microscopy and *in situ* photoemission spectroscopy is used to investigate the electronic properties and atomic structure of the $BaTiO_3$/Ge interface. Aberration-corrected scanning transmission electron micrographs reveal that the Ge(001) 2x1 surface reconstruction remains intact during the subsequent $BaTiO_3$ growth, thereby enabling a choice to be made between several theoretically predicted interface structures. The measured valence band offset of 2.7 eV matches well with the theoretical value of 2.5 eV based on the model structure for an in-plane-polarized interface. The agreement between the calculated and measured band offsets, which is highly sensitive to the detailed atomic arrangement, indicates that the most likely $BaTiO_3$/Ge(001) interface structure has been identified. We also experimentally and theoretically investigate a $BaTiO_3$/$SrTiO_3$/Ge(001) heterostructure. In contrast with the $BaTiO_3$/Ge system, this heterostructure has two stable polarizations states that are polarized out-of-plane. The electrostatic potential and charge density is shown to vary with the switching of the polarization in $BaTiO_3$, indicating the field-effect.

‡ The work described in this chapter has been published as "Atomic and electronic structure of the ferroelectric $BaTiO_3$/Ge(001) interface", K.D. Fredrickson, P. Ponath, A.B. Posadas, M.R. McCartney, T. Aoki, D.J. Smith and A.A. Demkov, Appl. Phys. Lett. **104**, 242908 (2014). K.D.F. designed and performed the first-principles calculations. P.P. and A.B.P. grow the samples and performed XRD and XPS on the samples. M.R.M., T.A. and D.J.S. performed STEM on the samples. A.A.D. contributed to the theoretical calculations and the overall design of the work. The work described in this chapter has also been published as "Carrier density modulation in a germanium heterostructure by ferroelectric switching", P. Ponath, K.D. Fredrickson, A.B. Posadas, Y. Ren, X. Wu, R.K. Vasudevan, M.B. Okatan, S. Jesse, T. Aoki, M.R. McCartney, D.J. Smith, S.V. Kalinin, K. Lai and A.A. Demkov, Nat. Comm. **6**, 6067 (2015). A.A.D. contributed to the theoretical calculations and the overall design of the work. A.A.D. has devised, designed and organized the work. P.P., A.B.P. and A.A.D. designed and performed the work related to the growth of the samples. P.P. and A.B.P. performed the X-ray diffraction, XPS and AFM experiments, and analyzed the data. K.D.F. and A.A.D. designed and performed first-principles calculations. R.K.V., M.B.O., S.J. and S.V.K. designed and performed the PFM experiments and analyzed the PFM data. Y.R., X.W. and K.L. designed and performed MIM experiments and analyzed the MIM data. M.R.M., T.A. and D.J.S. performed the TEM and EELS experiments and analyzed the data.

5.1 INTRODUCTION

Direct deposition of a ferroelectric oxide on a semiconductor typically results in chemical reaction at the boundary between the two materials, yielding a thick amorphous interfacial layer and a polycrystalline ferroelectric film. Monolithic integration of perovskites on semiconductors is a very active area of research, both theoretically and experimentally.[20–24,26–29,195–200] The interfacial layer prevents the ferroelectric oxide from contacting the semiconductor in an atomically intimate manner and from having a measurable effect on the underlying semiconductor. There is tremendous interest in specifically growing perovskites with very high dielectric constants, such as $SrTiO_3$ (STO) or $BaTiO_3$ (BTO), on semiconductors.[201,202] In the case of BTO, the additional property of ferroelectricity at room temperature provides even stronger motivation for integration with semiconductors; epitaxial in-plane-polarized BTO is highly promising for microwave device applications[15] and as a non-linear optical material in electro-optic applications,[16] in addition to being a high-k dielectric. BTO, polarized out-of-plane, also has potential for realizing a ferroelectric field-effect transistor (FeFET).[203,204] Such FeFET devices offer several advantages over regular transistors for both memory and logic applications, since the state of the transistor is non-volatile, has very fast switching, and does not require any standby power.[178,179] More recently, a transistor structure with negative capacitance has been proposed that may offer sub-threshold voltage below the theoretical minimum of 60 mV/decade at room temperature.[205] Both of these device structures require BTO to be polarized out-of-plane. In particular, ferroelectric BTO can be grown epitaxially on Si with the use of an appropriate epitaxial buffer layer. When grown on Si using an epitaxial STO buffer layer, the lattice spacing of BTO is fully relaxed to that of bulk BTO at a thickness of ~40 nm.[175]

So far the ferroelectric field-effect transistor (FeFET) has so far eluded development.[206] The conceptual simplicity of the FeFET architecture, combined with the large surface polarization charge density of a typical ferroelectric (~20 $\mu C/cm^2$), an order of magnitude larger than what dielectrics can typically sustain, contribute to the obvious attraction of having a ferroelectric gate in a field-effect transistor. This seemingly straightforward approach has not yet worked because of the fundamental challenge of

combining a ferroelectric oxide directly with a semiconductor without any interfacial reaction. In order to have a substantial effect on the semiconductor charge carrier density, the ferroelectric polarization charge must be as close to the transistor channel as possible. To achieve this proximity, one must ensure the highest quality ferroelectric oxide/semiconductor interface, which requires heterogeneous epitaxy between the covalently bonded semiconductor and the ionically bonded oxide. In pioneering work, McKee *et al.* were able to interface STO epitaxially with Si,[207] thus opening up a path to integrate ferroelectric oxides such as lead zirconium titanate (PZT) and BTO with Si, using STO buffer layers.[18,175,176,208,209] However, it is nearly impossible to prevent formation of a low permittivity SiO_2 layer at the STO-Si interface during subsequent deposition of the ferroelectric oxide due to the very high reactivity of Si with oxygen. This intermediate layer prevents the ferroelectric polarization field from having any influence on the semiconductor, and also results in a depolarizing field that eventually kills the ferroelectric polarization.[210,211]

An additional challenge for achieving functioning ferroelectric devices is that in order to modulate the semiconductor charge density by switching the polarization field, the latter must be aligned normal to the oxide/semiconductor interface. However, due to thermal expansion mismatch, for example between BTO and Si, a residual in-plane tensile stress is present when the materials are cooled down after ferroelectric deposition. Hence, BTO tends to grow with its long tetragonal axis (*c*-axis), which is the direction of ferroelectric polarization, in the film plane. BTO has been epitaxially grown on Si using a variety of buffer layers but ferroelectric measurements show in-plane polarization.[212–214] Despite these difficulties, several groups have reported BTO grown on Si using various buffer layers, with *c*-axis normal to the interface.[18,175,176,209] Vaithyanathan *et al.* showed that 30-nm-thick $Ba_{0.7}Sr_{0.3}TiO_3$ can also be used as a buffer layer for growth on Si to allow the formation of *c*-axis-oriented BTO up to 10-nm thickness.[176] Dubourdieu *et al.* demonstrated *c*-axis-oriented BTO on Si using 6-nm-thick buffer layers of fully relaxed STO for BTO thicknesses of up to 10 nm.[18] Niu *et al.* reported *c*-axis-oriented BTO grown on Si using a 5-nm-thick STO buffer layer and showed a 0.75 V memory window in C-V

measurements for 90-nm-thick film grown by PLD.[209] However, the presence of a low-permittivity 2-nm-thick interfacial SiO_2 layer required relatively high voltages to achieve switching. More importantly, the modulation of charge density in the semiconductor, in other words the ferroelectric field effect, was not demonstrated. Hence, one is faced with a dual challenge when trying to realize a FeFET on Si. On the one hand, most of the electric field is dropped across the low permittivity SiO_2 layer, making it difficult to switch the ferroelectric. Conversely, even if switched, the polarization charge is removed from the channel because of the same SiO_2 layer. An alternative approach to integrating a ferroelectric directly on Si was proposed by Warusawithana *et al.*, who grew ultrathin (<4 nm) strained STO directly on Si and showed using PFM that the compressively strained STO film was ferroelectric.[215] However, no measurements of the properties of Si were made, possibly due to the difficulty in dealing with device fabrication using such ultrathin films.

As the aggressive scaling of Si metal-oxide-semiconductor field-effect transistors (MOSFETs) has effectively reached its limits, there has been renewed interest in using Ge as a channel material due to its higher hole (1900 *vs.* 500 $cm^2/V.s$) and electron (3900 *vs.* 1400 $cm^2/V.s$) mobility.[216–219] In part, this interest can be attributed to the introduction of high-*k* dielectrics, which ended the predominant role of SiO_2 as a gate dielectric and paved the way for new candidate channel materials. As the native oxide of germanium (GeO_2) is water soluble, integration of Ge with other high-*k* oxides such as $LaLuO_3$, Al_2O_3/GeO_x or TiO_2/Al_2O_3 has also been considered. Using these materials, equivalent oxide thicknesses of less than 1 nm can be achieved,[219–221] together with hole mobilities of up to 596 $cm^2/V\text{-}s$.[222] Using Zintl templates several groups have made significant progress in interfacing BTO with Ge.[52,177,223,224] Merckling *et al*. reported epitaxial BTO on thick Ge films grown on Si substrates: a ½-monolayer Ba template layer was used in analogy to the ½-monolayer Sr on Si used for STO on Si heteroepitaxy.[223] Mixed *c*-axis-oriented and cubic phase growth was reported, and no measurements of the ferroelectricity or analysis of the interface structure were made. Because the BTO was grown using atomic oxygen, the interface was possibly oxidized with a buried GeO_2 layer that would be detrimental to

direct coupling of the BTO polarization to Ge. By inserting an ultrathin STO layer between BTO and Ge, one can impose compressive in-plane strain on BTO that can overcome tensile stress caused by the thermal expansion mismatch and thereby achieve BTO on Ge with out-of-plane polarization;[176] a similar approach was recently used to grow BTO on GaAs. Ferroelectric switching of *c*-axis-oriented BTO on STO-buffered GaAs was demonstrated by Huang *et al*. using preferentially oriented films with columnar crystallites,[225] and by Contreras-Guerrero *et al*. using flat epitaxial films.[226]

In this chapter, we study the electronic and atomic properties of the BTO/Ge interface. We use MBE to grow the samples of BTO on Ge, and XRD to measure the lattice constants and crystallographic orientation of BTO. We use both XPS and STEM to model the atomic positions and bonding at the BTO/Ge interface, and use density functional theory to complete the model of the interfacial structure and the band offsets which we compare to experiment. We also study the BTO/STO/Ge interface, which we model with density functional theory and compare to experiment. We model the polarization states of BTO and their effect on the electronic structure.

5.2 BTO/GE HETEROSTRUCTURE

5.2.1 Interface Models

All calculations are done using density functional theory (DFT) in the local density approximation (LDA) using plane augmented-wave pseudopotentials as included in the VASP code.[65,66,131–134] We employ the Perdew-Zunger form of exchange-correlation potential.[135] We use the valence configuration $3p^6 4s^2 3d^2$ for Ti, $5s^2 5p^6 6s^2$ for Ba, $2s^2 2p^4$ for O, and $3d^{10} 4s^2 4p^2$ for Ge. A 600 eV kinetic energy cutoff is used. For the Brillouin zone integration we use the following Monkhorst-Pack k-point meshes:[136] 88x8 for bulk BTO, Ge and $GeOBa_3$, $8\times8\times2$ for Ge surfaces, $8\times4\times2$ for the (2×1) interface structures, and $4\times4\times2$ for the (2×2) interface structure. Bulk materials are fully optimized, and all structures except the interfacial structures are optimized with respect to the ionic positions until the forces on all atoms are less than 30 meV/Å. For the interfacial structures, the first two layers of the substrate are allowed to relax while the rest of the substrate is fixed; the

film is allowed to relax completely. The energy is converged to 10^{-6} meV. The relaxation is not constrained by symmetry. The valence band offsets of the heterostructure are calculated using the reference potential method;[227] the conduction band offsets are determined by adding the experimental band gap to the calculated valence bands, due to the underestimation of the gaps in LDA. The underestimation of the band gap in LDA leads to an additional technical complication: in some cases, the conduction band of BTO is placed below the top of the valence band of Ge, leading to an un-physically large charging of the BTO film by Ge. To counter this effect, a Hubbard U correction (LDA + U theory)[228] of 8.0 eV was added to the Ti d-states to increase the band gap.[50] Although the band gap did not reach the experimental value of 3.2 eV,[13] the calculated band gap of 2.75 eV was, in most cases, sufficient to stop unphysical oxide charging. The one uncertain case is discussed below. Since the addition of a U on the Ti d states prevents the BTO from being ferroelectric, even in bulk, we add the U only at the end of the calculations, and do not include it in the relaxations, in order to see if any of the BTO films are polarized.

For ferroelectric tetragonal BTO, we calculate the lattice constant *a* to be 3.96 Å, the lattice constant *c* to be 3.98 Å, and the polarization to be 22.9 μC/cm^2. In comparison, the experimentally measured values of the lattice constants are *a* = 3.99 Å and c = 4.04 Å, both slightly larger than the calculated values. The experimentally measured polarization varies slightly with temperature, between 17-18 μC/cm^2; however, the authors claim that using including ionic polarizibility effects would raise the values by approximately 50%, to 25-27 μC/cm^2;[229] our value lies in the middle. We also compare to previously reported theoretical values of *a* = 4.00 Å, *c* = 4.04 Å, and a polarization of 17 μC/cm^2.[167] The lattice constants are again larger, but the polarization is much smaller than our calculated theoretical values, and closer to the low end of the experimental value that does not include ionic polarizibility effects.

While in nature Ge is a semiconductor, in LDA Ge is semi-metallic, with a calculated lattice constant a = 5.62 Å, which compares favorably to the experimental lattice constant of 5.65 Å. When we treat Ge as substrate, the ferroelectric phase of BTO rotated 45° with respect to conventional cubic cell of Ge, and is under 0.4% tensile strain. To

consider the possibility of growing Ge on BTO, we consider using BTO as the substrate, and using Ge as the film; Ge has a 0.3% compressive strain when rotated 45° and matched to BTO.

When we consider the growth of Ge on BTO, we use $GeOBa_3$ (GOB) as a reference. GOB is a metallic inverted-perovskite with Ge at the A site, O at the B site, and Ba at what would be the O site in a normal perovskite (Figure 5.1). It has an orthorhombic structure characterized by tilting of the OBa_6 octahedra.[230] However, in our calculations we approximate it as a simple cubic perovskite structure, due to the large lateral unit cell that would need to be considered for an interface calculation. We find the theoretically optimized cubic lattice constant to be 5.29 Å, smaller than the experimental value of 5.368 Å; however, we do not expect the lattice constant to exactly match due to the experimental sample being orthorhombic and the theoretical cell being cubic. GOB is under 5.6% tensile strain when rotated 45° and matched to BTO.

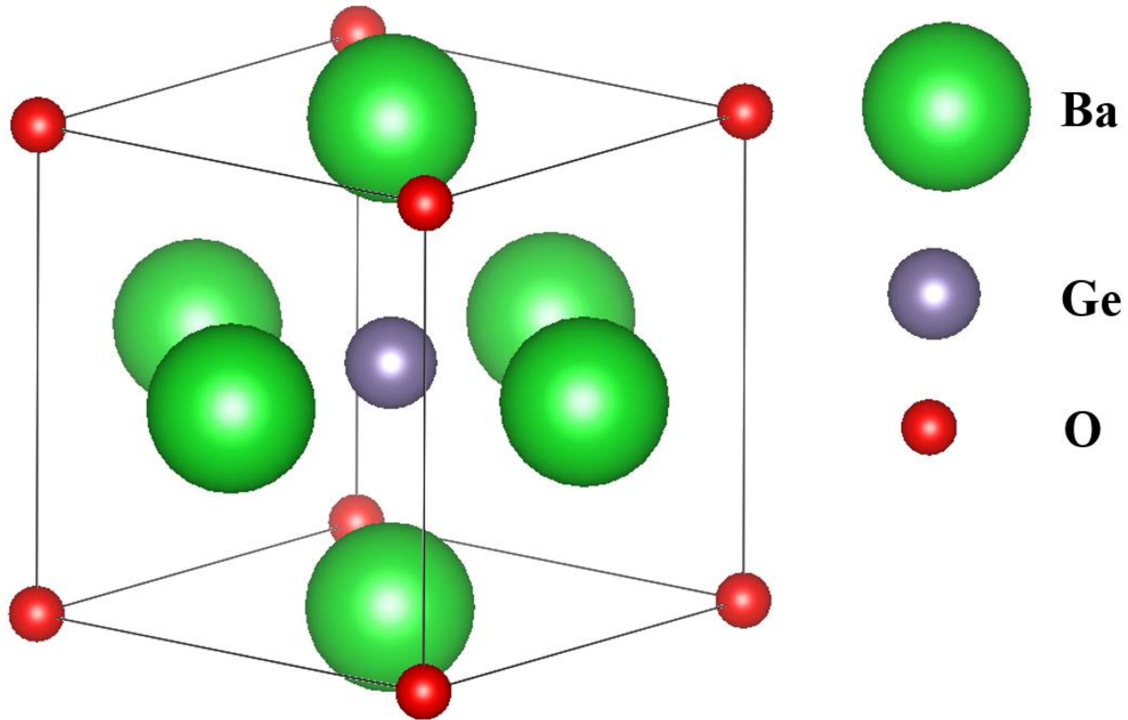

Figure 5.1 The GOB cubic unit cell.

For the BTO-on-Ge interface calculations, we use Ge slabs with thickness of 13 MLs and BTO slabs with thickness of 3.5 unit cells (UCs). We consider both BaO- and TiO_2-terminated BTO slabs. We attempt four different interfaces, in order to determine an experimentally feasible interface for the growth of BTO on Ge. For the Ge-on-BTO interfaces, we use Ge slabs with thickness of 19 MLs and BTO slabs with thickness of 4.5 UCs for the BaO-terminated interface and 5.5 UC for the TiO_2-terminated interface, with 1 UC of GOB separating the BTO and Ge slabs. We also would like to determine if it is possible to grow Ge(001) on BTO. As there are no experimental studies on the possibility of using GOB as an interfacial layer, we try both BaO and TiO_2-terminated BTO.

The calculated interfaces are shown in Figure 5.2. Figure 5.2 a)-d) are the interfaces for the BTO film on Ge substrate, and Figure 5.2 e) and f) are the interfaces for the Ge film on the BTO substrate. Notice that the Ge surface is assumed to have a (2x1) reconstruction when treated as the substrate; no such assumption was made when considering the Ge film. The interfaces considered are as follows: a) BaO-terminated BTO, with no interfacial layer; the O in BaO bond directly to the Ge dimers (Ge-O interface, Figure 5.2. a)). b) The same as the Ge-O interface, but with ½ ML of Sr passivating the wells (Ge-O Sr interface, Figure 5.2. b)). c) The same as the Ge-O Sr interface, but the BaO is shifted so that the ½ ML of Sr bonds to the O in BaO, creating rock salt-like bonding structure (Rock Salt interface, Figure 5.2. c)). d) SrO_2 interfacial layer that bonds to the TiO_2-terminated BTO; in this case, the ½ ML Sr passivation layer sits on top of the wells, rather than in them (SrO_2 interface, Figure 5.2. d)). e) The BaO-terminated BTO bonds to Ge via an interfacial GOB layer; the BaO layer in GOB forms a rock salt-like structure with the BAO surface, and the Ge bonds to the Ba_2Ge layer (GOB-BaO interface, Figure 5.3. a)). Finally, f) theTiO_2-terminated surface bonds to Ge via an interfacial GOB layer; the BaO layer in GOB forms a perovskite-like bonding with the TiO_2 surface, and the Ge bonds to the Ba_2Ge layer (GOB-TiO_2 interface, Figure 5.3. b)).

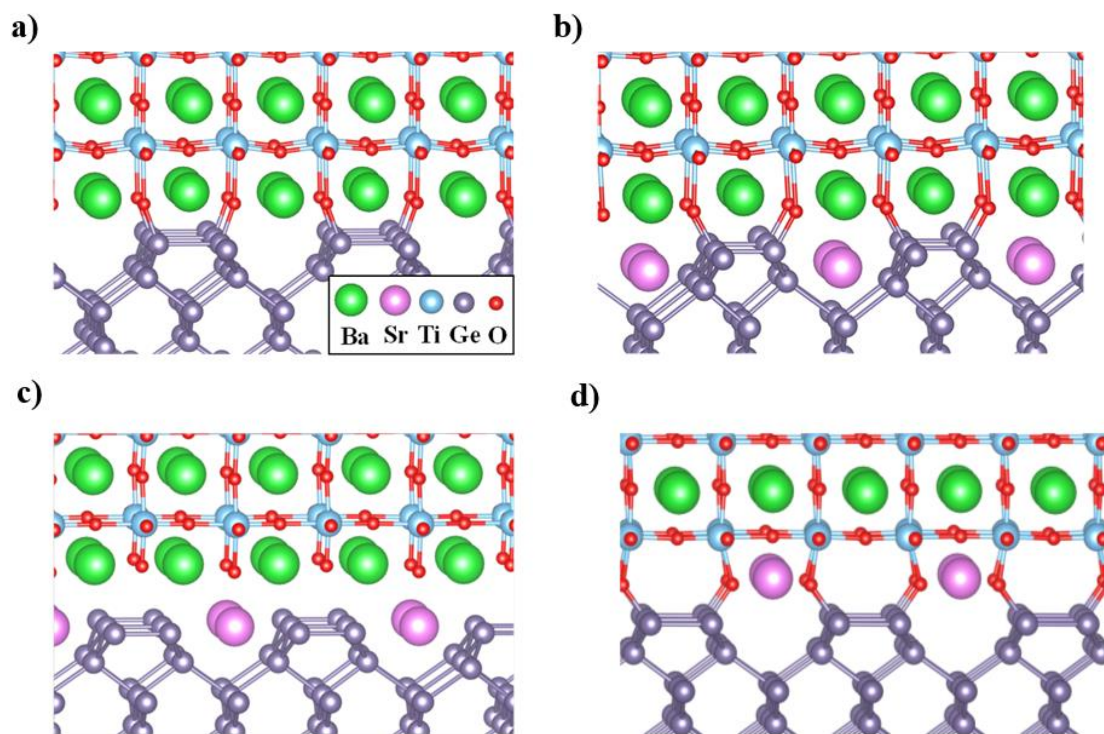

Figure 5.2. a) The Ge-O interface. b) The Ge-O Sr interface. c) The rock salt interface. d) The SrO_2 interface.

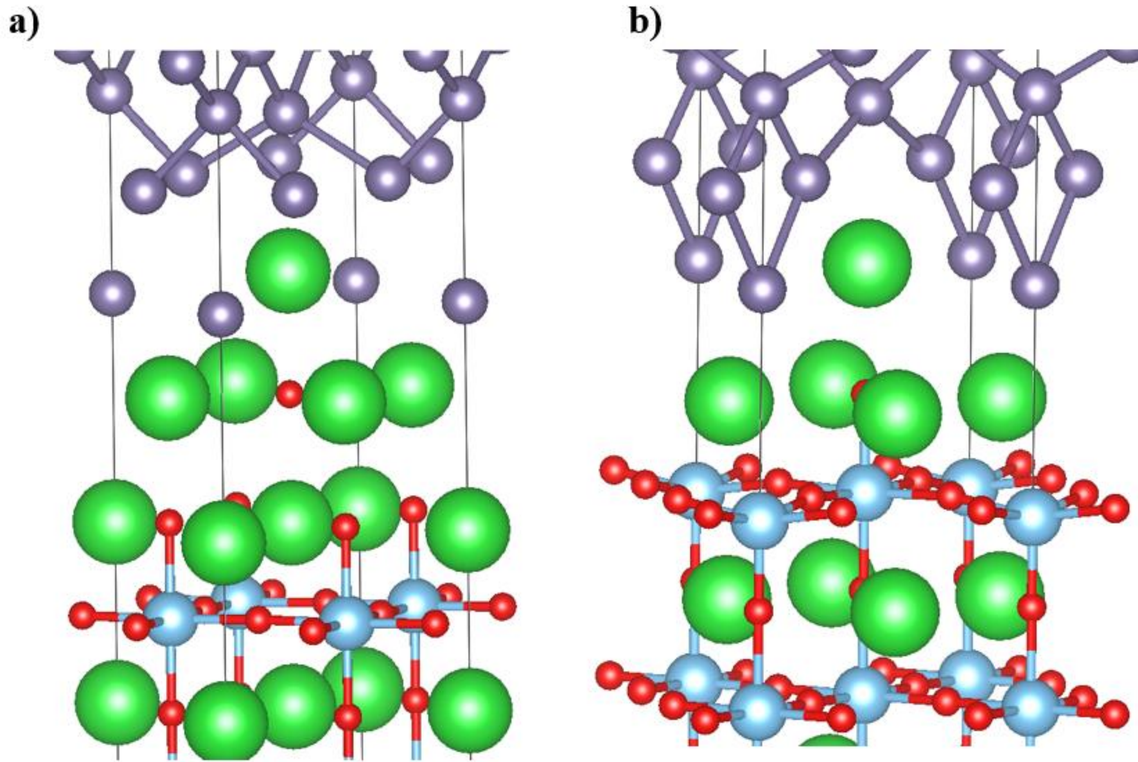

Figure 5.3. a) The GOB-BaO interface. b) The GOB-TiO_2 interface.

The band offset diagrams for the interfaces are shown in Figure 5.4. The interfacial states (if any) are shown, along with the band alignment. Theoretically, the dipole shift Δ at the interface is defined as

$$\Delta = VBO_{SL} - VBO_{TH} \tag{5.1}$$

where VBO_{SL} is the valence band offset in the Schottky limit (2.7 eV), and VBO_{TH} is the valence band offset calculated using density functional theory. Δ is a simple estimate of the degree of bonding at the interface; a larger absolute value of Δ means a larger deviation from the Schottky limit. Of note is the fact that in the Ge-O interface, Ge still charges BTO even with the addition of a U of 8.0 eV to increase the band gap. Since the gap is still not large enough to match experiment, we are unable to say if this charging is physical or not. Therefore, we have some doubts about the validity of the band offsets for this interface.

This issue does not appear in any other interface calculations. Our method for determining the band offsets of the SrO_2 interface is more complex, and is given in Section 5.2.4.

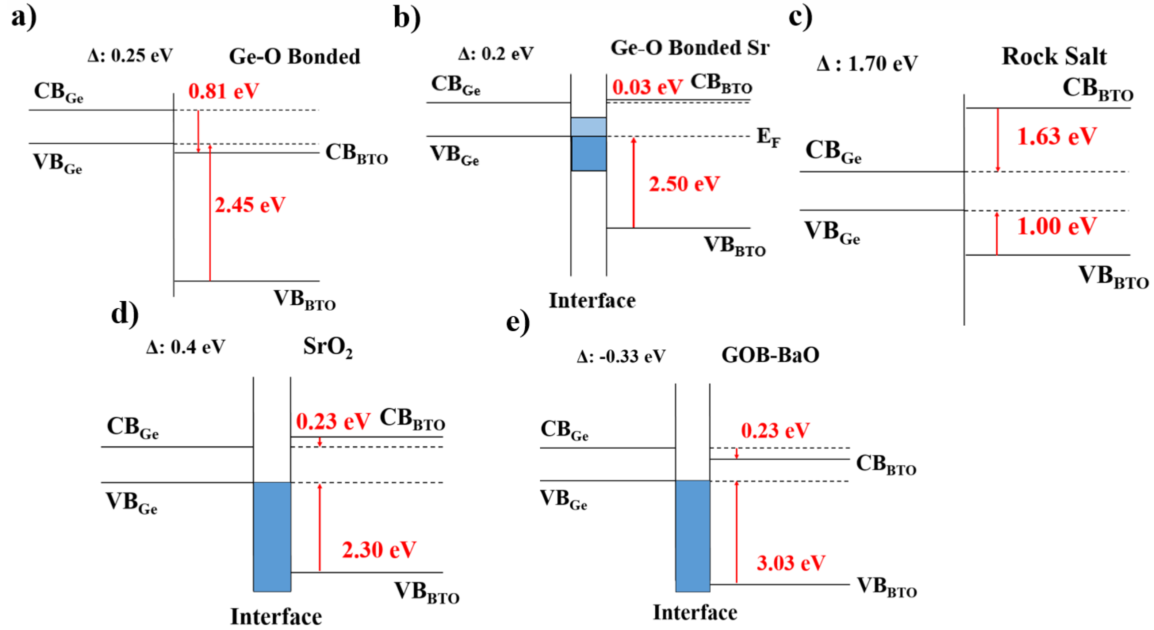

Figure 5.4. Band offset diagrams for the a) Ge-O bonded b) Ge-O Bonded Sr c) Rock Salt d) SrO2 e) GOB-BaO interface. Filled interfacial states are dark blue, and empty interfacial states are light blue.

As BTO is ferroelectric, the rumpling of the film or substrate is also of interest. The rumpling is defined as the relative shift between Ti and O (see Figure 2.3), and the polarization of BTO is linear with respect to the rumpling. For the BTO film/Ge substrate system, there are three directions of rumpling to consider; parallel with the Ge dimer and parallel with the interface [100], parallel with the Ge dimer and parallel with the interface [010], and perpendicular to the interface [001] (Figure 5.5); for the BTO substrate/Ge film system, there is only rumpling parallel to the interface and perpendicular to the interface by symmetry. We examine the rumpling of the TiO_2 layers of our heterostructures in Tables 5.1, 5.2, 5.3 and 5.4. The rumpling in the first layer of the GOB-BaO and GOB-TiO_2 interfaces are 0.025 and 0.063 Å out-of-plane, respectively (the remainder of the rumpling

is zero due the layers being fixed). We see that the specific interface with BTO greatly determines the electronic (band offsets) and atomic (polarization) properties of the BTO/Ge system.

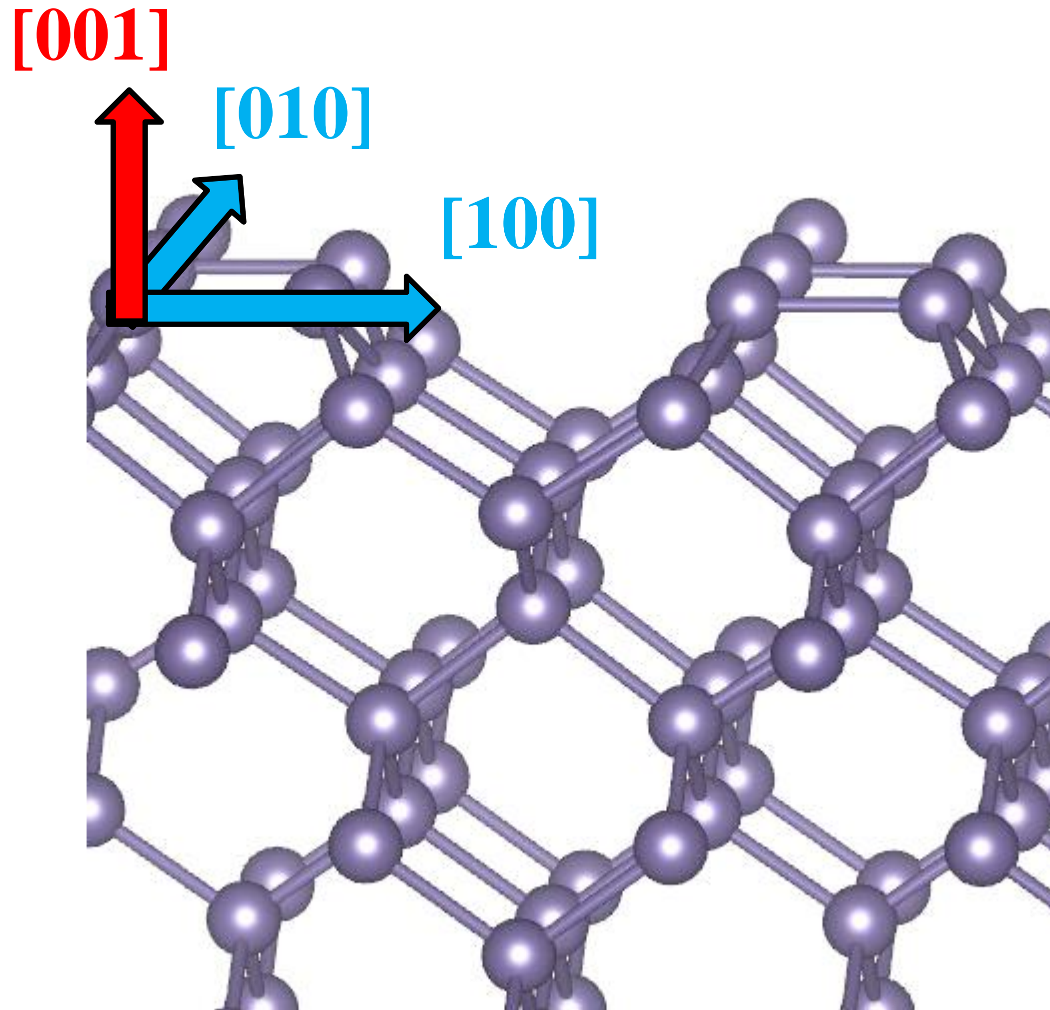

Figure 5.5. The possible directions of rumpling for the BTO film/Ge substrate system.

TiO_2 Layer #	Rumpling Parallel to Dimers (Å)	Rumpling Perpendicular to Dimers (Å)	Out-of-plane rumpling (Å)
1	0	0.039	-0.219
2	0	-0.021	-0.152
3	0	0.003	-0.087
4	0	-0.001	-0.052

Table 5.1. Structural data for the Ge-O bonded interface. TiO_2 Layer 1 is closest to the interface, Layer 4 is farthest away. A positive value means that Ti is closer to the Ge dimer than O, and a negative value means that Ti is farther away from the dimer than O.

TiO_2 Layer #	Rumpling Parallel to Dimers (Å)	Rumpling Perpendicular to Dimers (Å)	Out-of-plane rumpling (Å)
1	0	-0.106	-0.214
2	0	-0.002	-0.134
3	0	0	-0.074
4	0	0	-0.051

Table 5.2 Structural data for the Ge-O bonded Sr interface. TiO_2 Layer 1 is closest to the interface, Layer 4 is farthest away. A positive value means that Ti is closer to the Ge dimer than O, and a negative value means that Ti is farther away from the dimer than O.

TiO_2 Layer #	Rumpling Parallel to Dimers (Å)	Rumpling Perpendicular to Dimers (Å)	Out-of-plane rumpling (Å)
1	0	-0.106	-0.214
2	0	-0.002	-0.134
3	0	0	-0.074
4	0	0	-0.051

Table 5.3. Structural data for the rock salt interface. TiO_2 Layer 1 is closest to the interface, Layer 4 is farthest away. A positive value means that Ti is closer to the Ge dimer than O, and a negative value means that Ti is farther away from the dimer than O.

TiO_2 Layer #	Rumpling Parallel to Dimers (Å)	Rumpling Perpendicular to Dimers (Å)	Out-of-plane rumpling (Å)
1	0.074	0.059	0.002
2	0.080	0.079	-0.004
3	0.083	0.084	-0.008
4	0.054	0.058	-0.022

Table 5.4. Structural data for SrO_2 interface. TiO_2 Layer 1 is closest to the interface, Layer 2 is farthest away. A positive value means that Ti is closer to the Ge dimer than O, and a negative value means that Ti is farther away from the dimer than O. Note that there are only 2 layers of inequivalent TiO_2 due to this being a supercell calculation and having two interfaces.

5.2.2 Experiment

Although theory allows us to calculate any interface that we can imagine, determining which interface is the most energetically favorable is a daunting task. To validate our theoretical model, we used MBE to grow BTO on Ge(001), in order to determine the most realistic BTO/Ge interface. A customized DCA Instruments M600 MBE chamber with a base pressure of 2×10^{-10} Torr was used for depositing BTO. The crystallinity of the BTO film during growth was monitored by reflection-high-energy electron diffraction (RHEED) using 18-keV electrons at a grazing angle of 3°. The *n*-type Sb-doped (001)-oriented Ge wafers (0.029-0.054 Ω-cm) were cut into 16x16 mm^2 squares. The Ge substrates were then degreased using acetone and isopropanol, and wet-etched and oxidized using a combination of hydrochloric acid (HCl) and hydrogen peroxide (H_2O_2) to form a fresh chemically grown oxide layer. The substrate was then outgassed in vacuum at 120°C and transferred into the MBE growth chamber where it was exposed for 30 min to an oxygen plasma to remove carbon contamination from the surface and to oxidize the first few nm of the Ge surface. The sacrificial oxide was then slowly desorbed in order to produce an atomically flat, oxygen- and carbon-free surface, with very sharp (2x1) reconstruction peaks as observed by RHEED. Further details of the cleaning method used to prepare the germanium substrates are given in Ref. [231].

Prior to initiating BTO growth, a ½ ML of Sr metal was deposited onto the clean Ge(001) surface at a substrate temperature of 550 °C. This Sr Zintl template layer lowered the interface energy and facilitated two-dimensional growth.[232] An initial two unit cells of BTO were deposited on top of this layer using Ba and Ti effusion cells in the presence of $1.5\text{x}10^{-7}$ Torr molecular oxygen at a substrate temperature of 650°C. The oxygen pressure was then increased to $6.0\text{x}10^{-7}$ Torr and an additional three unit cells of BTO were deposited. Finally, the oxygen pressure was increased to $5.0\text{x}10^{-6}$ Torr and additional BTO was deposited up to the desired BTO thickness. Throughout the entire growth process, the substrate temperature was kept constant, with the deposition process consisting of alternately exposing the substrate to one ML of Ba and one ML of Ti in the presence of

oxygen. RHEED was used continuously to monitor the BTO deposition to ensure that the crystallinity of the surface was always maintained. After BTO growth to thicknesses ranging from 10 to 100 unit cells, the BTO film was cooled down to room temperature in oxygen at a rate of 5 °C/min. A RHEED pattern for a sample with 10 unit cells of BTO is shown in Figure 5.6.

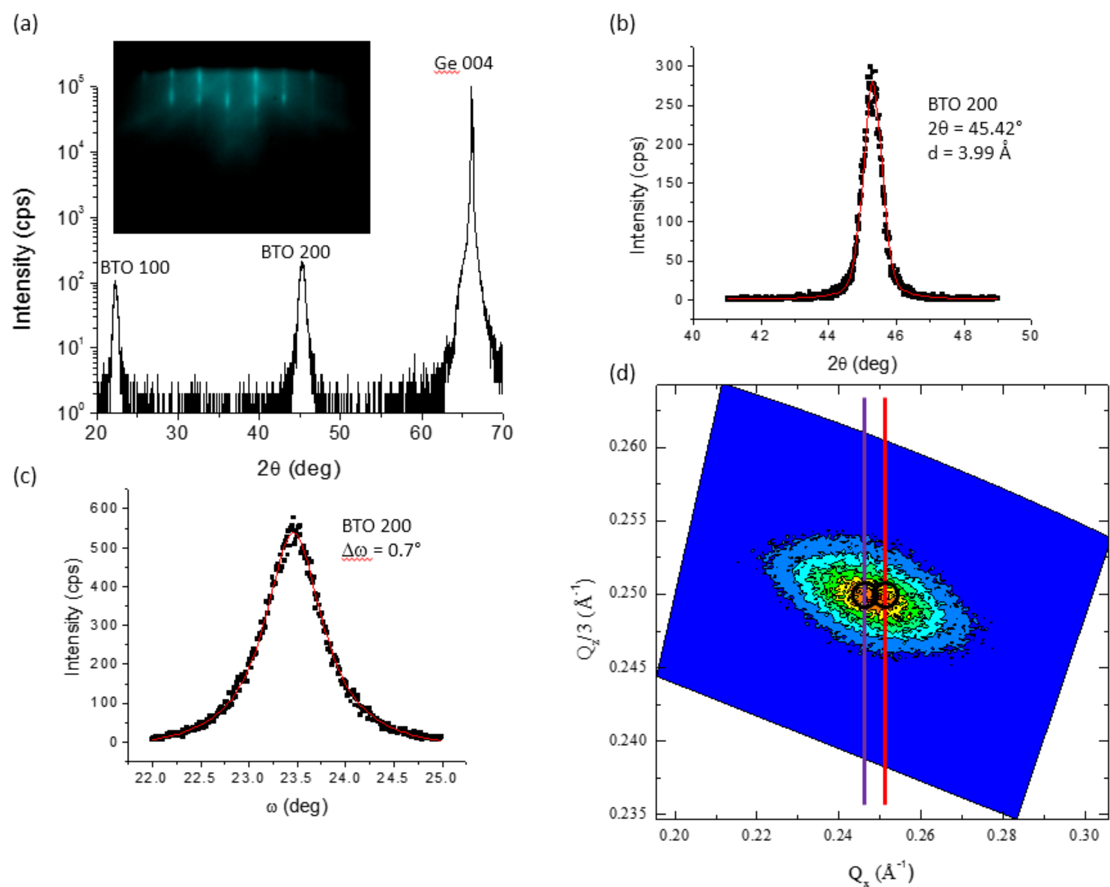

Figure 5.6. a) X-ray diffraction 2θ-θ scan of a 40 nm BTO film grown on Ge(001). Only substrate peaks and (*h*00) peaks of BTO are present indicating *a*-axis out-of-plane orientation. The inset shows a reflection high-energy electron diffraction pattern for a 12-nm-thick BTO on Ge, viewed along the <110> azimuth of BTO. b) High resolution 2θ-θ scan about the BTO(200) peak (dots) overlaid with a pseudo-Voigt function fit (solid line). The peak position indicates an out-of-plane lattice constant of 3.99 Å. c) Rocking curve scan of the same BTO/Ge sample about the BTO(200) peak, with a full width at half maximum of 0.7°. d) Reciprocal space map around the (103)/(301) reciprocal lattice point. The centroid of the feature corresponds to a = 3.99 Å and c = 4.01 Å. The small black circles indicate the positions corresponding to in-plane spacings of 4.03 and 3.99 Å. The in-plane structure is expected to have a mosaic domain structure but is unresolved in this scan.

X-ray diffraction measurements of the BTO films were carried out using a Bruker-AXS D8 Advance powder diffractometer with a Cu Kα radiation source, in order to determine the lattice constants and the crystallographic orientation. A symmetric 2θ-ω scan

of a 40-nm film of BTO on Ge (001) is shown on a log scale in Figure 5.6 b). Only peaks from the Ge substrate and a single orientation of BTO are observed. From a higher resolution scan around 2θ = 45° (Figure 5.6 c)), we find an out-of-plane lattice constant of 3.99 Å, corresponding to the shorter BTO *a*-axis pointing out of plane (i.e., 100-oriented) and implying a ferroelectric polarization lying in the plane of the BTO film. A low-resolution reciprocal space map was also performed, centered at 2θ = 75.00° and a tilt angle ψ = 18.43°, to verify the in-plane lattice constant. This scan corresponds to the (103)/(301) off-normal crystallographic planes of BTO. The result of the measurement is shown in Figure 5.6 d), plotted as reciprocal lattice spacing in the plane and normal to the plane of the film. The measurement shows a broad peak. After fitting the broad peak to a single 2D Gaussian and finding the position of the centroid of the peak, we find an in-plane lattice constant of 4.01 Å and an out-of-plane lattice constant of 3.995 Å. This confirms that the out-of-plane lattice constant is smaller than the average in-plane lattice constant consistent with ferroelectric polarization lying in the plane of the film. The in-plane lattice constant value measured for the BTO on Ge is in between the bulk *a* and *c* lattice constants of BTO. The expected positions for in-plane lattice constants that correspond to 3.99 Å (bulk *a* lattice constant) and 4.03 Å (bulk *c* lattice constant) are indicated by the vertical lines and small black circles in Figure 5.6 d). An *a*-axis orientation of BTO suggests the existence of a mosaic 90° a_1/a_2 domain structure, with the polarization lying in plane but in either of two possible directions perpendicular to each other.[233] Due to the low resolution of the reciprocal space map scan, particularly in the Q_x direction, and the closeness of the *a* and *c* lattice constants of BTO, we are not able to resolve the in-plane domain structure in this measurement.

The valence band offset between BTO and Ge was measured using x-ray photoelectron spectroscopy (XPS). The XPS system with a VG Scienta R3000 analyzer and monochromatic Al Kα radiation was connected to the MBE system allowing *in situ* sample transfer. The analyzer energy scale was calibrated using a clean Ag sample such that the binding energy of Ag $3d_{5/2}$ was 368.28 eV. The binding energy of the Ge 3d core level and the location of the valence band edge for a clean Ge sample were measured prior

to BTO growth. A thin (five unit cells) BTO layer was then grown and the Ba 3d and Ge 3d core-level binding energies were measured for the heterostructure. Finally, additional BTO was grown to a thickness of 40 nm and the Ba 3d core-level binding energy and location of the valence band edge of the thick (bulk-like) BTO were measured. The valence band edge locations for BTO and Ge were determined by linear extrapolation of the steepest descending edge to zero intensity.[234] From the measured binding energies, the valence band offset between BTO and Ge was determined to be 2.7±0.1 eV, which was in good agreement with the value reported in Ref. [177].

Cross-sectional images of the BaTiO3-Ge interface were obtained using a probe-corrected JEOL ARM200F scanning transmission electron microscope (STEM), operated at 200 keV and having a nominal probe diameter of ~0.8Å. Figure 5.7 a) shows an aberration-corrected, high-angle annular-dark-field (HAADF) image of the BTO-Ge interface, where the sample thickness in projection along the beam direction is estimated to be ~15-20nm, which would correspond to averaging over about 40-50 BTO unit cells. The individual Ba and Ti(O) atomic columns are clearly visible in the epitaxial BTO layer, and the atomically sharp nature of the interface between the two materials is clearly evident. Extensive observations along the BTO-Ge interface revealed that the uppermost pairs of Ge atomic columns ("dumbbells") displayed both 1x and 2x periodicities, indicating that the Ge 2x1 surface reconstruction had been retained during the epitaxial BTO growth. Furthermore, changes in the periodicity from 2x to 1x were observed at single-layer-high steps of the Ge surface (Figure 5.7 b)), as might be expected from previous studies of Ge(001) reconstructed surfaces using scanning tunneling microscopy.[235] However, it should be noted that the increased vertical separation between the top Ge column of atoms and the Ba/Sr atomic columns apparent in this image only occurs in the close vicinity (~1-3nm) of the terrace steps but not elsewhere across most of the terrace. Finally, as shown by the overlaid structural model in Figure 5.7 c), the Ge dimer pairs at the interface in the latter case show a decided inward slant towards each other. This highly characteristic appearance proved to be decisive in choosing between alternative models of the interface structure, as described in the following.

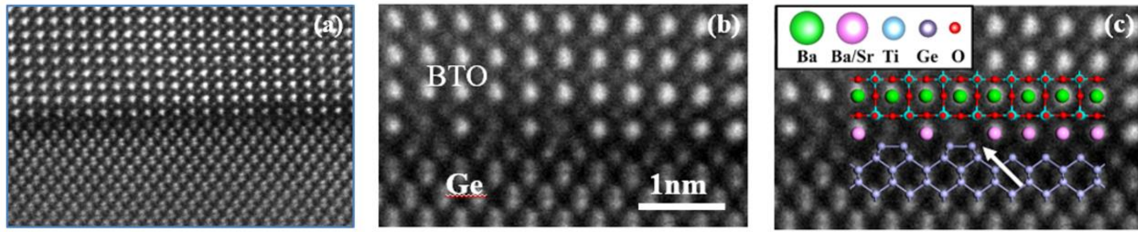

Figure 5.7. a) High-angle annular-dark-field aberration-corrected electron micrograph showing abrupt nature of BTO/Ge interface. b) Enlarged view of BTO/Ge interface showing a region of the BTO-Ge interface with both 2x and 1x periodicities visible along the plane of the interface. c) Same image with overlaid structural model. Arrow indicates step edge in Ge corresponding to transition between 2x and 1x periodicity of the reconstructed Ge surface viewed in [110]-type projection.

Since the STEM imaging was unable to clearly discern the presence of any oxygen at the interface, to determine the presence and nature of Ge-O bonding at the interface, we measured the Ge 3d core level spectrum of a sample with a BTO thickness of 4 nm, which is sufficiently thin to see Ge through the BTO layer. Figure 5.8 shows the presence of Ge at the interface with a chemical shift of 2.1 eV to higher binding energy with respect to the Ge elemental peak. Such a chemical shift has been reported in $LaGeO_x$ and $YGeO_x$ and ascribed to metal-O-Ge bonding.[236,237] From this result, it was assumed that the interface was fully oxidized, which was then incorporated into the structural model of the interface.

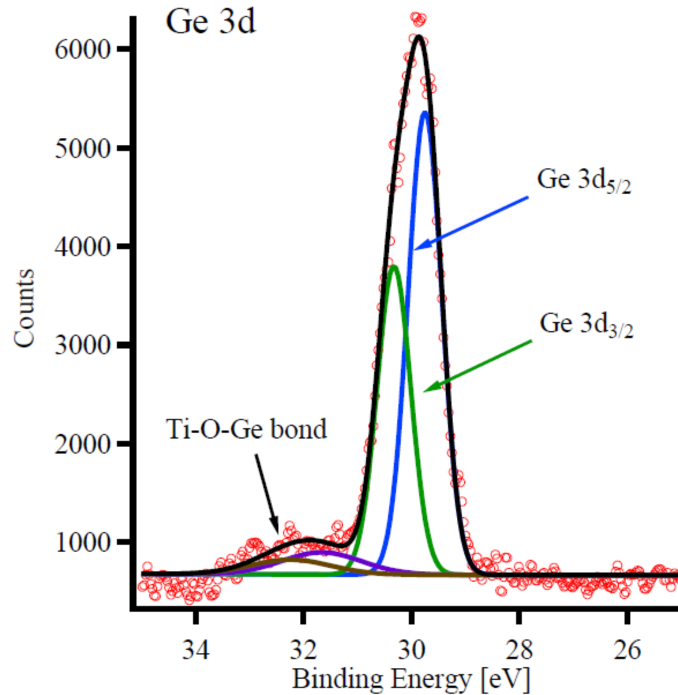

Figure 5.8. Ge *3d* core level spectrum for a sample with 4-nm-thick BTO overlayer. There is a chemical shift of 2.1 eV that is consistent with metal-O-Ge bonding.

5.2.3 Band Offset Matching

The interface geometry suggested by STEM and XPS was then refined using density functional theory. The most similar theoretical model is the SrO_2 interface, pictured in Figure 5.2 d). The BTO is TiO_2-terminated at the interface and is polarized parallel to the interface plane along the [110] direction. Initially, a ½ Sr ML Zintl layer is placed directly above the troughs of 2×1 reconstructed Ge, as suggested by the STEM image. Oxygen is incorporated at the interface as suggested by XPS, with Ti-O-Ge bonding.

The aberration-corrected electron micrographs provided useful insights into the interfacial structure, but some features were still unclear: The exact position of the ½ ML Sr above the interface was difficult to determine. Moreover, although XPS established the presence of O at the interface, it was not visible in the STEM images due to its small atomic number as well as possible interfacial disorder. Thus, in order to finalize the structure, we

tried to match the theoretical valence band offset to the experimental values. The physics of the valence band offset formation at the interface of a wide band gap insulator and semiconductor is as follows. In the Schottky limit, the band discontinuity is controlled by the electron affinity and band gaps of the two materials. Since the affinities of BTO and Ge are similar, this implies that the top of the valence band for Ge aligns slightly above the mid-gap for BTO. Once the two materials are brought into direct contact, electrons of the Ge valence band can occupy evanescent states in the oxide gap, which would result in the oxide being negatively charged and the semiconductor being positively charged. The resulting band line-up moves away from the Schottky limit as required by the charged double layer (interface dipole), which is precisely the Schottky barrier formation mechanism in semiconductors. However, significant lattice polarizability in oxides results in additional screening that pushes electrons from the evanescent states back into the semiconductor in order to restore the Schottky line-up. Interfacial oxygen is often the most polarizable species present.[238]

By performing model calculations, the band offset was found to be affected by the relative positions of Sr and O with respect to the BTO film and Ge substrate. More importantly, the relative displacement of O and Sr in the direction normal to the interface had an enormous effect on the band offset. Changing the relative vertical positions of the O and Sr by fixing Sr and moving O, we calculated the band offset as a function of this distance. Using a linear fit, we estimated the relative displacement necessary to match the experimental valence band offset of 2.7 eV, to be 0.59 Å. This separation is close to the value that was inferred from the STEM image.

To further refine the location of interfacial oxygen, it was assumed that the system preferred to have equilibrium Ge-O and Ti-O bond lengths of 1.64 Å[239] and 2.04 Å,[240] respectively. The O atoms were placed to match the bonding with Ge and Ti (the Ti-O bonds are slightly longer than experiment due to in-plane rumpling, which moves Ti further away from O). The Sr atoms were then placed 0.59 Å above the O atoms, and the band offset calculated. The valence band offset was then calculated to be 2.3 eV, which was in

reasonable agreement with the experimental value of 2.7 eV. We attribute the discrepancy to possible changes in the interface chemistry.

For this interface, we find a Δ of 0.4 eV. This value is a self-consistent result of charging the evanescent states of Ge and screening by the interfacial oxygen. Experiment, however, suggests essentially a Schottky alignment with no dipole shift. Atomic-column-resolved electron-energy-loss spectroscopy indicates cation exchange at the interface that leads to the interface Sr being replaced by Ba. Replacing half or all Sr atoms at the interface with Ba increases the calculated valence band offset to 2.37 or 2.44 eV, respectively. Analysis of the charge density reveals that with Ba at the interface, the charge density is shifted further towards O, raising the potential on the oxide site and leading to a larger band offset. Similarly, introducing an oxygen vacancy in the Ti-O-Ge bridge results in a band offset of 2.49 eV. The 0.2 eV shift in the band offset due to cation exchange at the interface is in excellent agreement with experiment: in samples where Sr remained at the interface the band offset is 2.5±0.1 eV.

To investigate the interface structure at the step edges, we took the previously mentioned BTO/Ge heterostructure and removed the first layer of Ge, and dimerized the next layer (the new dimer direction is now rotated 90º from the original orientation). We allow the BTO and interfacial SrO_2 to relax completely; we allow the top two ML of Ge to relax and fix the rest. The structure is relaxed until the forces are smaller than 0.07 eV/Å. We find that the O with Ge dimers directly below them migrate down to sit on top of the Ge dimers; this is surprising, as they are already bonded with the TiO_2 layer directly above them. The other O with no dimers below them stay in essentially the same place. The Sr atoms do not move appreciably (Figure 5.9 a)). We use this fact to explain the interface at a step edge; see Figure 5.9 b). On the left, the interface is the same as before. There is a step edge where the first ML of Ge is gone; the center area is the same interface as in Figure 5a, rotated 90º due to the rotation of the Ge dimers in the next layer down. Note that there the distance between Ge and the TiO_2 plane is increased from the left area; we base this on the step edge pictured in Figure 5.7 c), where there is no visible shift of the BTO downwards to keep the same TiO_2-Ge distance on both sides of the step. On the right side

of the figure, there is another step, with the dimers parallel to the original dimers on the left area. In order to keep a clean BTO/Ge interface matching that on the left side, there must be some step-edge reconstruction. We suggest that a rock salt BaO structure will form to compensate for the step edge; this satisfies the O and Ba on both sides of the step edge.

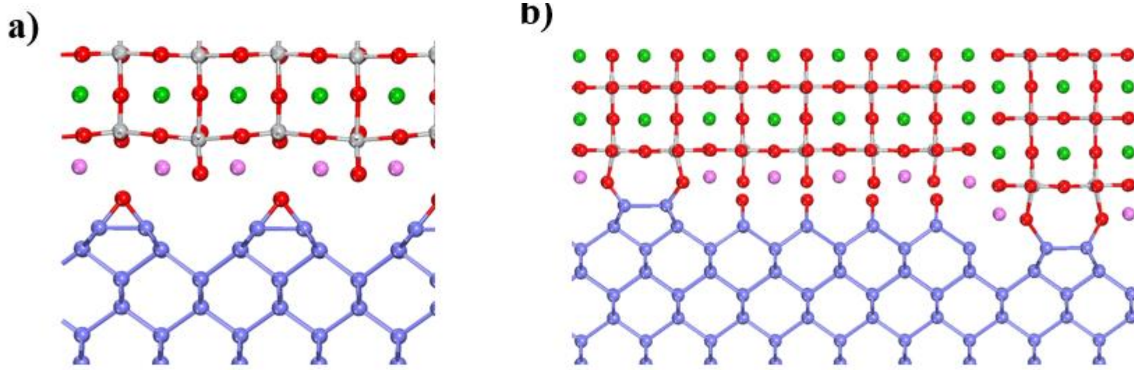

Figure 5.9. a) Calculated structure of the BTO/Ge interface after a step. Note that half of the O at the interface has relaxed to be on top of the Ge dimers. b) The BTO interface showing influences of two steps. Before the first step, the interface is the same as Figure 5.4. After the first step, the interface is that of Figure 5.5 a), rotated 90°. After the second step, the interface is the same as before either of the steps. In order to maintain the same interface, we propose a rock salt bonding between the BTO on either side of the steps.

5.2.4 Conclusion

In conclusion, the epitaxial growth of *a*-oriented BTO on Ge(001) substrates has been experimentally demonstrated using molecular beam epitaxy with a 1/2 ML Sr Zintl template. We calculated the band offsets and rumpling for a variety of differen possible BTO/Ge interfaces. Aberration-corrected electron microscopy was used to examine the atomic structure of the interface and showed conclusively that the (2×1) dimer structure of the reconstructed Ge(001) surface structure had been preserved during subsequent growth. The valence band offset across the interface was measured by x-ray photoelectron spectroscopy to be 2.5-2.7eV, whereas values in the range of 2.3-2.5eV, depending on the interface stoichiometry, were calculated using density functional theory. The close agreement between theory and experiment strongly suggests that the most likely

BTO/Ge(001) interface structure has been identified. We also offer an explanation for how the BTO/Ge interface is maintained across step edges.

5.3. BTO/STO/GE HETEROSTRUCTURE

5.3.1 Theory

To establish the feasibility of achieving the field effect in the presence of the STO layer, we performed first-principles calculations of the BTO/STO/Ge stack. Previous density functional theory (DFT) calculations have shown that BTO strained to STO remains ferroelectric even with only 1 unit cell of BTO present, but the effect of polarization on the potential in the semiconductor layers beneath has not yet been considered.[41] All calculations are done using density functional theory in the local density approximation using plane augmented-wave pseudopotentials as included in the VASP code.[65,66,131–134] We employ the Perdew-Zunger form of exchange-correlation potential.[135] We use the valence configuration $3p^6 4s^2 3d^2$ for Ti, $5s^2 5p^6 6s^2$ for Ba, $2s^2 2p^4$ for O, and $3d^{10} 4s^2 4p^2$ for Ge, $4s^2 4p^6 5s^2$ for Sr, and $2s^2 2p^1$ for B, and a 600 eV kinetic energy cutoff. For the Brillouin zone integration, we use a Monkhorst-Pack 6x3x1 mesh for the BTO/STO/Ge heterostructure.[136] To satisfy the periodic boundary conditions along the stacking direction in the presence of the internal field, we use a vacuum slab with mirror symmetry. To create the BTO/STO/Ge/STO/BTO heterostructure, we start with a BTO/STO/BTO vacuum slab. Ten and a half unit cells (UC) of BTO, with both sides TiO2-terminated, are followed with 6 UC of STO (beginning and ending with SrO) followed with another 10.5 UC of BTO, with both sides TiO2- terminated. We then add 15.0 Å of vacuum to prevent spurious slab-slab interactions. We are left with a mirror symmetric cell. We use a lateral lattice constant of 3.98 Å, which is $1/\sqrt{2}$ times the calculated lattice constant of Ge (5.63 Å), in anticipation of later building the BTO/STO/Ge slab and assuming Ge to be the substrate. We perform full relaxation until the forces are converged to less than 0.08 eV/ Å, and find that there are two stable structures; one with the BTO polarized inward, away from vacuum and toward STO, and one with BTO unpolarized

(except for the first two TiO2 planes that are polarized away from the vacuum). The following procedure is identical for both of the polarized states. We insert 8 monolayers (ML) of Ge in the center of the slab, with the top layer of Ge on either side of the slab dimerized, and the STO/Ge interface based on the ½ ML Sr Zintl structure.[20,25,232] Thickness of BTO is reduced to 7.5 UC to facilitate the speed of the calculation. Keeping the inner 4 ML of Ge and BTO fixed we perform another relaxation. Finally, we substitute one of the Ge atoms in the center of the heterostructure with B to emulate the p-type doping of Ge used in experiment. We calculate a plane-averaged electrostatic potential to obtain an electrostatic potential along the direction normal to the heterostructure stacking. A running average is performed twice over the plane-averaged potential to obtain a macroscopic potential shown in Figure 5.10.

The simulation cell and the macroscopic average of the electrostatic potential across it are shown in Figure 5.10. We find that there are two stable states of polarization. One, which we call P_1, is essentially un-polarized and another, which we call P_2, is polarized "down" with Ti shifted away from the vacuum. In state P_1 the few near-surface planes of BTO are polarized "down" with the remainder of the layers being essentially flat. This is an artifact of the 2.8 nm thickness of BTO used in the calculation. The initial inward ("down") relaxation of Ti is induced by the surface and is well documented in TiO_2.[241] Of course, the local potential in the BTO bulk is totally symmetric. Therefore, polarization could be "up" or "down", but the "up" polarization requires a head-to-head domain wall as one approaches the film surface. As the energy of such a wall, 0.11 J/m^2, is too high it is suppressed in ultra-thin films.[242] We will revisit this issue when discussing the electron microscopy results. We then examine the electrostatic potential for both polarization states. When comparing the difference in potential of the polarized and unpolarized heterostructures, we find a clear difference in electrostatic potential in the Ge layer as a result of switching between the two stable states of BTO polarization; for the B doped Ge, we find a potential energy difference of 1.09 eV, and for the pure Ge we find a potential energy difference of 1.22 eV. This indicates that the presence of high-permittivity STO layer does not interfere with a robust field effect.

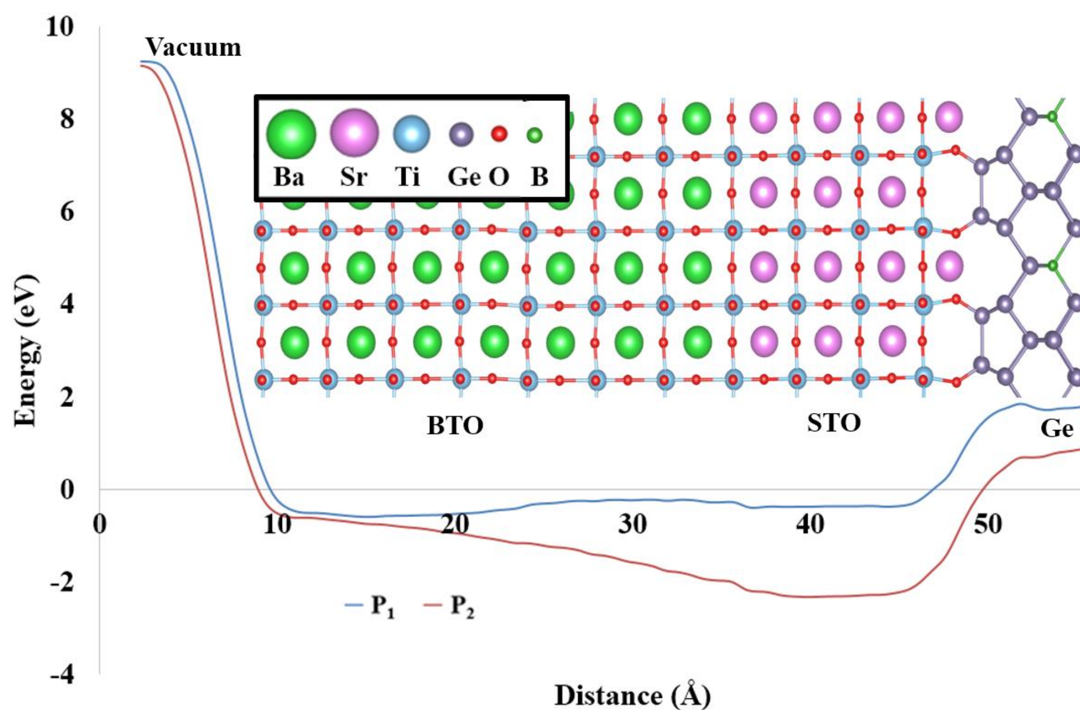

Figure 5.10. The supercell used in the DFT calculations, consisting of vacuum, BTO, STO and B-doped Ge. The cell is mirrored on the other side (not shown). Note the recession of the Ti from the surface, indicating polarization away from the BTO surface, and toward the BTO/STO interface. Below, we show the macroscopic average of the plane-averaged electrostatic potential for the P_1 and P_2 states.

5.3.2 Experiment

The Ge surface is prepared using a combination of wet-etching, oxygen plasma cleaning and annealing, resulting in a (2×1) reconstruction, low surface roughness, and clear surface signal in the angle resolved photoemission spectrum.[231] Prior to BTO growth, ½ monolayer of strontium is deposited to prevent germanium from oxidizing during the initial growth of the first 5 unit cells of STO at 200°C. After increasing the temperature to 600°C to crystallize the STO, BTO is co-deposited on the STO/Ge template at a temperature of 650°C. A reflection-high-energy electron diffraction (RHEED) pattern of a 15-nm-thick film of BTO is shown in the inset of Figure 5.11 a). *In situ* X-ray photoelectron

spectroscopy (XPS) measurements are carried out, to determine the stoichiometry of the grown film.

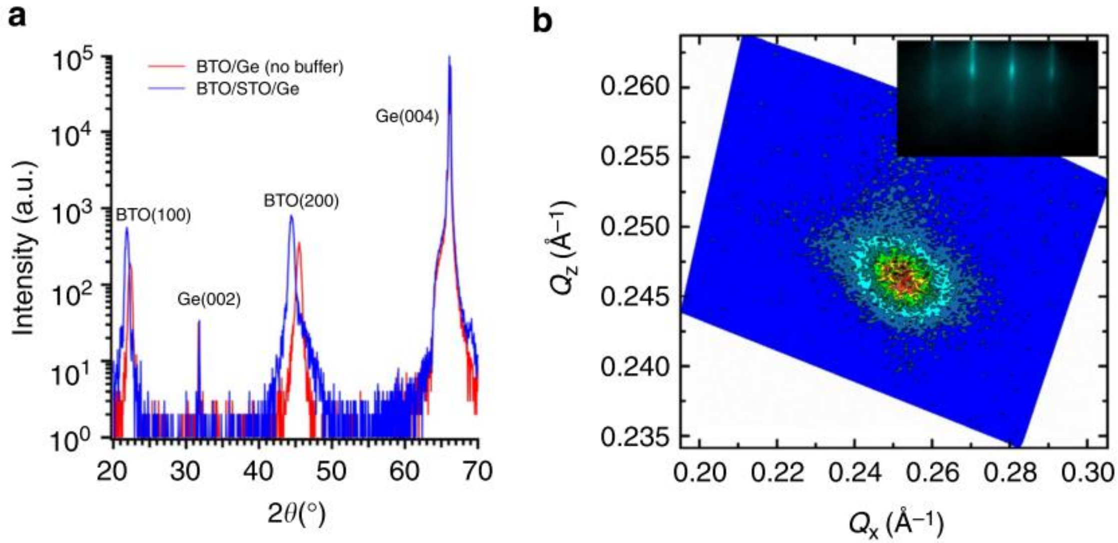

Figure 5.11. a) X-ray diffraction θ-2θ scan of 16 nm $BaTiO_3$ epitaxially grown on Ge(001) substrate, with and without a 2 nm $SrTiO_3$ buffer layer. Without the buffer, the d-spacing corresponds to the *a*-axis of BTO directed out of plane. With the STO buffer, the *c*-axis of BTO is directed out of plane. b) Reciprocal space map of the (103) Bragg reflection for BTO/STO/Ge. The centroid of the peak is consistent with a short in-plane axis and long out-of-plane axis. The inset shows a typical RHEED pattern for BTO/STO/Ge taken along the [110] azimuth showing good crystallinity and surface flatness.

Films were characterized by X-ray diffraction (XRD) performed on the BTO/Ge samples using a Philips X'Pert double-crystal diffractometer. Figure 5.11 a) shows symmetric θ-2θ scans of a 160-Å-thick BTO film grown on Ge, both with and without a 20-Å-thick STO buffer layer. The BTO peaks correspond to a single orientation with an out-of-plane spacing of 4.06 Å for the film with the STO buffer, and 3.98 Å for the film without the buffer. This result clearly demonstrates the *c*-axis orientation for the STO-buffered sample compared with the *a*-axis orientation for the BTO layer grown directly on Ge. Figure 5.7 b) shows a reciprocal space map around the (103) Bragg reflection for the *c*-axis oriented sample. The measured lattice constants after fitting with a 2D Gaussian are

a = 3.96 Å and c = 4.06 Å**.** Rocking curve scans around the BTO 002 Bragg peak typically show a full-width at half-maximum of 0.5-0.8°.

The crystalline quality of the BTO layer and the GeO_2-free Ge surface are confirmed using cross-section aberration-corrected electron microscopy. Electron micrographs clearly reveal that the BTO layer is coherently strained to the partly relaxed STO buffer, with no dislocations visible along considerable lengths of the BTO/STO interface. Aberration-corrected images were recorded using a probe-corrected JEOL-ARM200F, as shown in Figure 5.12) a. Individual Ti, Ge, Sr and Ba atomic column locations can be identified in both bright-field and high-angle annular-dark-field images, while Fourier transforms (diffractograms) of these images also confirm the tetragonality of the BTO with the longer c-axis pointing out of the plane (Figure 5.12 b)). Closer examination at higher magnification reveals that the Ti atomic columns close to the top of the BTO film are shifted downwards from the cell center whereas in regions close to the STO film they are displaced slightly upwards (Figures 5.12 c) and d)). The "down" polarization near the surface is in agreement with the theoretical prediction.

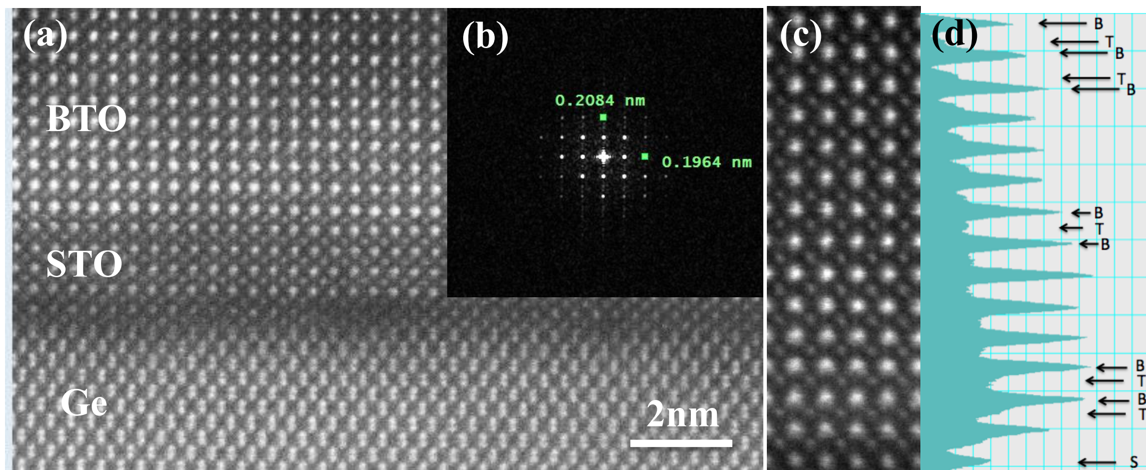

Figure 5.12. a) High-angle annular-dark-field (ADF) image of BTO/STO/Ge(001) heterostructure recorded with 200-keV probe-corrected scanning transmission electron microscope. White spots correspond to positions of metal atoms. b) Fourier transform of ADF image confirming tetragonality of BTO layer. c) Enlargement of ADF image showing region of BTO film. d) Corresponding line profile from c) showing shifts in Ti atomic-column positions.

The ferroelectric properties of the BTO layer were then tested using Band-Excitation Piezoresponse Force Microscopy (BE-PFM).[243] Results from a typical BE-PFM switching experiment are shown in Figures 5.13 a)-c), where a 5 x 5 μm^2 square was initially poled with the tip held at -6 V, and a smaller 2.5 x 2.5 μm^2 square within the original square was then poled with the tip held at +4 V. The topography in Figure 5.13 a) shows no change in the poled areas, suggesting no irreversible electrochemical reactions at the surface. At the same time, the vertical BE-PFM amplitude and phase images in b) and c) indicate clear and sharp boundaries, which are signatures of written ferroelectric domains, and largely obviate tip-injected surface charge effects dominating the contrast. This experiment also confirms that the BTO film outside the poled regions is monodomain, with polarization oriented towards the STO/Ge substrate in agreement with the theoretical predictions.

In order to further characterize the ferroelectric properties of the BTO film, we carried out BE- Piezoresponse Spectroscopy measurements (BEPS)[244], where the tip is placed at a particular position, a DC waveform is applied to the tip and simultaneously the BE-response is captured to yield the system's response. We performed a BEPS measurement on the BTO film across a 10×10 grid to yield a dataset of 100 measurements in total; the average spectrogram of the response (amplitude and phase) is shown in Figure 5.13 d), with the DC waveform shown inset. Three selected responses at individual points from the 100 measurements, after fitting to a simple harmonic oscillator (SHO) model are shown in Figures 5.13 e) and f). The average of 100 measurements is shown as a solid olive line. The amplitude curves clearly follow the expected butterfly-like hysteresis typical of ferroelectrics, while the phase loop appears to show a change somewhat less than 180°. The latter effect is probably due to a slight electrostatic contribution to the signal, which cannot be ruled out due to the lack of a bottom electrode in this sample. We also note that the coercive voltage appears largely symmetric with only a small offset, with values around ~ +4 V and ~ -5 V.

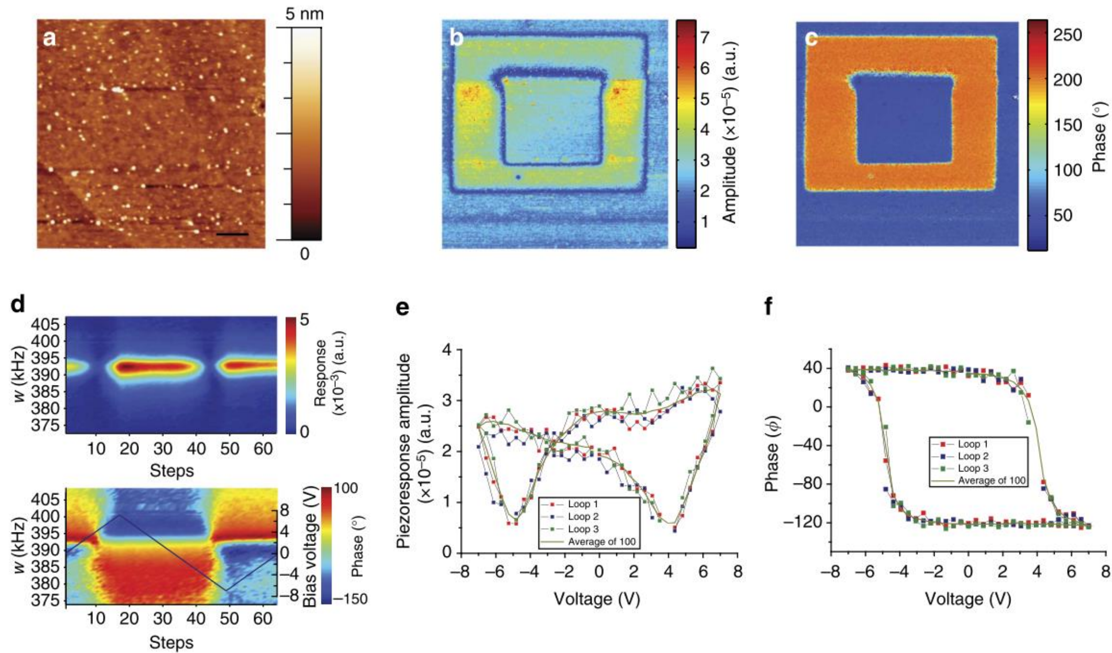

Figure 5.13. a) Topography, b) BE-PFM amplitude and c) associated phase image after a box-in-box switching experiment on the BTO heterostructure, showing clear ferroelectric switching. A 5 x 5 μm^2 box was poled with the tip held at -6 V, and then a smaller box 2.5 x 2.5 μm^2 was subsequently scanned with the tip held at +4 V before the BE-PFM images were captured. 100 hysteresis loops were then captured on the same film using BE spectroscopy. The average response is shown in the spectrograms in d) for amplitude (above) and phase (below), with the applied DC waveform shown in blue. Selected e) amplitude and f) phase loops are shown, with the average loop shown as a solid line in olive.

Having demonstrated that the BTO layer is both polar and ferroelectric, we next turn to addressing the field effect. Due to the difficulty in fabricating BTO/Ge transistors, we utilize microwave impedance microscopy (MIM) to measure the conductivity of the underlying Ge.[245–248] MIM is a novel imaging tool used to spatially resolve the local permittivity and conductivity of materials,[249–251] and was employed to demonstrate the ferroelectric field effect in the BTO/STO-Ge heterostructures. Here the 1 GHz excitation signal is delivered to a specially designed cantilever probe and the evanescent wave from the tip apex, with a diameter of 20-100 nm, interacts with the sample underneath.[252]

The modulation of the carrier density at the ferroelectric-Ge interface results in appreciable impedance change of the tip, which is readily detected by the MIM electronics. As shown schematically in Figure 5.14 a), a DC voltage of -4 V is also applied to the conductive MIM tip through a bias-tee to locally switch the BTO polarization. After a 20 × 20 μm^2 square was written, the DC bias was removed and a larger region concentric with the previous scan was then imaged by the same tip using PFM and MIM, both of which show clear contrast between the written and unwritten areas. The PFM contrast (Figure 5.14 b)) again confirms that BTO polarization is reversed by a sufficiently large negative tip bias, with no corresponding topographic features. In Figure 5.14 c), the poled area shows substantially lower MIM-Re and slightly higher MIM-Im signals than the intact region. Since neither the conductivity ($\sigma_{BTO} = 0$) nor the first-order dielectric constant (ε_{BTO}) of the BTO is affected by the polarization reversal, the MIM contrast must come solely from the underlying Ge layer accompanied by the poling process. We also confirmed that the PFM and MIM contrast is not observed for a smaller negative tip bias ($|V_{tip}| < 4$ V) or a positive bias up to +4 V, indicative of a ferroelectric switching process.

Finite-element modeling was performed to analyze the effect of carrier modulation in Ge on the MIM signals.[250] Since the near-field interaction is highly dependent on the exact tip-sample contact condition, the simulation only serves as a qualitative guide to the experimental data. As shown in Figure 5.14 d), the MIM-Im signal, which is proportional to the tip-to-ground capacitance, rises monotonically with σ at the BTO/STO-Ge interface. On the other hand, the MIM-Re signal, which represents electrical loss within the probing volume, peaks at an intermediate σ_{Ge}. The higher MIM-Im and lower MIM-Re signals in the patterned square hence indicate a larger interfacial σ_{Ge} than that of the unwritten area. As elaborated below, the MIM data clearly corroborate the conclusion of DFT calculations and STEM images that the polarization of the as-grown BTO layer is pointing towards the underlying Ge substrate. This as-grown ferroelectric polarization partially depletes holes in the p-type Ge (left inset of Figure 5.14 d), giving rise to a lower interface conductivity than the bulk. After the BTO polarization is reversed by a sufficiently large negative tip bias, the energy bands drastically bend upwards (right inset of Figure 5.14 d)) and holes

accumulate near the BTO/STO-Ge interface. As a result, σ_{Ge} is much enhanced at the heterojunction, leading to the observed MIM contrast. To the best our knowledge, this is the first demonstration of carrier density modulation in semiconductors due to ferroelectric switching.

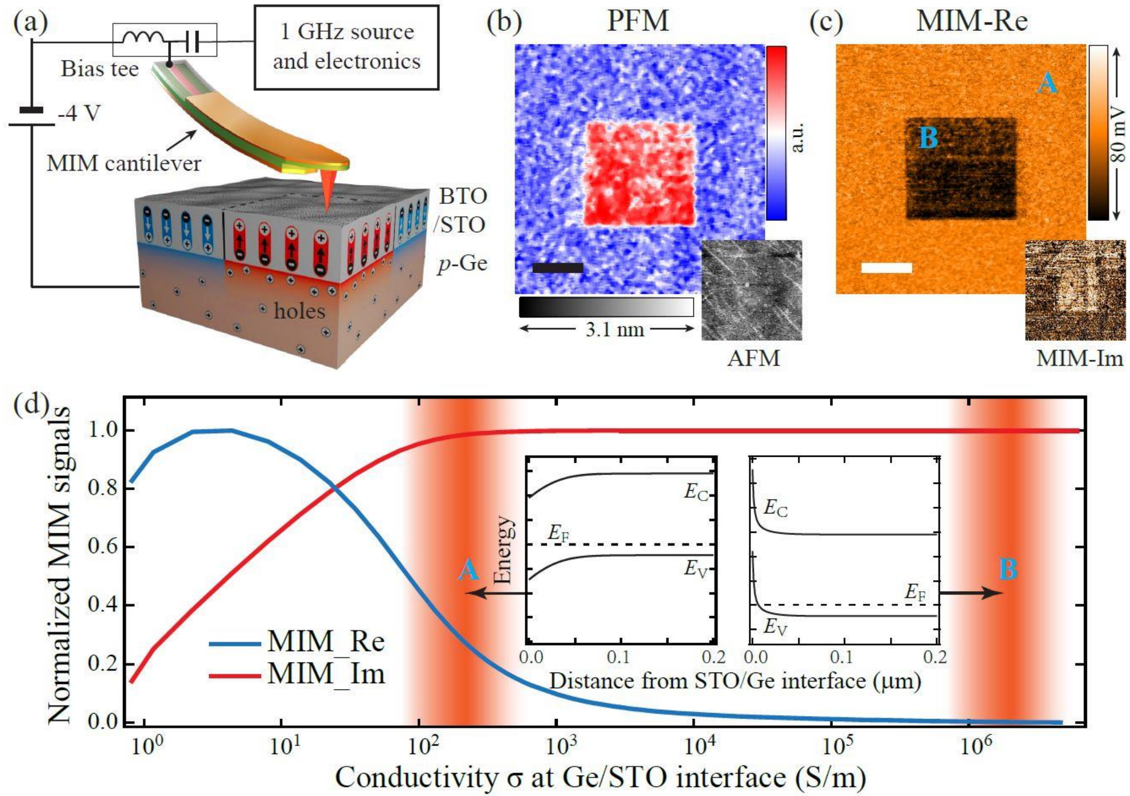

Figure 5.14. a) Schematic diagram illustrating the measurement setup and configuration of samples. A negative-biased conductive scanning probe makes downward to upward switching in ferroelectric polarization of BTO layer, which modulates hole density at the BTO/p-Ge interface. b) PFM, AFM (bottom right corner in b), c) MIM real part and MIM imaginary part (bottom right corner in c) images acquired after writing a 20 × 20 mm^2 square by applying -4 V DC bias on the tip (Scale bars: 10 mm). d) Simulated MIM-Re (blue line) and MIM-Im (red line) signals as a function of conductivity at the BTO/Ge interface. Left and right insets, respectively, show band diagrams of Ge in regions A and B in panel c).

5.3.3 Conclusion

In conclusion, the ferroelectric field effect is clearly demonstrated for highly crystalline *c*-axis-oriented $BaTiO_3$, epitaxially grown on Ge(100) substrates using molecular beam epitaxy via a thin (20 Å) $SrTiO_3$ buffer layer. The ferroelectric properties of the BTO layer and its effects on the underlying Ge are confirmed using piezoelectric force microscopy and microwave impedance microscopy. Results of electron microscopy and piezoelectric force microscopy in regard to the microscopic nature of the effect can be well understood within the atomistic picture provided by first principles theory. Our results open the possibility of realizing a ferroelectric FET, leading to new non-volatile memories and low-power devices.

Chapter 6: Switchable conductivity at the $BaTiO_3$/$SrTiO_3$ interface[§]

We investigate theoretically the interface between a ferroelectric $BaTiO_3$ film and a non-polar insulating $SrTiO_3$ substrate. We find that thin $BaTiO_3$ (under 5 nm) can stabilize a non-polarized state, and an additional metastable polarized state. While the non-polarized state is insulating, for the polarized heterostructure, we discover the existence of two-dimensional charge carrier gases. In this case, the heterostructure undergoes an electronic reconstruction in order to prevent the polar catastrophe. The two-dimensional gases, formed as a result, screen the polarization, leading to a substantially reduced potential drop across the ferroelectric film. We emphasize that the two-dimensional electron and hole gases are created by the polarization of the sample, and are not due to polar nature of the material or to doping.

6.1 Introduction

The astounding discovery of a conducting layer at the interface of two large band gap, insulating oxides, $LaAlO_3$ (LAO) and $SrTiO_3$ (STO), by Ohtomo and Hwang[47] has led to an obvious question: how can the interface of two insulators be conductive? The answer is widely believed to be a phenomenon known as the polar catastrophe.[253–255] Left uncompensated, a large electric field is built-up in a polar oxide such as LAO; the alternating positively charged LaO and negatively charged AlO_2 layers lead to a ramping up of the electrostatic potential that grows without limit. Due to the large cost of the corresponding internal field, and to avoid dielectric breakdown, the heterostructure must do something to counter the polarization catastrophe. In many cases, atomic reconstruction is the solution, where diffusion of atoms or vacancies helps to reduce or eliminate the internal field.[46,48,88–90,189] Another way to avoid the polar catastrophe is electronic reconstruction, where the electronic charge migrates to the interface to eliminate the field.

[§] The work described in this chapter has been published as “Switchable conductivity at the ferroelectric interface: nonpolar oxides”, K.D. Fredrickson and A.A. Demkov, Phys. Rev. B **91**, 115126 (2015). K.D.F. designed and performed the first-principles calculations. A.A.D. contributed to the theoretical calculations and the overall design of the work.

This interfacial charge density resulting from electronic reconstruction is often referred to as a two-dimensional electron gas (2DEG), due to its localization at the interface between LAO and STO.[46,48–51] The thickness of LAO is also an important factor; there is a critical thickness of LAO where the 2DEG forms and the interface undergoes an insulator-metal transition, with a critical thickness of four unit cells (UC) of LAO[256] for an LAO/STO structure and six UC's in LAO/STO multilayer structures.[257] It was also found that even when the LAO thickness is less than the critical thickness of 4 UC, the interface could still be made conducting by applying a gate voltage.[256] Theory has suggested that some of the electrons at the interface are localized in sub-bands and do not contribute to the conductivity,[258] explaining why experimentally the charge density measured is much lower than the expected 0.5e per unit cell.[88,89,91,256] Compressive strain has been shown to decrease the conductivity of the 2DEG and increase the critical LAO thickness for formation of the 2DEG; however, tensile strain was shown to result in an insulating interface.[259]

Experiment and theory show that the 2DEG at the oxide/oxide interface has many exotic features. It can be paramagnetic, ferromagnetic or even superconducting,[49,50,92,260] with strong Rashba splitting leading to a controllable magnetic moment.[261–263] Although the 2DEG is usually thought of as localized at the interface, the spatial extent of the gas has been found to vary from a depth of a few nanometers to hundreds of micrometers.[264] The varying spread of the 2DEG is due to many factors, including oxygen vacancy concentration,[264] temperature of the system,[89] charge density of the gas,[265] amount of cationic exchange,[266] and ionic relaxation at the interface.[98,267,268]

It has been demonstrated that various modifications of the LAO/STO heterostructure also lead to a variety of interesting effects. Arras *et al.* showed that adding a variety of metallic layers on LAO leads to an increase or decrease of the field in LAO, and in one case, even creating a spin-polarized 2DEG at the interface.[269] Although most of the experiments were done on LAO grown on bulk STO, there have also been reports of the 2DEG found in LAO/STO heterostructures deposited on Si, paving the way for semiconducting devices utilizing the properties of the oxide 2DEG.[270] Levy and co-authors

used atomic force microscope lithography to induce a reversible metal/insulator transition of the interface.[271,272]

Although the discussion of 2DEGs is dominated by the STO/LAO interface, there are reports of 2DEGs being formed in a variety of other oxide materials. Even in pure STO, replacing a SrO layer with a rare earth-oxide (RO) ML leads to an additional donated electron in the system. Depending on the rare earth atom substituted, the ML can be either insulating, or a 2DEG may form.[273] Inserting sub-monolayer doping levels of La in pure STO induces a change from 3D to 2D conducting states, depending on the concentration of the La dopant levels.[274] 2DEGs have also been seen in heterostructures containing neither STO or LAO; theoretically, a $YMnO_3$/GaN heterostructure was shown to have a spin-dependent conduction band offset due to a spin-polarized metallic interface.[275] The combination of two polar materials ($Mg_xZn_{1-x}O$/ZnO) led to a 2DEG at the interface due to charge being driven there by the polarization of the materials; however, these materials are not switchable.[276]

There is evidence that ferroelectrics may allow for the creation of surface charge. In the bulk of a ferroelectric, the material cannot be metallic, due to screening of the polarization due to conduction electrons.[277] However, there is experimental and theoretical evidence of the formation of a two-dimensional conducting layer on the surface of clean ferroelectrics, which is attributed to the uncompensated surface charge due to the ferroelectric nature of the material.[278–282] A prior study has shown that a $PbZr_{0.2}Ti_{0.8}O_3$-$LaNiO_3$ heterostructure allows a switchable conduction layer at the interface, although in this case the substrate is already metallic.[283] In a recent theoretical study, Niranjan *et al.* have shown that the charge density at a polar ferroelectric $KNbO_3$(KNO)/STO interface can change depending on the polarization state of the ferroelectric, due to variation in electronic screening of the polarization.[284] While the charge density of the 2DEG at the KNO/STO interface can be modified by switching the polarization of KNO (provided it is a single domain film), the origin of the 2DEG is in the polar nature of KNO, which is clear as the 2DEG is still seen even when KNO is in a paraelectric state with no polarization present. In other words, although the 2DEG responds to the change in the polarization of

the sample, the polarization does not *create* the 2DEG. In fact, one thing that all prior work on 2DEGs at the interface of insulating oxides has in common is that the creation of the 2DEG is due to either a) the polar nature of one of the materials, or b) the addition of dopants to introduce extra electrons. In this paper, we propose that a 2DEG can be created at the interface of two insulating nonpolar oxides, one of which is ferroelectric. Crucially, neither of the materials is polar! That is, the 2DEG is *created* by the polarization of the system, which is seen by the fact that in the nonpolarized, paraelectric state, the entire system is insulating. Our goal is to study an interface of a stoichiometrically non-polar ferroelectric $BaTiO_3$ (BTO) with a "normal" band insulating oxide STO to determine the feasibility of creating a 2DEG purely via spontaneous polarization. We choose STO as it is commonly used as a substrate for epitaxial BTO growth;[285–287] the STO/BTO system is itself interesting due to theoretical reports of increased BTO polarization[41] and giant dielectric response.[42]

The rest of the chapter is organized as follows. We describe the computational methods used in this work in Section 6.2. In Section 6.3, we discuss the structure and polarization stability. The appearance of a two dimensional conducting state at both the BTO/STO interface and at the BTO surface is discussed in Section 6.4. We summarize our results in Section 6.5.

6.2 Computational Details

All calculations are done using density functional theory (DFT) within the local density approximation (LDA) and plane augmented-wave pseudopotentials as implemented in the VASP code.[65,66,131–134] We employ the Perdew-Zunger form of the exchange-correlation potential.[135] We use the valence configuration $3p^6 4s^2 3d^2$ for Ti, $5s^2 5p^6 6s^2$ for Ba, $4s^2 4p^6 5s^2$ for Sr, and $2s^2 2p^4$ for O. We use a 650 eV kinetic energy cutoff for all calculations. For the Brillouin zone integration, we use the following Monkhorst-Pack[136] k-point meshes: 8×8×8 for bulk BTO, 8×8×8 for bulk STO and 8×8×1 for the BTO/STO superstructures. Bulk BTO and STO are fully optimized, and all structures are optimized with respect to the ionic positions until the forces on all atoms are less than 10

meV/Å. For the BTO/STO superstructures we optimize the ionic positions until the forces are less than 30 meV. The energy is converged to 10^{-3} meV/cell. The relaxation is not constrained by symmetry.

We restrict our consideration to the cubic phase of STO, as this is the phase most commonly used in experimental growth. We calculate the lattice constant of STO to be 3.861 Å, in good agreement with previously reported experimental value of 3.905 Å[137] and a theoretical value of 3.918 Å.[288] At high temperature BTO is cubic, but at 393 K it transforms to a tetragonal ferroelectric phase. As we are interested in the room temperature properties of BTO, we restrict ourselves to studying the tetragonal phase. Our calculated lattice constant *a* of 3.960 Å and c/a ratio of 1.005 compare favorably with the experimental values of a = 3.990 Å and c/a = 1.011,[166] and with previously reported theoretical values of a = 4.00 Å and c/a = 1.010.[167] As BTO has a larger lattice constant than STO, setting the lateral size of BTO to be that of STO results in a compressive strain of 2.5%.

To investigate the BTO/STO junction and comply with the periodic boundary conditions, we use a 6 unit cell thick STO layer representing a substrate, with two 10-unit-cell-thick BTO slabs attached on either side, each terminated with a TiO_2 layer; 15 Å of vacuum separates the slabs. We note that our BTO is ~4 nm thick, above the critical thickness for ferroelectricity of ~2.4 nm shown previously in literature for LDA.[36] The interface between the two materials is represented by a BaO/TiO_2/SrO layer sequence (Figure 6.1). We allow all of the BTO and the first unit cell of STO on either side to relax; we freeze the central UC of STO to mimic the experimental conditions of a bulk substrate. To make sure that the vacuum is thick enough for our calculations, we examine the plane-averaged electrostatic potential and verify that the potential of the system reaches a constant value in the vacuum region.

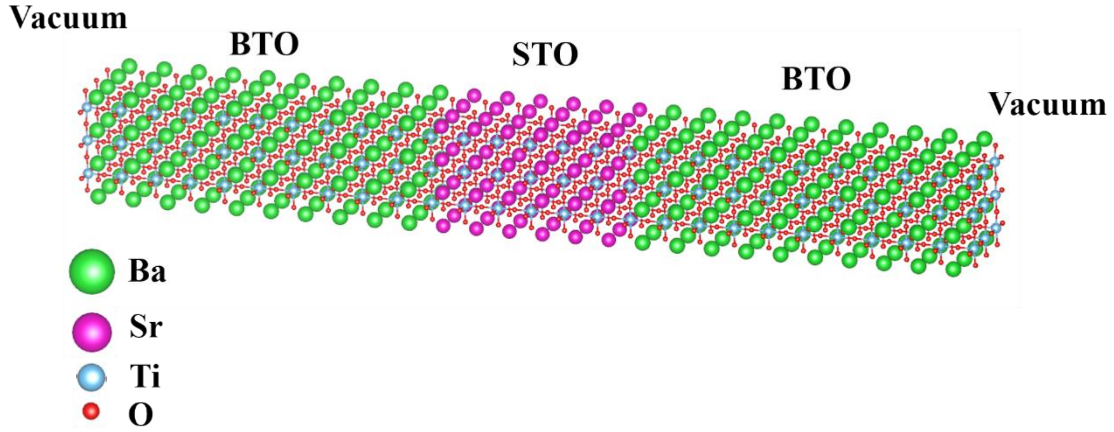

Figure 6.1. The simulation cell, showing the Vacuum/BTO/STO/BTO/Vacuum slab.

6.3 Polarization Stability

To test the effect of polarization on the STO/BTO superstructure, we consider six different polarization configurations: no polarization (which we refer to as P_0), polarization with Ti atom moving away from the surface and toward the interface (which we refer to as P_+), and polarization with Ti moving toward the surface and away from the interface; we do all three cases with TiO_2-terminated and BaO-terminated BTO, for a total of six cases. The polarization of a unit cell of either BTO or STO is given by

$$P_{\beta}^{*} = \frac{1}{\Omega} \sum_{\kappa} \int Z_{\kappa,\alpha\beta}^{*} d\tau_{\kappa,\alpha} \tag{6.1}$$

where P is the polarization, Ω is the volume of the unit cell, τ is the displacement of the ion, κ indexes the ions in the unit cell, α, β are Cartesian directions, and Z* is the Born effective charge tensor given by

$$Z_{\kappa,\alpha\beta}^{*} = \Omega \frac{dP_{\beta}}{d\tau_{\kappa,\alpha}} \tag{6.2}$$

We calculate Z* using density functional perturbation theory.[81,82] As the change in polarization is highly linear with respect to the ionic displacement, as a very good approximation,[83] we calculate P by

$$P_\beta = \frac{1}{\Omega} \sum_\kappa Z^*_{\kappa,\alpha\beta} \tau_{\kappa,\alpha} \tag{6.3}$$

In bulk BTO, we find P to lie exclusively in the [001] direction with a value of 22.9 μC/cm^2, in reasonable agreement with previously reported experimental value of 27 μC/cm^2,[289] and a theoretical value of 30 μC/cm^2.[290] The rumpling, given by the relative displacement of the Ti and O ions, is calculated to be 0.096 Å in bulk. In the heterostructure, the calculation of polarization is somewhat less straightforward; due to relaxation effects, the unit cell volume is not constant for each layer of BTO or STO. The lateral strain is obviously the same for each unit cell of the same material as it is set by the periodic boundary conditions of the simulation cell, but the height (length in the c-direction) of each cell is allowed to vary and does relax into the vacuum. We define a cell be from one AO plane to the next AO plane (A=Ba,Sr). We calculate the rumpling as the difference in z-direction between Ti and O atoms in the TiO_2 plane and the difference in z-direction between Ba (Sr) and O in the BaO (SrO) planes. We use the bulk values of Born effective charges of STO and BTO for the heterostructures; for the TiO_2 layer at the interface, we use the average of the Ti and O Born effective charges of BTO and STO.

First, we will examine the TiO_2-terminated structures. We find that the case of the polarization pointing toward the surface of BTO is unstable, and the system relaxes to the un-polarized paraelectric case. This appears to be due to the strong tendency of the surface TiO_2 plane to relax away from the vacuum (Ti atoms "sink" into the crystal).[291,292] The effect of the surface can be overcome if a much thicker BTO layer is used. However, in our calculation, a 180° domain wall would need to be considered, which in a previous work we calculated to have an energy 0.11 J/m^2.[242] The full examination of this problem is beyond the intended scope of this chapter. The rumpling and polarization are shown in Figure 6.2 for both stable structures, one where the polarization points away from the BTO surface and towards the BTO/STO interface (the P_+ case), and another where the BTO is

un-polarized (the paraelectric P_0 case). We see that the P_+ case retains just under half the polarization and rumpling of the bulk. We also find that the P_0 configuration is lower in energy than the P_+ by 20 meV per cell at this thickness. Upon examining the BaO-terminated heterostructures, we see that all three polarization states relax to the un-polarized, paraelectric state, giving us a total of three unique polarization states; TiO_2-terminated, polarized away from the surface (P_+); TiO_2-terminated, un-polarized (P_0); and BaO-terminated, un-polarized. Although we have shown that it is only possible to obtain two states for the heterostructure with the TiO_2-terminated surface (polarized away from the surface, or unpolarized),the addition of a metallic capping layer may allow the BTO to polarize away from the interface; indeed, our prior calculations have shown that 5 ML of Pt as a capping layer for 10 UC of BTO is enough to stabilize ferroelectricity.[242] The addition of a metallic capping layer could also protect the surface from unwanted adsorption by foreign material.

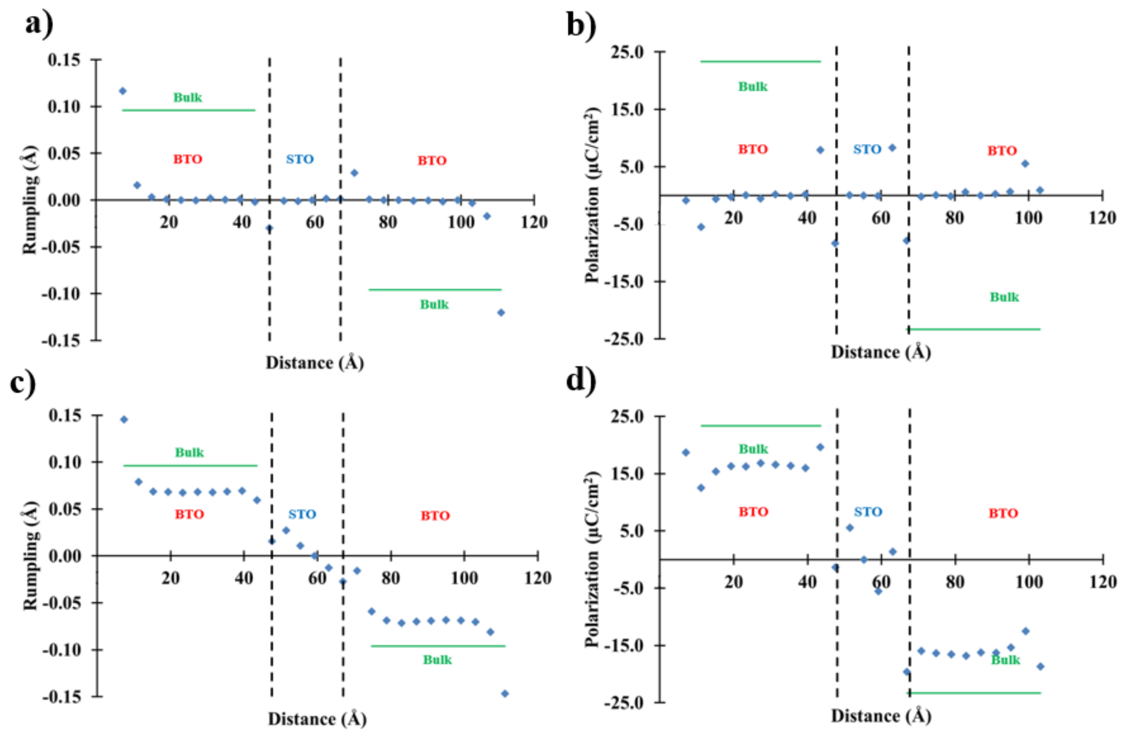

Figure 6.2. The a) rumpling and b) polarization for the paraelectric P_0 structure, and the c) rumpling and d) polarization for the polarized P_+ structure.

We also examine the Ti-O bond lengths of the interface for the three heterostructures; for reference, the bulk STO bond Ti-O bond length is 1.93 Å, and in BTO there are two Ti-O bond lengths in the c-direction due to the rumpling of the TiO_2, with 1.87 Å being the shorter bond length and 2.11 Å being the longer bond length. Upon examining the Ti-O bond lengths at the interface, we see that in the P_0 case, the Ti-O bond length for the O in the BaO layer is 2.03 Å, and the Ti-O bond length to the O in the SrO layer is 1.93 Å; the in-plane Ti-O bond length is 1.93 Å. The Ti-O bond length for the SrO layer is the same as bulk STO, and the Ti-O bond in the BaO layer is between the that of STO and the long bond length in BTO. The difference in bond length for the BaO layer is due to the strain of BTO being lattice matched to STO. In the P_+ heterostructure, the Ti-O bond length for the O in the BaO layer is 2.09 Å, and the Ti-O bond length to the O in the SrO layer is 1.96 Å; the in-plane Ti-O bond length is 1.93 Å. The differing bond lengths are due the small but nonzero rumpling of the TiO_2 layer. The bond lengths for the BaO-terminated heterostructure are essentially the same as those of the P_0 case.

We also examine the plane-averaged electrostatic potential of the P_+ and P_0 configurations and compare them in Figure 6.3. One can see that there is a noticeable change in potential in the polarized portion of BTO, as is expected; however, we see that the potential is also noticeably different in the STO. We note that the difference in potential energy at the center of the slab is approximately 0.81 eV, with the P_0 case being higher. This suggests that on an insulating substrate, the change in potential in the substrate should be measureable between a polarized and non-polarized film. The change in potential is due to the electric field resulting from the polarization of BTO. Averaging over BTO, we get a polarization of 16.45 μC/cm^2; assuming a constant polarization P in BTO of this value and relative permittivity of free space ($\varepsilon_r = 1$), the magnitude of the electric field E is

$$E_{BTO} = \frac{P}{\varepsilon_r \varepsilon_0} \tag{6.4}$$

which we calculate to be 1.89 V/Å, and would correspond to a potential energy drop of ~ 80 V. When we inspect the field in BTO from the calculation, we see that the field is actually only 0.02 V/Å, roughly 1% of the field that we obtained under these assumptions.

The reason for this discrepancy in field and potential difference will be discussed in the next section.

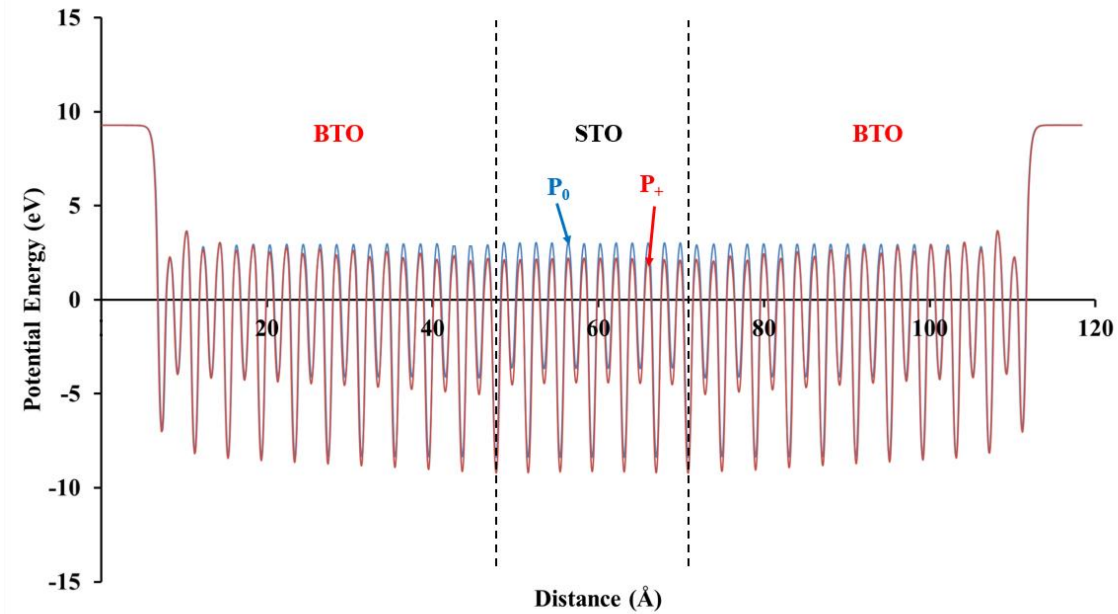

Figure 6.3. The comparison of plane-averaged electron electrostatic potential between P_0 and P_+. The difference in potential due to the polarization in the P_+ case can be clearly seen.

6.3 Two-Dimensional Electron and Hole Gases

Further insight can be obtained from the analysis of the electronic structure of our heterostructures. We plot the layer projected density of states (DOS) of the TiO_2 layers in Figure 6.4. In Figure 6.4 we present the result for configuration P_0. For the surface TiO_2 layer, the DOS extends into the gap, due to the higher energy surface states at the TiO_2-terminated surface.[292] The rest of the TiO_2 layers are similar to that of bulk BTO. Also note that there is no large change in the DOS at the BTO/STO interface, and the entire heterostructure is insulating. In the non-polarized case, there is no fundamental difference between this heterostructure and a relatively thick BTO or STO slab. The BaO-terminated case looks essentially the same as the P_0 case.

When examining the P_+ configuration (Figure 6.4 b)), however, there are important differences. First, there is the previously mentioned electric field across the BTO layer, which is expected for a polarized slab of BTO. More importantly, examining the STO/BTO interface, we see that the Fermi energy is now in the conduction band, indicating that the interface is conducting. Moving towards vacuum, away from the interface, the conduction band rises due to the internal field of BTO, and the Fermi energy drops below the conduction band edge, showing that the bulk of BTO is insulating. Finally, reaching the surface of BTO, we see that the Fermi energy is now in the valence band, making the surface also conducting. There is charge density near the interface that does not extend into the BTO bulk. This suggests that this conducting interfacial state has two-dimensional character, i.e. a 2DEG. Also, as the Fermi energy is in the surface layer of BTO, there is also a two-dimensional hole gas (2DHG) at the surface. Figure 6.5 shows a contour plot of the DOS that shows the 2DEG and 2DHG. As we can see, since neither of the materials are polar, there must be hole states present somewhere in the material, since the paraelectric heterostructure is charge neutral and insulating.

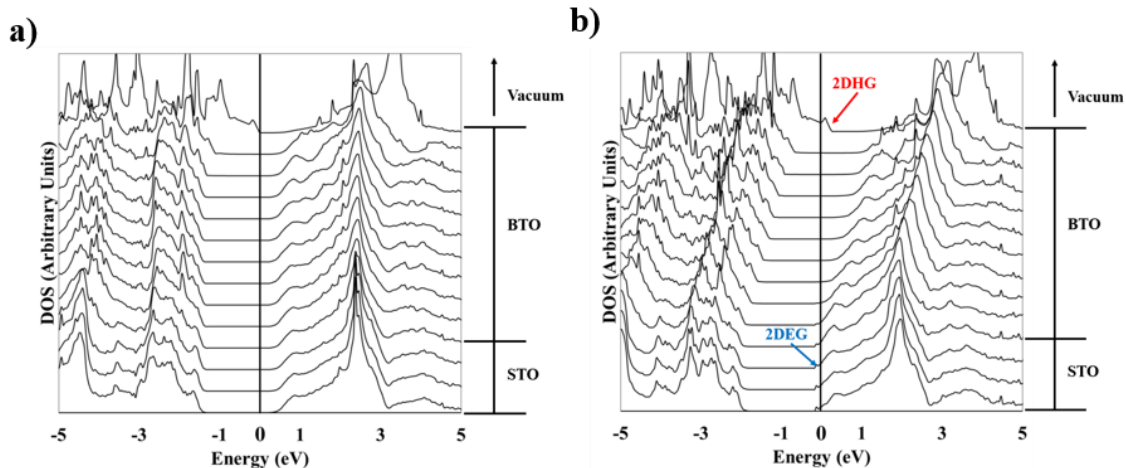

Figure 6.4. The layer-decomposed DOS for a) P0 and b) P+. The slab is mirrored on the other side, so only a half of the DOS is shown.

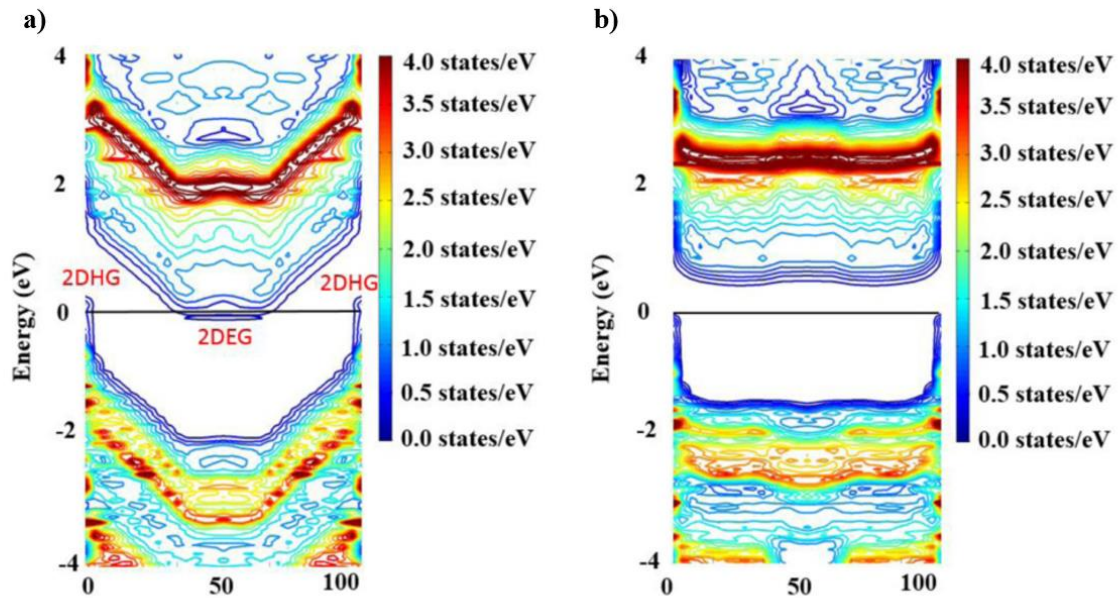

Figure 6.5. The DOS of the system projected on TiO_2 planes in the energy vs distance plane for the a) polarized and b) paraelectric BTO/STO heterostructure. In the polarized case, the 2DEG and the 2DHG can be clearly seen.

In Figure 6.6, we examine the projected DOS at the surface, interface, and deep in the STO bulk. We see that the 2DHG at the surface of BTO resides entirely on oxygen p_x and p_y states. The effect of the surface is to raise the energies of the p_x and p_y states while leaving the p_z states unaffected, consistent with prior calculations of the BTO surface.[293] The Ti d-states do not strongly contribute to this surface state. At both the BTO/STO interface and in the STO bulk, we see that the 2DEG is comprised of mostly Ti d_{yz} and d_{xz} states, with a small portion of d_{xy} states; the e_g states and O p-states do not contribute. This is quite different from the LAO/STO interface, where only the d_{xy} orbital is occupied, and forms an in-gap state.[50]

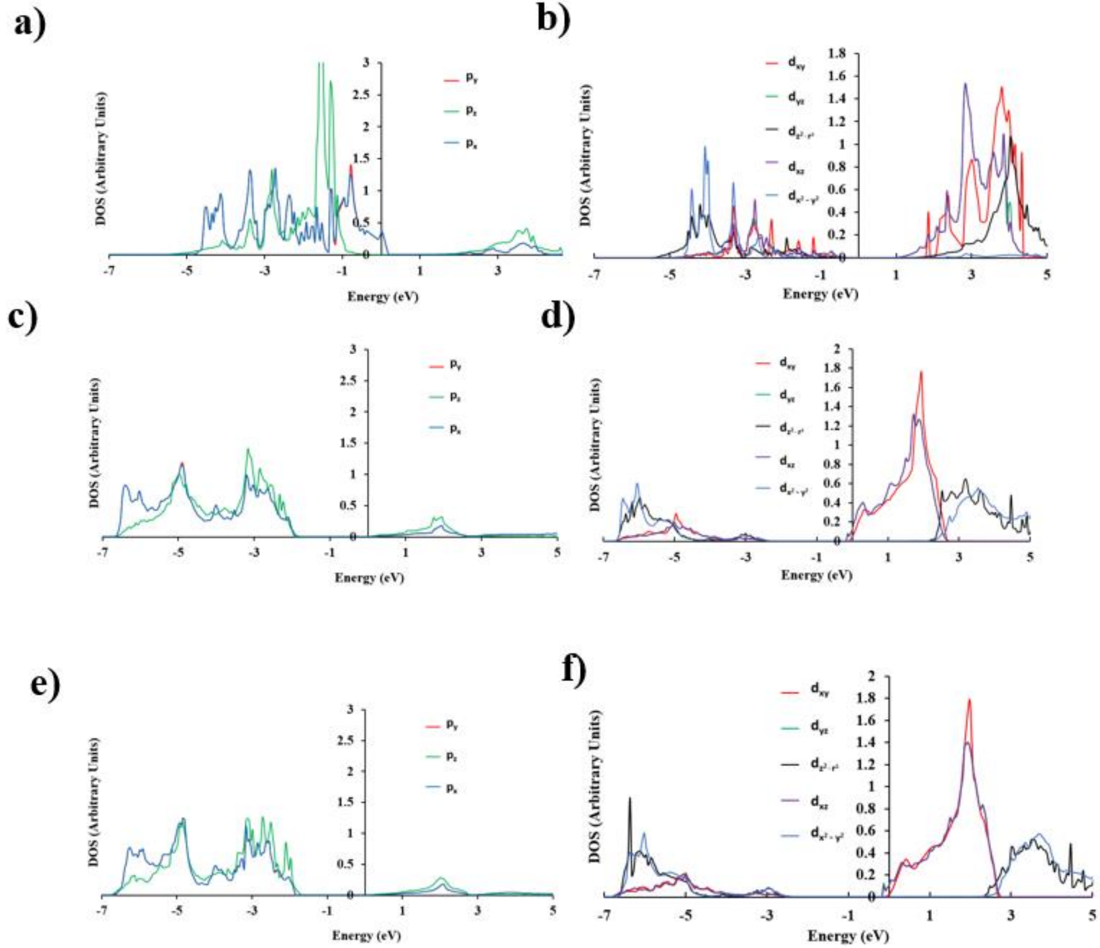

Figure 6.6. Projected DOS for selected TiO2 planes for the polarized BTO/STO heterostructure. a) p-states and b) d-states of the BTO surface, c) p-states and d) d-states of the BTO/STO interface, and e) p-states and f) d-states of the center of the STO bulk. The 2DEG can be seen to be of almost all d-character, and the 2DHG can be seen to be almost entirely p-character.

The difference in occupation is due to the symmetry-breaking nature of the interface, and the rumpling of the TiO_2 planes in STO, though the splitting of the t_{2g} states is small (this splitting is also seen in the nonpolarized heterostructure, although the t_{2g} states are unoccupied). The charge density at the Fermi level of the heterostructure is shown in Figure 6.7. In Figure 6.7 a), we see that the holes are localized completely at the BTO surface, on the O atoms (if exposed to air, this 2DHG might be compensated by adsorbed species, therefore in practice one may need to consider a capping layer). The p character

of the charge density is clearly visible. In Figure 6.7 b), we see that the electron density is located over several layers of TiO_2, concentrated at the interface, and dying rapidly into STO and BTO; it is located almost entirely on the Ti atoms**,** in agreement with our analysis from the density of states. As the hole states are localized solely at the BTO surface, and the electron states are mainly at the STO/BTO interface, decaying rapidly going into both STO and BTO, we call these states two-dimensional.

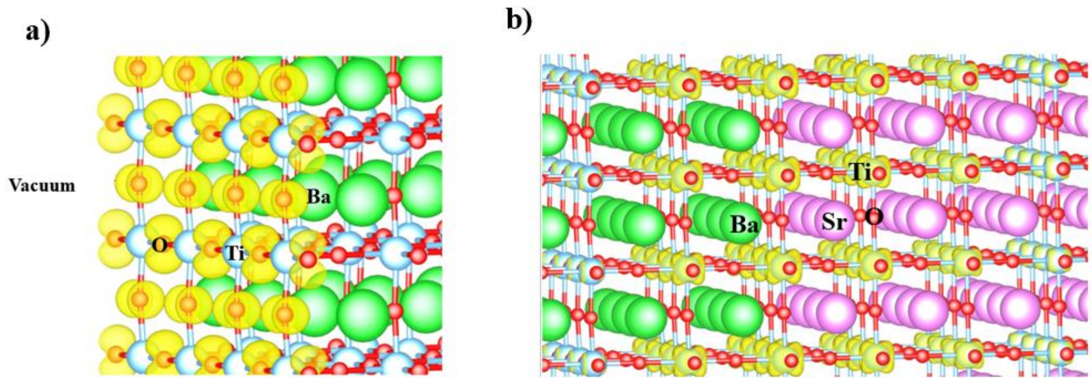

Figure 6.7. The charge density at the Fermi level. The pictured isosurface is for a charge density of 0.1203 e/Å^3. a) The hole gas at the surface of BTO. Note the p-character of the charge density. b) The electron gas at the STO/BTO interface. Note the d-character of the charge distribution.

One important issue is that, in LDA, both BTO and STO have an incorrect band gap (in experiment the band gap is ~3.2 eV for both rather than ~1.7 eV in LDA). Our calculations show that using the LDA+U[228] method in bulk BTO, with U on the Ti *d* states, bulk BTO is paraelectric, even in the tetragonal phase. This means that using relaxing the ions using LDA+U in the system is not possible, as we will be unable to achieve a ferroelectric state. However, we did a calculation with relaxed ionic positions with LDA, and we used LDA+U (U = 8.0 eV) to see its effect on the electronic structure. With LDA+U on bulk BTO, the gap is increased to ~2.8 eV, and upon examining the DOS for the polarized heterostructure, the 2DEG dies much more rapidly than in LDA, with the central layer of TiO_2 almost insulating (the paraelectric BTO/STO structure is essentially unchanged, except for the larger band gaps). This is to be expected, due to the scaling of shorter decay length with larger band gaps.[294]

Now, we discuss why the electric field in BTO is smaller than anticipated. The effect of the 2DHG and 2DEG is to impose an extra electric field on the BTO to help screen the large field caused by the polarization of the sample (here we assume that the field caused by the 2D gases almost entirely compensates the internal field caused by the polarization, see Figure 6.8). The electric field caused by the 2DHG and 2DEG points in the opposite direction to that of the field due to the polarization of BTO. We calculate the charge of the 2DHG by integrating the DOS for the surface layer of TiO_2 and find the total charge to be 0.12 e; the charge of the 2DEG must be opposite in value due to the conservation of charge in the system. We calculate the surface charge density of each gas to be 12.5 $\mu C/cm^2$. Therefore, the true electric field of the system is given by the difference between the two polarizations, which is 0.45 V/Å. Finally, we expect the field to be diminished in BTO due to its large dielectric constant. If we take the expected field and divide it by the calculated field, we obtain a relative dielectric constant of 21.0. Although this number is small in comparison to that of bulk BTO (1500 at 1 KHz),[295] experiment has shown that thin films have a much smaller relative dielectric constant (as low as 93 for 108 nm film).[296] As our film is even thinner (~ 4 nm), we believe that a value of 21.0 is a reasonable estimate for the dielectric constant of our sample.

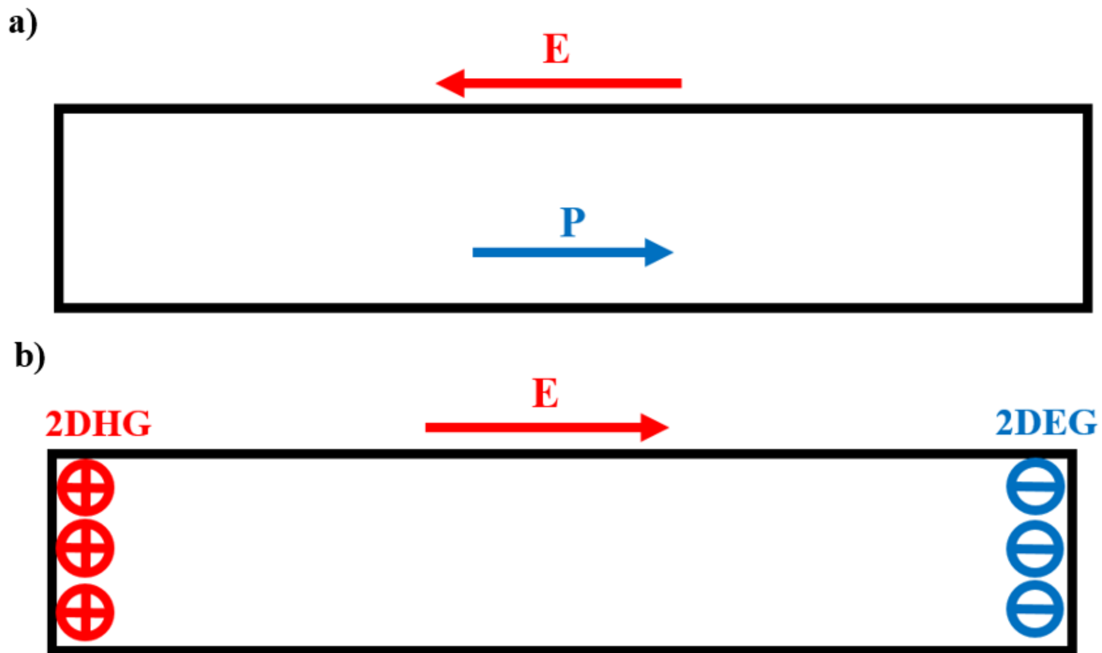

Figure 6.8. a) The electric field caused by the polarization of BTO. b) The electric field caused by the 2DEG and 2DHG. Note that the gases cause a field that opposes the field caused by the polarization of the sample.

There is another way to view the formation of the two-dimensional gases in our system. Electrostatic boundary conditions tell us that the free surface charge density σ_f of an interface is due to the difference in the normal component of the electric displacement **D** between two materials:

$$D_{1,n} - D_{2,n} = \sigma_f \tag{6.5}$$

As there is no external field, we see that σ_f is due to the difference in polarization between BTO and STO. We compute the average polarization in STO to be 2.0 μC/cm^2, and thus $_f$ is equal to 14.4 μC/cm^2, in good agreement with 12.5 μC/cm^2 of the 2DEG and 2DHG found from the integrated charge density (we can see that since the polarization is not constant in BTO and STO, we do not expect this approximation to be exact). Thus, we see that the presence of the gases can also be explained with an electrostatic argument.

The mechanism for the formation of the conducting layers is similar to that at the LAO/STO interface. The internal field due to the polarization in BTO increases with

increasing BTO thickness. There is an electronic reconstruction caused by the migration of the electrons in the high-energy surface state to the BTO/STO interface to avoid the polar catastrophe, similarly to that at the LAO/STO interface. In our calculation, however, the 2DEG is comprised of all t_{2g} states, in contrast with the LAO/STO interface that has a 2DEG only in the d_{xy} orbital. In addition, while in LAO there is no mechanism to "turn-off" the field due to the intrinsically polar layers, in BTO the field can be removed by switching to a non-polar state, where the TiO_2 layers are flat and there is no field. In this case, there is no polar catastrophe and the electronic reconstruction is unnecessary, leading to an insulating interface, which is to be expected for a clean interface between two non-polar oxides. This gives us control over having a conducting or insulating interface and surface by switching between two stable polarization states. A possible way to check this experimentally would be to measure interface conductivity of a BTO/STO heterostructure above and below the critical temperature T_c of BTO.

6.5 Conclusion

Using first-principles calculations, we investigate the interface between a ferroelectric BTO film and a non-polar insulating STO substrate. We find that thin TiO_2-terminated BTO, under 5 nm, can stabilize two different polarization states; one is a paraelectric state, and the other is a polarized state where BTO is polarized toward the BTO/STO interface. There is a potential difference of 0.81 eV in STO between the non-polarized and the polarized BTO heterostructures caused by the drop in potential from the electric field created by the BTO polarization. The non-polarized heterostructure is insulating throughout and no two-dimensional conductive states are found. In the polarized heterostructure; however, we discovered the existence of a 2DEG at the interface between BTO and STO, and the existence of a 2DHG at the surface of BTO. The polarized heterostructure undergoes an electronic reconstruction in order prevent the polar catastrophe, which explains the appearance of both the 2DEG and 2DHG. The two-dimensional gases cause an additional electric field in BTO that opposes the field caused by the polarization, leading to a substantially reduced potential drop. We calculate the

relative dielectric constant of the thin BTO film to be 21.0. We emphasize that the creation of this 2DEG at an insulating oxide interface has been shown to be created by the polarization of the sample, and not due to polar materials or doping.

References

[1] R. Roy, *Crystal Chemistry of Non-Metallic Materials* (Springer-Verlag, Berlin, 1974).

[2] D.G. Schlom, L.Q. Chen, X. Pan, A. Schmehl, and M.A. Zurbuchen, J. Am. Ceram. Soc. **91**, 2429 (2008).

[3] K.A. Müller and H. Burkard, Phys. Rev. B **19**, 3593 (1979).

[4] C.H. Ahn, K.M. Rabe, and J.M. Triscone, *Physics of Ferroelectrics* (Springer-Verlag, Berlin, 2007).

[5] S.-W. Cheong and M. Mostovoy, Nat. Mater. **6**, 13 (2007).

[6] P. Schiffer, A.P. Ramirez, W. Bao, and S.-W. Cheong, Phys. Rev. Lett. **75**, 3336 (1995).

[7] M. Imada, A. Fujimori, and Y. Tokura, Rev. Mod. Phys. **70**, 1039 (1998).

[8] M. Johnsson and P. Lemmens, arXiv:cond-mat/0506606.

[9] K.M. Rabe and P. Ghosez, *Ferroelectrics* (Springer-Verlag, Berlin, 2007).

[10] N.A. Benedek and C.J. Fennie, J. Phys. Chem. C **117**, 13339 (2013).

[11] P.M. Woodward, Acta Crystallogr. Sect. B Struct. Sci. **53**, 44 (1997).

[12] M.W. Lufaso and P.M. Woodward, Acta Crystallogr. Sect. B Struct. Sci. **57**, 725 (2001).

[13] R. Mara, G. Sutherland, and H. Tyrell, Phys. Rev. **96**, 801 (1954).

[14] K. Van Benthem, C. Elsässer, and R.H. French, J. Appl. Phys. **90**, 6156 (2001).

[15] J.M. Pond, S.W. Kirchoefer, W. Chang, J.S. Horwitz, and D.B. Chrisey, Integr. Ferroelectr. **22**, 317 (1998).

[16] S. Abel, T. Stöferle, C. Marchiori, C. Rossel, M. Rossell, R. Erni, D. Caimi, M. Sousa, A. Chelnokov, B. Offrein, and J. Fompeyrine, Nat. Commun. **4**, 1671 (2013).

[17] P. Ponath, K. Fredrickson, A.B. Posadas, Y. Ren, X. Wu, R.K. Vasudevan, M. Baris Okatan, S. Jesse, T. Aoki, M.R. McCartney, D.J. Smith, S. V. Kalinin, K. Lai, and A.A. Demkov, Nat. Commun. **6**, 6067 (2015).

[18] C. Dubourdieu, J. Bruley, T.M. Arruda, A. Posadas, J. Jordan-Sweet, M.M. Frank, E. Cartier, D.J. Frank, S. V Kalinin, A.A. Demkov, and V. Narayanan, Nat. Nanotechnol. **8**, 748 (2013).

[19] A.A. Demkov and A.B. Posadas, *Integration of Functional Oxides with Semiconductors* (Springer, New York, 2014).

[20] X. Zhang, A. Demkov, H. Li, X. Hu, Y. Wei, and J. Kulik, Phys. Rev. B **68**, 125323 (2003).

[21] C. Ashman, C. Först, K. Schwarz, and P. Blöchl, Phys. Rev. B **69**, 075309 (2004).

[22] A.M. Kolpak and S. Ismail-Beigi, Phys. Rev. B **85**, 195318 (2012).

[23] A.M. Kolpak, F.J. Walker, J.W. Reiner, Y. Segal, D. Su, M.S. Sawicki, C.C. Broadbridge, Z. Zhang, Y. Zhu, C.H. Ahn, and S. Ismail-Beigi, Phys. Rev. Lett. **105**, 1 (2010).

[24] C.S. Hellberg, K.E. Andersen, H. Li, P.J. Ryan, and J.C. Woicik, Phys. Rev. Lett. **108**, 166101 (2012).

[25] K.D. Fredrickson, P. Ponath, A.B. Posadas, M.R. McCartney, T. Aoki, D.J. Smith, and A.A. Demkov, Appl. Phys. Lett. **104**, 242908 (2014).

[26] X. Hu, H. Li, Y. Liang, Y. Wei, Z. Yu, D. Marshall, J. Edwards, R. Droopad, X. Zhang, A.A. Demkov, K. Moore, and J. Kulik, Appl. Phys. Lett. **82**, 203 (2003).

[27] L. V. Goncharova, D.G. Starodub, E. Garfunkel, T. Gustafsson, V. Vaithyanathan, J. Lettieri, and D.G. Schlom, J. Appl. Phys. **100**, (2006).

[28] G. Niu, G. Saint-Girons, B. Vilquin, G. Delhaye, J.-L. Maurice, C. Botella, Y. Robach, and G. Hollinger, Appl. Phys. Lett. **95**, 062902 (2009).

[29] S.-B. Mi, C.-L. Jia, V. Vaithyanathan, L. Houben, J. Schubert, D.G. Schlom, and K. Urban, Appl. Phys. Lett. **93**, 101913 (2008).

[30] K.J. Choi, M. Biegalski, Y.L. Li, A. Sharan, J. Schubert, R. Uecker, P. Reiche, Y.B. Chen, X.Q. Pan, V. Gopalan, L.-Q. Chen, D.G. Schlom, and C.B. Eom, Science **306**, 1005 (2004).

[31] D.G. Schlom, L.-Q. Chen, C. Eom, K.M. Rabe, S.K. Streiffer, and J. Triscone, Annu. Rev. Mater. Res. **37**, 589 (2007).

[32] N. Bickel, G. Schmidt, K. Heinz, and K. Müller, Phys. Rev. Lett. **62**, 2009 (1989).

[33] V. Ravikumar, D. Wolf, and V.P. Dravid, Phys. Rev. Lett. **74**, 960 (1995).

[34] R. Herger, P.R. Willmott, O. Bunk, C.M. Schlepütz, B.D. Patterson, and B. Delley, Phys. Rev. Lett. **98**, 1 (2007).

[35] J.H. Haeni, P. Irvin, W. Chang, R. Uecker, P. Reiche, Y.L. Li, S. Choudhury, W. Tian, M.E. Hawley, B. Craigo, a K. Tagantsev, X.Q. Pan, S.K. Streiffer, L.Q. Chen, S.W. Kirchoefer, J. Levy, and D.G. Schlom, Nature **430**, 758 (2004).

[36] J. Junquera and P. Ghosez, Nature **422**, 506 (2003).

[37] P. Zubko, S. Gariglio, M. Gabay, P. Ghosez, and J.-M. Triscone, Annu. Rev. Condens. Matter Phys. **2**, 141 (2011).

[38] M. Stengel, D. Vanderbilt, and N.A. Spaldin, Nat. Mater. **8**, 392 (2009).

[39] S. Valencia, A. Crassous, L. Bocher, V. Garcia, X. Moya, R.O. Cherifi, C. Deranlot, K. Bouzehouane, S. Fusil, A. Zobelli, A. Gloter, N.D. Mathur, A. Gaupp, R. Abrudan, F. Radu, A. Barthélémy, and M. Bibes, Nat. Mater. **10**, 753 (2011).

[40] G. Radaelli, D. Petti, E. Plekhanov, I. Fina, P. Torelli, B.R. Salles, M. Cantoni, C. Rinaldi, D. Gutiérrez, G. Panaccione, M. Varela, S. Picozzi, J. Fontcuberta, and R. Bertacco, Nat. Commun. **5**, 3404 (2014).

[41] J.B. Neaton and K.M. Rabe, Appl. Phys. Lett. **82**, 1586 (2003).

[42] A.L. Roytburd, S. Zhong, and S.P. Alpay, Appl. Phys. Lett. **87**, 1 (2005).

[43] N. Sai, B. Meyer, and D. Vanderbilt, Phys. Rev. Lett. **84**, 5636 (2000).

[44] H.N. Lee, H.M. Christen, M.F. Chisholm, C.M. Rouleau, and D.H. Lowndes, Nature **433**, 395 (2005).

[45] M.P. Warusawithana, E. V Colla, J.N. Eckstein, and M.B. Weissman, Phys. Rev. Lett. **90**, 036802 (2003).

[46] H.Y. Hwang, Y. Iwasa, M. Kawasaki, B. Keimer, N. Nagaosa, and Y. Tokura, Nat. Mater. **11**, 103 (2012).

[47] A. Ohtomo and H.Y. Hwang, Nature **427**, 423 (2004).

[48] N. Nakagawa, H.Y. Hwang, and D.A. Muller, Nat. Mater. **5**, 204 (2006).

[49] R. Pentcheva and W. Pickett, Phys. Rev. B **74**, 035112 (2006).

[50] J. Lee and A.A. Demkov, Phys. Rev. B **78**, 193104 (2008).

[51] K. Janicka, J. Velev, and E. Tsymbal, Phys. Rev. Lett. **102**, 106803 (2009).

[52] K.D. Fredrickson and A.A. Demkov, Phys. Rev. B **91**, 115126 (2015).

[53] E.R. Fossum, J.I. Song, and D. V. Rossi, IEEE Trans. Electron Devices **38**, 1182 (1991).

[54] J. Zhu, H. Li, L. Zhong, P. Xiao, X. Xu, X. Yang, Z. Zhao, and J. Li, ACS Catal. **4**, 2917 (2014).

[55] I. Popescu, A. Urda, T. Yuzhakova, I.C. Marcu, J. Kovacs, and I. Sandulescu, Comptes Rendus Chim. **12**, 1072 (2009).

[56] J.L. Wang, F. Gaillard, A. Pancotti, B. Gautier, G. Niu, B. Vilquin, V. Pillard, G.L.M.P. Rodrigues, and N. Barrett, J. Phys. Chem. C **116**, 21802 (2012).

[57] J. Shin, V.B. Nascimento, G. Geneste, J. Rundgren, E.W. Plummer, B. Dkhil, S.V. Kalinin, and A.P. Baddorf, Nano Lett. **9**, 3720 (2000).

[58] F. Lin, S. Wang, F. Zheng, G. Zhou, J. Wu, B.-L. Gu, and W. Duan, Phys. Rev. B **79**, 035311 (2009).

[59] R.C. Hatch, K.D. Fredrickson, M. Choi, C. Lin, H. Seo, A.B. Posadas, and A.A. Demkov, J. Appl. Phys. **114**, 103710 (2013).

[60] P. Hohenberg and W. Kohn, Phys. Rev. **136**, B864 (1964).

[61] W. Kohn and L.J. Sham, Phys. Rev. **140**, A1133 (1965).

[62] J.C. Phillips and L. Kleinman, Phys. Rev. **116**, 287 (1959).

[63] N. Troullier and J.L. Martins, Phys. Rev. B **43**, 8861 (1991).

[64] D. Hamann, M. Schlüter, and C. Chiang, Phys. Rev. Lett. **43**, 1494 (1979).

[65] P.E. Blöchl, Phys. Rev. B **50**, 17953 (1994).

[66] G. Kresse and D. Joubert, Phys. Rev. B **59**, 1758 (1999).

[67] N.A.W. Holzwarth, G.E. Matthews, R.B. Dunning, A.R. Tackett, and Y. Zeng, Phys. Rev. B **55**, 2005 (1997).

[68] R.M. Martin, *Electronic Structure: Basic Theory and Practical Methods* (Cambridge University Press, Cambridge, 2004).

[69] L. Landau, Zh. Eskp. Teor. Fiz. **7**, 627 (1937).

[70] L. Landau, Phys. Z. Sowjun. **11**, 545 (1937).

[71] V. Ginzburg, J. Phys. USSR **10**, 107 (1946).

[72] V. Ginzburg, Zh. Eskp. Teor. Fiz. **19**, 36 (1949).

[73] A.F. Devonshire, Adv. Phys. **3**, 85 (1954).

[74] A.F. Devonshire, Philos. Mag. **40**, 1040 (1949).

[75] A.F. Devonshire, Philos. Mag. **42**, 1065 (1951).

[76] V. Fridkin and S. Ducharme, *Ferroelectricity at the Nanoscale* (Springer-Verlag Berlin Heidelberg, New York, 2014).

[77] P. Chandra and P.B. Littlewood, arXiv:cond-mat/0609347.

[78] S. Ikeda, H. Kominami, K. Koyama, and Y. Wada, J. App **62**, 3339 (1987).

[79] R. Resta, Ferroelectrics **136**, 51 (1992).

[80] D. Vanderbilt and R. King-Smith, Phys. Rev. B **48**, 4442 (1993).

[81] S. Baroni and R. Resta, Phys. Rev. B **33**, 7017 (1986).

[82] M. Gajdoš, K. Hummer, G. Kresse, J. Furthmüller, and F. Bechstedt, Phys. Rev. B **73**, 045112 (2006).

[83] R. Resta, M. Posternak, and A. Baldereschi, Phys. Rev. Lett. **70**, 1010 (1993).

[84] R. Konta, T. Ishii, H. Kato, and A. Kudo, J. Phys. Chem. B **108**, 8992 (2004).

[85] N. Zhou, K. Zhao, H. Liu, Z. Lu, H. Zhao, L. Tian, W. Liu, and S. Zhao, J. Appl. Phys. **105**, 5 (2009).

[86] D. Kan, T. Terashima, R. Kanda, A. Masuno, K. Tanaka, S. Chu, H. Kan, A. Ishizumi, Y. Kanemitsu, Y. Shimakawa, and M. Takano, Nat. Mater. **4**, 816 (2005).

[87] K. Ueno, S. Nakamura, H. Shimotani, A. Ohtomo, N. Kimura, T. Nojima, H. Aoki, Y. Iwasa, and M. Kawasaki, Nat. Mater. **7**, 855 (2008).

[88] A. Kalabukhov, R. Gunnarsson, J. Börjesson, E. Olsson, T. Claeson, and D. Winkler, Phys. Rev. B **75**, 121404 (2007).

[89] W. Siemons, G. Koster, H. Yamamoto, W. Harrison, G. Lucovsky, T. Geballe, D. Blank, and M. Beasley, Phys. Rev. Lett. **98**, 196802 (2007).

[90] G. Herranz, M. Basletić, M. Bibes, C. Carrétéro, E. Tafra, E. Jacquet, K. Bouzehouane, C. Deranlot, A. Hamzić, J.-M. Broto, A. Barthélémy, and A. Fert, Phys. Rev. Lett. **98**, 216803 (2007).

[91] A. Brinkman, M. Huijben, M. van Zalk, J. Huijben, U. Zeitler, J.C. Maan, W.G. van der Wiel, G. Rijnders, D.H.A. Blank, and H. Hilgenkamp, Nat. Mater. **6**, 493 (2007).

[92] N. Reyren, S. Thiel, A.D. Caviglia, L.F. Kourkoutis, G. Hammerl, C. Richter, C.W. Schneider, T. Kopp, A.-S. Rüetschi, D. Jaccard, M. Gabay, D.A. Muller, J.-M. Triscone, and J. Mannhart, Science **317**, 1196 (2007).

[93] D.A. Dikin, M. Mehta, C.W. Bark, C.M. Folkman, C.B. Eom, and V. Chandrasekhar, Phys. Rev. Lett. **107**, 056802 (2011).

[94] J.A. Bert, B. Kalisky, C. Bell, M. Kim, Y. Hikita, H.Y. Hwang, and K.A. Moler, Nat. Phys. **7**, 767 (2011).

[95] W.S. Choi, D.W. Jeong, S.A.A. Seo, Y.S. Lee, T.H. Kim, S.Y. Jang, H.N. Lee, and K. Myung-Whun, Phys. Rev. B **83**, 195113 (2011).

[96] A. Posadas, M. Berg, H. Seo, A. De Lozanne, A.A. Demkov, D.J. Smith, A.P. Kirk, D. Zhernokletov, and R.M. Wallace, Appl. Phys. Lett. **98**, (2011).

[97] H. Seo, A.B. Posadas, and A.A. Demkov, J. Vac. Sci. Technol. B **30**, 04E108 (2012).

[98] A. Ohtomo, D.A. Muller, J.L. Grazul, and H.Y. Hwang, Nature **419**, 378 (2002).

[99] Y. Hotta, T. Susaki, and H.Y. Hwang, Phys. Rev. Lett. **99**, 3 (2007).

[100] J. Biscaras, N. Bergeal, A. Kushwaha, T. Wolf, A. Rastogi, R.C. Budhani, and J. Lesueur, Nat. Commun. **1**, 89 (2010).

[101] S.A.A. Seo, W.S. Choi, H.N. Lee, L. Yu, K.W. Kim, C. Bernhard, and T.W. Noh, Phys. Rev. Lett. **99**, 3 (2007).

[102] J.S. Kim, S.A.A. Seo, M.F. Chisholm, R.K. Kremer, H.U. Habermeier, B. Keimer, and H.N. Lee, Phys. Rev. B **82**, 2 (2010).

[103] M. Kawasaki, K. Takahashi, T. Maeda, R. Tsuchiya, M. Shinohara, O. Ishiyuma, T. Yonezawa, M. Yoshimoto, and H. Koinuma, Science **266**, 1540 (1994).

[104] G. Koster, B.L. Kropman, G.J.H.M. Rijnders, D.H.A. Blank, and H. Rogalla, Appl. Phys. Lett. **73**, 2920 (1998).

[105] K. Szot and W. Speier, Phys. Rev. B **60**, 5909 (1999).

[106] T. Ohnishi, K. Shibuya, M. Lippmaa, D. Kobayashi, H. Kumigashira, M. Oshima, and H. Koinuma, Appl. Phys. Lett. **85**, 272 (2004).

[107] M. Kareev, S. Prosandeev, J. Liu, C. Gan, A. Kareev, J.W. Freeland, M. Xiao, and J. Chakhalian, Appl. Phys. Lett. **93**, 061909 (2008).

[108] J. Zhang, D. Doutt, T. Merz, J. Chakhalian, M. Kareev, J. Liu, and L.J. Brillson, Appl. Phys. Lett. **94**, 092904 (2009).

[109] A. Biswas, P.B. Rossen, C.H. Yang, W. Siemons, M.H. Jung, I.K. Yang, R. Ramesh, and Y.H. Jeong, Appl. Phys. Lett. **98**, 051904 (2011).

[110] R. Gunnarsson, A.S. Kalabukhov, and D. Winkler, Surf. Sci. **603**, 151 (2009).

[111] J.E. Boschker and T. Tybell, Appl. Phys. Lett. **100**, 151604 (2012).

[112] J.G. Connell, B.J. Isaac, G.B. Ekanayake, D.R. Strachan, and S.S.A. Seo, Appl. Phys. Lett. **101**, 251607 (2012).

[113] S.A. Chambers, T.C. Droubay, C. Capan, and G.Y. Sun, Surf. Sci. **606**, 554 (2012).

[114] Y. Haruyama, S. Kodaira, Y. Aiura, H. Bando, Y. Nishihara, T. Maruyama, Y. Sakiska, and H. Kato, Phys. Rev. B **53**, 8032 (1996).

[115] Y. Aiura, I. Hase, H. Bando, T. Yasue, T. Saitoh, and D.S. Dessau, Surf. Sci. **515**, 61 (2002).

[116] W. Meevasana, P.D.C. King, R.H. He, S.K. Mo, M. Hashimoto, A. Tamai, P. Songsiriritthigul, F. Baumberger, and Z.X. Shen, Nat. Mater. **10**, 114 (2011).

[117] W. Meevasana, X.J. Zhou, B. Moritz, C.C. Chen, R.H. He, S.I. Fujimori, D.H. Lu, S.K. Mo, R.G. Moore, F. Baumberger, T.P. Devereaux, D. Van Der Marel, N. Nagaosa, J. Zaanen, and Z.X. Shen, New J. Phys. **12**, 0 (2010).

[118] A.F. Santander-Syro, O. Copie, T. Kondo, F. Fortuna, S. Pailhès, R. Weht, X.G. Qiu, F. Bertran, A. Nicolaou, A. Taleb-Ibrahimi, P. Le Fèvre, G. Herranz, M. Bibes, N. Reyren, Y. Apertet, P. Lecoeur, A. Barthélémy, and M.J. Rozenberg, Nature **469**, 189 (2011).

[119] E. Frantzeskakis, J. Avila, and M.C. Asensio, Phys. Rev. B **85**, 125115 (2012).

[120] Y. Ishida, R. Eguchi, M. Matsunami, K. Horiba, M. Taguchi, A. Chainani, Y. Senba, H. Ohashi, H. Ohta, and S. Shin, Phys. Rev. Lett. **100**, 3 (2008).

[121] M. Takizawa, K. Maekawa, H. Wadati, T. Yoshida, A. Fujimori, H. Kumigashira, and M. Oshima, Phys. Rev. B **79**, 1 (2009).

[122] Y.J. Chang, A. Bostwick, Y.S. Kim, K. Horn, and E. Rotenberg, Phys. Rev. B **81**, 1 (2010).

[123] M. D'Angelo, R. Yukawa, K. Ozawa, S. Yamamoto, T. Hirahara, S. Hasegawa, M.G. Silly, F. Sirotti, and I. Matsuda, Phys. Rev. Lett. **108**, 1 (2012).

[124] R. Yukawa, S. Yamamoto, K. Ozawa, M. D'Angelo, M. Ogawa, M. Silly, F. Sirotti, and I. Matsuda, Phys. Rev. B **87**, 115314 (2013).

[125] A. Stashans and J. Chimborazo, Philos. Mag. Part B **82**, 1145 (2002).

[126] J. Chimborazo and M. Castillo, Proc. SPIE **5122**, 280 (2003).

[127] F.F.Y. Wang and K.P. Gupta, Metall. Trans. **4**, 2767 (1973).

[128] F.W. Lytle, J. Appl. Phys. **35**, 2212 (1964).

[129] T.C. Chiang, J.A. Knapp, M. Aono, and D.E. Eastman, Phys. Rev. B **21**, 3513 (1980).

[130] F.J. Himpsel, Appl. Opt. **19**, 3964 (1980).

[131] G. Kresse and J. Hafner, Phys. Rev. B **47**, 558 (1993).

[132] G. Kresse and J. Hafner, Phys. Rev. B **49**, 14251 (1994).

[133] G. Kresse and J. Furthmüller, Comput. Mater. Sci. **6**, 15 (1996).

[134] G. Kresse and J. Furthmüller, Phys. Rev. B **54**, 11169 (1996).

[135] J. Perdew and A. Zunger, Phys. Rev. B **23**, 5048 (1981).

[136] H.J. Monkhorst and J.D. Pack, Phys. Rev. B **13**, 5188 (1976).

[137] E. Geiss, R. Sandstrom, W. Gallagher, A. Gupta, S. Shinde, R. Cook, E. Cooper, E. O'Sullivan, J. Roldan, A. Segmuller, and J. Angiello, IBM J. Res. Dev. **34**, 916 (1990).

[138] K.M. Shen, F. Ronning, D.E. Lu, W.S. Lee, N.J.C. Ingle, W. Meevasana, F. Baumberger, A. Damascelli, N.P. Armitage, L.L. Miller, Y. Kohsaka, M. Azuma, M. Takano, H. Takagi, and Z.X. Shen, Phys. Rev. Lett. **93**, 1 (2004).

[139] K. Szot, W. Speier, U. Breuer, R. Meyer, J. Szade, and R. Waser, Surf. Sci. **460**, 112 (2000).

[140] D. Kobayashi, H. Kumigashira, M. Oshima, T. Ohnishi, M. Lippmaa, K. Ono, M. Kawasaki, and H. Koinuma, J. Appl. Phys. **96**, 7183 (2004).

[141] Y. Aiura, H. Bando, Y. Nishihara, Y. Haruyama, T. Komeda, S. Kodaira, Y. Sakisaka, T. Maruyama, and H. Kato, *Advances in Superconductivity VI* (Springer, Tokyo, 1994).

[142] Y. Aiura, Y. Nishihara, Y. Haruyama, T. Komeda, S. Kodaira, Y. Sakisaka, T. Maruyama, and H. Kato, Phys. B **194**, 1215 (1994).

[143] D. Ricci, G. Bano, G. Pacchioni, and F. Illas, Phys. Rev. B **68**, 1 (2003).

[144] J.P. Buban, H. Iddir, and S. Öğüt, Phys. Rev. B **69**, 3 (2004).

[145] W. Luo, W. Duan, S.G. Louie, and M.L. Cohen, Phys. Rev. B **70**, 1 (2004).

[146] C. Lin, C. Mitra, and A.A. Demkov, Phys. Rev. B **86**, 4 (2012).

[147] C. Mitra, C. Lin, J. Robertson, and A. Demkov, Phys. Rev. B **86**, 1 (2012).

[148] V.E. Alexandrov, E.A. Kotomin, J. Maier, and R.A. Evarestov, Eur. Phys. J. B **72**, 53 (2009).

[149] D.D. Cuong, B. Lee, K.M. Choi, H.S. Ahn, S. Han, and J. Lee, Phys. Rev. Lett. **98**, 1 (2007).

[150] M. Choi, F. Oba, and I. Tanaka, Appl. Phys. Lett. **98**, 172901 (2011).

[151] Y. Tokura, Y. Taguchi, Y. Okada, Y. Fujishima, T. Arima, K. Kumagai, and Y. Iye, Phys. Rev. Lett. **70**, 2126 (1993).

[152] D.D. Sarma, S.R. Barman, H. Kajueter, and G. Kotliar, Europhys. Lett. **36**, 307 (1996).

[153] J. Szade, K. Szot, M. Kulpa, J. Kubacki, C. Lenser, R. Dittmann, and R. Waser, Phase Transitions **84**, 489 (2011).

[154] K. Iwaya, R. Shimizu, T. Ohsawa, T. Hashizume, and T. Hitosugi, Phys. Rev. B **83**, 125117 (2011).

[155] A. Bussmann-Holder, A.R. Bishop, and A. Simon, Ferroelectrics **400**, 19 (2010).

[156] S.A. Chambers, T. Ohsawa, C.M. Wang, I. Lyubinetsky, and J.E. Jaffe, Surf. Sci. **603**, 771 (2009).

[157] M.L. Knotek, Surf. Sci. **101**, 334 (1979).

[158] N. Erdman, K.R. Poeppelmeier, M. Asta, O. Warschkow, D.E. Ellis, and L.D. Marks, Nature **419**, 55 (2002).

[159] M. Castell, Surf. Sci. **505**, 1 (2002).

[160] T. Kubo and H. Nozoye, Surf. Sci. **542**, 177 (2003).

[161] O. Warschkow, M. Asta, N. Erdman, K.R. Poeppelmeier, D.E. Ellis, and L.D. Marks, Surf. Sci. **573**, 446 (2004).

[162] K. Johnston, M. Castell, A. Paxton, and M. Finnis, Phys. Rev. B **70**, 085415 (2004).

[163] R. Herger, P. Willmott, O. Bunk, C. Schlepütz, B. Patterson, B. Delley, V. Shneerson, P. Lyman, and D. Saldin, Phys. Rev. B **76**, 195435 (2007).

[164] G.W. Trucks, K. Raghavachari, G.S. Higashi, and Y.J. Chabal, Phys. Rev. Lett. **65**, 504 (1990).

[165] M.C. Flowers, N.B.H. Jonathan, Y. Liu, and A. Morris, J. Chem. Phys. **102**, 1034 (1995).

[166] C. Li, D. Cui, Y. Zhou, H. Lu, and Z. Chen, Appl. Surf. Sci. **136**, 173 (1998).

[167] S. Tinte, M. Stachiotti, M. Sepliarsky, R. Migoni, and C. Rodriguez, J. Phys. Condens. Matter **11**, 9679 (1999).

[168] S. Piskunov, E.A. Kotomin, E. Heifets, J. Maier, R.I. Eglitis, and G. Borstel, Surf. Sci. **575**, 75 (2005).

[169] C. Wang, G. Zhou, J. Li, B. Yan, and W. Duan, Phys. Rev. B **77**, 245303 (2008).

[170] F. Löffler, Surf. Coatings Technol. **132**, 222 (2000).

[171] C.T. Campbell, Surf. Sci. Rep. **27**, 1 (1997).

[172] C. Henry, Surf. Sci. Rep. **31**, 231 (1998).

[173] M. Finnis, J. Phys. Condens. Matter **8**, 5811 (1996).

[174] H. Brune, Surf. Sci. Rep. **31**, 125 (1998).

[175] F. Niu and B.W. Wessels, J. Vac. Sci. Technol. B **25**, 1053 (2007).

[176] V. Vaithyanathan, J. Lettieri, W. Tian, A. Sharan, A. Vasudevarao, Y.L. Li, A. Kochhar, H. Ma, J. Levy, P. Zschack, J.C. Woicik, L.Q. Chen, V. Gopalan, and D.G. Schlom, J. Appl. Phys. **100**, 024108 (2006).

[177] R.A. McKee, F.J. Walker, and M.F. Chisholm, Science **293**, 468 (2001).

[178] M. Dawber, K. Rabe, and J. Scott, Rev. Mod. Phys. **77**, 1083 (2005).

[179] J.F. Scott, Ferroelectrics **183**, 51 (1996).

[180] V.K. Wadhawan, *Introduction to Ferroic Materials* (CRC Press, 2000).

[181] L. Vitos, A. Ruban, H. Skriver, and J. Kollar, Surf. Sci. **411**, 186 (1998).

[182] W. Tyson and W. Miller, Surf. Sci. **62**, 267 (1977).

[183] F.R. de Boer, R. Boom, W.C.M. Mattens, A.R. Miedema, and A.K. Niessen, *Cohesion in Metals* (North-Holland, Amsterdam, 1988).

[184] J. Padilla and D. Vanderbilt, Phys. Rev. B **56**, 1625 (1997).

[185] W. Lawless, Phys. Rev. **175**, 619 (1968).

[186] W. Shih, W. Shih, and I. Aksay, Phys. Rev. B **50**, 575 (1994).

[187] J. Padilla, W. Zhong, and D. Vanderbilt, Phys. Rev. B **53**, 5969 (1996).

[188] P. Marton, I. Rychetsky, and J. Hlinka, Phys. Rev. B **81**, 144125 (2010).

[189] H. Seo and A.A. Demkov, Phys. Rev. B **84**, 045440 (2011).

[190] Y. Wei, X. Hu, Y. Liang, D.C. Jordan, B. Craigo, R. Droopad, Z. Yu, A. Demkov, J.L. Edwards, and W.J. Ooms, J. Vac. Sci. Technol. B **20**, 1402 (2002).

[191] A.A. Demkov and X. Zhang, J. Appl. Phys. **103**, 103710 (2008).

[192] H. Li, X. Hu, Y. Wei, Z. Yu, X. Zhang, R. Droopad, A.A. Demkov, J. Edwards, K. Moore, W. Ooms, J. Kulik, and P. Fejes, J. Appl. Phys. **93**, 4521 (2003).

[193] J.C. Woicik, H. Li, P. Zschack, E. Karapetrova, P. Ryan, C.R. Ashman, and C.S. Hellberg, Phys. Rev. B **73**, 1 (2006).

[194] M. Choi, A. Posadas, R. Dargis, C.-K. Shih, A.A. Demkov, D.H. Triyoso, N. David Theodore, C. Dubourdieu, J. Bruley, and J. Jordan-Sweet, J. Appl. Phys. **111**, 064112 (2012).

[195] S.H. Baek and C.B. Eom, Acta Mater. **61**, 2734 (2013).

[196] J.W. Reiner, A. Posadas, M. Wang, M. Sidorov, Z. Krivokapic, F.J. Walker, T.P. Ma, and C.H. Ahn, J. Appl. Phys. **105**, 1 (2009).

[197] J. Wang, H. Zheng, Z. Ma, S. Prasertchoung, M. Wuttig, R. Droopad, J. Yu, K. Eisenbeiser, and R. Ramesh, Appl. Phys. Lett. **85**, 2574 (2004).

[198] C. Dubourdieu, I. Gelard, O. Salicio, G. Saint-Girons, B. Vilquin, and G. Hollinger, Int. J. Nanotechnol. **7**, 320 (2010).

[199] D.M. Kim, C.B. Eom, V. Nagarajan, J. Ouyang, R. Ramesh, V. Vaithyanathan, and D.G. Schlom, Appl. Phys. Lett. **88**, 142904 (2006).

[200] M.D. McDaniel, T.Q. Ngo, A. Posadas, C. Hu, S. Lu, D.J. Smith, E.T. Yu, A.A. Demkov, and J.G. Ekerdt, Adv. Mater. Interfaces **1**, n/a (2014).

[201] J. Robertson, Reports Prog. Phys. **69**, 327 (2006).

[202] R. Droopad, Z. Yu, J. Ramdani, L. Hilt, J. Curless, C. Overgaard, J.L. Edwards, J. Finder, K. Eisenbeiser, and W. Ooms, Mater. Sci. Eng. B **87**, 292 (2001).

[203] T.P. Ma and J.P. Han, IEEE Electron Device Lett. **23**, 386 (2002).

[204] S.-Y. Wu, IEEE Trans. Electron Devices **21**, (1974).

[205] S. Salahuddin and S. Datta, Nano Lett. **8**, 405 (2008).

[206] J. Hoffman, X. Pan, J.W. Reiner, F.J. Walker, J.P. Han, C.H. Ahn, and T.P. Ma, Adv. Mater. **22**, 2957 (2010).

[207] R. McKee, F. Walker, and M. Chisholm, Phys. Rev. Lett. **81**, 3014 (1998).

[208] A. Lin, X. Hong, V. Wood, A.A. Verevkin, C.H. Ahn, R.A. McKee, F.J. Walker, and E.D. Specht, Appl. Phys. Lett. **78**, 2034 (2001).

[209] G. Niu, S. Yin, G. Saint-Girons, B. Gautier, P. Lecoeur, V. Pillard, G. Hollinger, and B. Vilquin, Microelectron. Eng. **88**, 1232 (2011).

[210] I.P. Batra, P. Wurfel, and B.D. Silverman, Phys. Rev. B **8**, 3257 (1973).

[211] D. Ito, N. Fujimura, T. Yoshimura, and T. Ito, J. Appl. Phys. **93**, 5563 (2003).

[212] Z. Yu, J. Ramdani, J.A. Curless, C.D. Overgaard, J.M. Finder, R. Droopad, K.W. Eisenbeiser, J.A. Hallmark, W.J. Ooms, and V.S. Kaushik, J. Vac. Sci. Technol. B **18**, 2139 (2000).

[213] R.A. McKee, F.J. Walker, J.R. Conner, E.D. Specht, and D.E. Zelmon, Appl. Phys. Lett. **59**, 782 (1991).

[214] M.-B. Lee, M. Kawasaki, M. Yoshimoto, and H. Koinuma, Appl. Phys. Lett. **66**, 1331 (1995).

[215] M. Warusawithana, C. Cen, C. Sleasman, J. Woicik, Y. Li, L.F. Kourkoutis, J. Klug, H. Li, P. Ryan, L.-P. Wang, M. Bedzyk, D. Muller, L. Chen, J. Levy, and D.G. Schlom, Science **324**, 367 (2009).

[216] R. Pillarisetty, Nature **479**, 324 (2011).

[217] G. Scappucci, O. Warschkow, G. Capellini, W.M. Klesse, D.R. McKenzie, and M.Y. Simmons, Phys. Rev. Lett. **109**, 1 (2012).

[218] S. Paleari, S. Baldovino, A. Molle, and M. Fanciulli, Phys. Rev. Lett. **110**, 1 (2013).

[219] K.C. Saraswat, C.O. Chui, T. Krishnamohan, A. Nayfeh, and P. McIntyre, Microelectron. Eng. **80**, 15 (2005).

[220] R. Zhang, T. Iwasaki, N. Taoka, M. Takenaka, and S. Takagi, IEEE Trans. Electron Devices **59**, 335 (2012).

[221] L. Zhang, M. Gunji, S. Thombare, and P.C. McIntyre, IEEE Electron Device Lett. **34**, 732 (2013).

[222] R. Zhang, P.C. Huang, N. Taoka, M. Takenaka, and S. Takagi, Dig. Tech. Pap. - Symp. VLSI Technol. 161 (2012).

[223] C. Merckling, G. Saint-Girons, C. Botella, G. Hollinger, M. Heyns, J. Dekoster, and M. Caymax, Appl. Phys. Lett. **98**, 092901 (2011).

[224] J.H. Ngai, D.P. Kumah, C.H. Ahn, and F.J. Walker, Appl. Phys. Lett. **104**, 062905 (2014).

[225] W. Huang, Z.P. Wu, and J.H. Hao, Appl. Phys. Lett. **94**, 92 (2009).

[226] R. Contreras-Guerrero, J.P. Veazey, J. Levy, and R. Droopad, Appl. Phys. Lett. **102**, 1 (2013).

[227] L. Kleinman, Phys. Rev. B **24**, 7412 (1981).

[228] S.L. Dudarev, G.A. Button, S.Y. Savrasov, C.J. Humphreys, and A.P. Sutton, Phys. Rev. B **57**, 1505 (1998).

[229] G.H. Kwei, A.C. Lawson, S.J.L. Billinge, and S.W. Cheong, J. Phys. Chem. **97**, 2368 (1993).

[230] B. Huang and J. Corbett, Z. Anorg. Allg. Chem. **624**, 21 (1998).

[231] P. Ponath, A.B. Posadas, R.C. Hatch, and A.A. Demkov, J. Vac. Sci. Technol. B **31**, 031201 (2013).

[232] A.A. Demkov, H. Seo, X. Zhang, and J. Ramdani, Appl. Phys. Lett. **100**, 071602 (2012).

[233] Y.L. Li, S.Y. Hu, Z.K. Liu, and L.Q. Chen, Appl. Phys. Lett. **78**, 3878 (2001).

[234] S.A. Chambers, T. Droubay, T.C. Kaspar, and M. Gutowski, J. Vac. Sci. Technol. B **22**, 2205 (2004).

[235] H.J.W. Zandvliet, Phys. Rep. **388**, 1 (2003).

[236] G. Mavrou, P. Tsipas, A. Sotiropoulos, S. Galata, Y. Panayiotatos, A. Dimoulas, C. Marchiori, and J. Fompeyrine, Appl. Phys. Lett. **93**, 212904 (2008).

[237] D. Tsoutsou, Y. Panayiotatos, A. Sotiropoulos, G. Mavrou, E. Golias, S.F. Galata, and A. Dimoulas, J. Appl. Phys. **108**, (2010).

[238] O. Sharia, A. Demkov, G. Bersuker, and B. Lee, Phys. Rev. B **75**, 1 (2007).

[239] G. V. Gibbs, M.B. Boisen, F.C. Hill, O. Tamada, and R.T. Downs, Phys. Chem. Miner. **25**, 574 (1998).

[240] A.F. Wells, *Structural Inorganic Chemistry* (Oxford University Press, New York, 1984).

[241] U. Diebold, Surf. Sci. Rep. **48**, 53 (2003).

[242] K.D. Fredrickson, A.B. Posadas, A.A. Demkov, C. Dubourdieu, and J. Bruley, J. Appl. Phys. **113**, 184102 (2013).

[243] S. Jesse, S.V. Kalinin, R. Proksch, A.P. Baddorf, and B.J. Rodriguez, Nanotechnology **18**, 435503 (2007).

[244] S. Jesse, A.P. Baddorf, and S.V. Kalinin, Appl. Phys. Lett. **88**, 9 (2006).

[245] A. Tselev, N. V. Lavrik, A. Kolmakov, and S. V. Kalinin, Adv. Funct. Mater. **23**, 2635 (2013).

[246] S.M. Anlage, V.V. Talanov, and A.R. Schwartz, *Scanning Probe Microscopy* (Springer, New York, 2006).

[247] S.M. Anlage, D.E. Steinhauer, B.J. Feenstra, C.P. Vlahcos, and F.C. Wellstood, *Microwave Superconductivity* (Kluwer Academic Publishers, Amsterdam, 2001).

[248] X.D. Xiang and C. Gao, Mater. Charact. **48**, 117 (2002).

[249] B.T. Rosner and D.W. Van Der Weide, Rev. Sci. Instrum. **73**, 2505 (2002).

[250] K. Lai, W. Kundhikanjana, M. Kelly, and Z.X. Shen, Rev. Sci. Instrum. **79**, (2008).

[251] K. Lai, W. Kundhikanjana, M.A. Kelly, and Z.-X. Shen, Appl. Nanosci. **1**, 13 (2011).

[252] Y. Yang, K. Lai, Q. Tang, W. Kundhikanjana, M.A. Kelly, K. Zhang, Z. Shen, and X. Li, J. Micromechanics Microengineering **22**, 115040 (2012).

[253] J. Goniakowski, F. Finocchi, and C. Noguera, Reports Prog. Phys. **71**, 016501 (2008).

[254] H.Y. Hwang, Science **313**, 1895 (2006).

[255] W. Harrison, E. Kraut, J. Waldrop, and R. Grant, Phys. Rev. B **18**, 4402 (1978).

[256] S. Thiel, G. Hammerl, A. Schmehl, C.W. Schneider, and J. Mannhart, Science **313**, 1942 (2006).

[257] M. Huijben, G. Rijnders, D.H.A. Blank, S. Bals, S. Van Aert, J. Verbeeck, G. Van Tendeloo, A. Brinkman, and H. Hilgenkamp, Nat. Mater. **5**, 556 (2006).

[258] Z. Popović, S. Satpathy, and R. Martin, Phys. Rev. Lett. **101**, 256801 (2008).

[259] C.W. Bark, D.A. Felker, Y. Wang, Y. Zhang, H.W. Jang, C.M. Folkman, J.W. Park, S.H. Baek, H. Zhou, D.D. Fong, X.Q. Pan, E.Y. Tsymbal, M.S. Rzchowski, and C.B. Eom, Proc. Natl. Acad. Sci. **108**, 4720 (2011).

[260] A.D. Caviglia, S. Gariglio, N. Reyren, D. Jaccard, T. Schneider, M. Gabay, S. Thiel, G. Hammerl, J. Mannhart, and J.-M. Triscone, Nature **456**, 624 (2008).

[261] A. Manchon and S. Zhang, Phys. Rev. B **78**, 212405 (2008).

[262] G. Khalsa, B. Lee, and A.H. MacDonald, Phys. Rev. B **88**, 041302 (2013).

[263] A.D. Caviglia, M. Gabay, S. Gariglio, N. Reyren, C. Cancellieri, and J.-M. Triscone, Phys. Rev. Lett. **104**, 126803 (2010).

[264] M. Basletic, J.-L. Maurice, C. Carrétéro, G. Herranz, O. Copie, M. Bibes, E. Jacquet, K. Bouzehouane, S. Fusil, and A. Barthélémy, Nat. Mater. **7**, 621 (2008).

[265] G. Khalsa and A.H. MacDonald, Phys. Rev. B **86**, 125121 (2012).

[266] M. Takizawa, H. Wadati, K. Tanaka, M. Hashimoto, T. Yoshida, A. Fujimori, A. Chikamatsu, H. Kumigashira, M. Oshima, K. Shibuya, T. Mihara, T. Ohnishi, M. Lippmaa, M. Kawasaki, H. Koinuma, S. Okamoto, and A. Millis, Phys. Rev. Lett. **97**, 057601 (2006).

[267] S. Okamoto, A. Millis, and N. Spaldin, Phys. Rev. Lett. **97**, 056802 (2006).

[268] R. Pentcheva and W. Pickett, Phys. Rev. Lett. **102**, 107602 (2009).

[269] R. Arras, V.G. Ruiz, W.E. Pickett, and R. Pentcheva, Phys. Rev. B **85**, 125404 (2012).

[270] J.W. Park, D.F. Bogorin, C. Cen, D.A. Felker, Y. Zhang, C.T. Nelson, C.W. Bark, C.M. Folkman, X.Q. Pan, M.S. Rzchowski, J. Levy, and C.B. Eom, Nat. Commun. **1**, 94 (2010).

[271] C. Cen, S. Thiel, J. Mannhart, and J. Levy, Science **323**, 1026 (2009).

[272] C. Cen, S. Thiel, G. Hammerl, C.W. Schneider, K.E. Andersen, C.S. Hellberg, J. Mannhart, and J. Levy, Nat. Mater. **7**, 298 (2008).

[273] H.W. Jang, D.A. Felker, C.W. Bark, Y. Wang, M.K. Niranjan, C.T. Nelson, Y. Zhang, D. Su, C.M. Folkman, S.H. Baek, S. Lee, K. Janicka, Y. Zhu, X.Q. Pan, D.D. Fong, E.Y. Tsymbal, M.S. Rzchowski, and C.B. Eom, Science **331**, 886 (2011).

[274] P. V. Ong, J. Lee, and W.E. Pickett, Phys. Rev. B **83**, 193106 (2011).

[275] N. Sai, J. Lee, C.J. Fennie, and A.A. Demkov, Appl. Phys. Lett. **91**, 202910 (2007).

[276] Y. Kozuka, A. Tsukazaki, and M. Kawasaki, Appl. Phys. Rev. **1**, 011303 (2014).

[277] P. Anderson and E. Blount, Phys. Rev. Lett. **14**, 217 (1965).

[278] T. Kolodiazhnyi, M. Tachibana, H. Kawaji, J. Hwang, and E. Takayama-Muromachi, Phys. Rev. Lett. **104**, 147602 (2010).

[279] Y. Wang, X. Liu, J.D. Burton, S.S. Jaswal, and E.Y. Tsymbal, Phys. Rev. Lett. **109**, 247601 (2012).

[280] Y. Shi, Y. Guo, X. Wang, A.J. Princep, D. Khalyavin, P. Manuel, Y. Michiue, A. Sato, K. Tsuda, S. Yu, M. Arai, Y. Shirako, M. Akaogi, N. Wang, K. Yamaura, and A.T. Boothroyd, Nat. Mater. **12**, 1024 (2013).

[281] J. He, G.B. Stephenson, and S.M. Nakhmanson, J. Appl. Phys. **112**, 054112 (2012).

[282] Y. Watanabe, M. Okano, and A. Masuda, Phys. Rev. Lett. **86**, 332 (2001).

[283] M.S.J. Marshall, A. Malashevich, A.S. Disa, M.-G. Han, H. Chen, Y. Zhu, S. Ismail-Beigi, F.J. Walker, and C.H. Ahn, Phys. Rev. Appl. **2**, 051001 (2014).

[284] M. Niranjan, Y. Wang, S. Jaswal, and E. Tsymbal, Phys. Rev. Lett. **103**, 016804 (2009).

[285] K. Shimoyama, M. Kiyohara, K. Kubo, A. Uedono, and K. Yamabe, J. Appl. Phys. **92**, 4625 (2002).

[286] A. Soukiassian, W. Tian, V. Vaithyanathan, J.H. Haeni, L.Q. Chen, X.X. Xi, D.G. Schlom, D.A. Tenne, H.P. Sun, X.Q. Pan, K.J. Choi, C.B. Eom, Y.L. Li, Q.X. Jia, C. Constantin, R.M. Feenstra, M. Bernhagen, P. Reiche, and R. Uecker, J. Mater. Res. **23**, 1417 (2011).

[287] A. Visinoiu, R. Scholz, S. Chattopadhyay, M. Alexe, and D. Hesse, Jpn. J. Appl. Phys. **41**, 6633 (2002).

[288] X. Zhang and A.A. Demkov, J. Vac. Sci. Technol. B **20**, 1664 (2002).

[289] W. Zhong, R. King-Smith, and D. Vanderbilt, Phys. Rev. Lett. **72**, 3618 (1994).

[290] H. Wieder, Phys. Rev. **99**, 1161 (1955).

[291] R. Eglitis and D. Vanderbilt, Phys. Rev. B **76**, 155439 (2007).

[292] J. Padilla and D. Vanderbilt, Surf. Sci. **418**, 64 (1997).

[293] R.I. Eglitis, S. Piskunov, E. Heifets, E.A. Kotomin, and G. Borstel, Ceram. Int. **30**, 1989 (2004).

[294] A. Demkov, L. Fonseca, E. Verret, J. Tomfohr, and O. Sankey, Phys. Rev. B **71**, 195306 (2005).

[295] B. Jaffe, W. Cook, and H. Jaffe, *Piezoelectric Ceramics* (Academic, New York, 1971).

[296] L. Huang, Z. Chen, J.D. Wilson, S. Banerjee, R.D. Robinson, I.P. Herman, R. Laibowitz, and S. O'Brien, J. Appl. Phys. **100**, 034316 (2006).